Parylene Technology for Neural Probes Applications

Thesis by

Changlin Pang

In Partial Fulfillment of the Requirements

for the Degree of

Doctor of Philosophy

California Institute of Technology

Pasadena, California

2008

(Defended September 17th, 2007)

To my wife

Acknowledgements

I would first and foremost like to express my gratitude to my advisor, Professor Yu-Chong Tai. Without his advice, guidance, and support, I would not have accomplished what I have achieved in my five years at Caltech. What I learnt from him is far beyond research.

My appreciation also goes to the previous group members who helped me to start my Ph.D. work, including Dr. Ellis Meng, Dr. Jun Xie, Dr. Qing He, Dr. Justin Boland, Dr. Matthieu Liger, Mr. Ted Harder, and Dr. Victor Chi-Yuan Shih. From them I received numerous kinds of help which are impossible to list here.

Thanks to all my colleagues in the group: Dr. Siyang Zheng, Dr. Scott Miserendino, Dr. Angela Tooker, Dr. Damien Rodger, Po-Jui Chen, Quoc (Brandon) Quach, Wen Li, Nick Lo, Jason Shih, Mike Liu, Luca Giacchino, Ray Huang, Jeffrey Chun-Hui Lin, Mandheerej S. Nandra, Juhwan Yoo, Justin Young-Hyun Kim, Tanya Owen, Christine Matsuki, and Trevor Roper. Your support over the years is greatly appreciated.

The interdisciplinary nature of my work has allowed me to have many great collaborators. I would like to thank Prof. Richard A. Andersen and Prof. Joel W. Burdick. They have provided much guidance and assistance for my research. The same gratitude goes to the colleagues in Prof. Anderson's lab: Dr. Sam Musallam, Dr. Daniel Rizzuto, Dr. Jeremy Emken, and Dr. Cevat Ustun; and the colleagues in Prof Burdick's lab: Dr. Jorge G.Cham, Dr. Zoran Nenadic, and Dr. Rachel Berquist for their assistance on my projects.

Thank Luca Giacchino and Ray Huang, who were working together with me on the projects and gave me very helpful proofreading of my thesis.

Abstract

Parylene Technology for Neural Probes Applications

Thesis by

Changlin Pang

Doctor of Philosophy in Electrical Engineering

California Institute of Technology

Neural probes are important tools in detecting and studying neuron activities. Although people have been working on neural probe development for a long time, the current neural probes (including metal-wire probes and silicon neural probes) are still far from being satisfactory. An ideal neural probe array should have good biocompatibility, high-density electrodes with high signal-to-noise ratio, flexible cables for interconnections, integrated electronics, and even integrated actuators to track neuron movement.

The work of this thesis focused on applying parylene technology to neural probes development to make a new generation of neural probes with better functions. With the properties of high electrical resistivity, mechanical flexibility, biocompatibility, low coefficient of friction, and an easy deposition/etching process, parylene is a good material for neural probe applications. In this thesis, we have designed, fabricated, and characterized a new parylene neural probe with a long, flexible parylene cable for a neural prosthesis system. Parylene layers are first used on the silicon probe shank with multiple electrodes as insulation and protective layers. And long parylene flexible cables are first monolithically

integrated with silicon neural probes. A 96-electrode high-density, 3-D neural probe array for chronic implantation has been demonstrated. Different types of electrolysis actuators (including a silicon diaphragm actuator and a parylene balloon actuator) have been made and tested. The research on electrolysis-based actuators shows their great potential to be used for movable neural probes.

Compared with the traditional silicon neural probes (e.g., the Michigan probes, the Utah electrode arrays), our microfabricated neural probes have much longer and stronger probe shanks (8 or 12 mm long, able to penetrate the human pia) and much longer flexible parylene cable (about 7 or 12 cm, long enough to go through a percutaneous connector and the human skull). At the same time, our new probe arrays are shown to have better biocompatibility (being totally covered with parylene material), lower stress, better penetration ability, and greater flexibility for making high-density 3-D arrays and for use in chronic neural signal recording implantation.

Table of Contents

List of Figures

LIST OF TABLES

CHAPTER 1

INTRODUCTION

1.1 History of Neural Probes

1.1.1 Functions of Neural Probes

Humanity has struggled to understand the nervous system and develop treatments for its disorders for centuries. As early as 1757, people explored the use of electrical currents as an approach to overcome paralysis [1]. From the middle of the last century, neural probes became the most important tool in enabling neural scientists to locate microelectrode sensors near to individual neurons and to sense their action potentials [2, 3]. The neural probe technologies make it possible to use extracellular recording of the electrical activity of single neuron [4-6] or groups of neurons using multiple electrodes [7-11] to help people to understand neuron activities. Acute and chronic multiple-electrode recordings have also been used in a variety of cortical and sensory areas [12-14] to study issues such as population encoding [15, 16], somatosensory organization [17-19], nervous system behavior [20, 21], and network connectivity [9]. It quickly became clear that arrays of

electrodes, and perhaps large arrays, would be needed to really understand the signal processing performed in complex neural networks. Figure 1-1(a) shows the typical neural signal (action potential) that the neural probes are used to detect from the brain. The illustration of the use of multiple electrodes for recording of extracellular neural signals is shown in Figure 1-1(b).
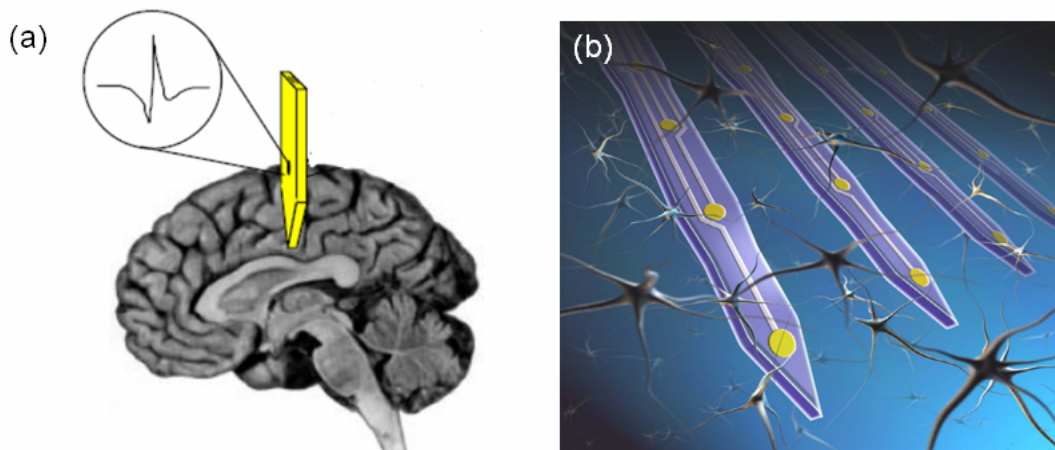
Figure 1-1　(a) Illustration of the use of neural probe to detect neural signals from the brain; (b) the use of multiple electrodes for recording extracellular neural signals

1.1.2　Traditional Neural Probes

One of the typical traditional neural probes is the metal-wire neural probe [2, 22, 23]. The metal-wire neural probes are sharpened wires, normally less than 100 μm in diameter and insulated to define an exposed recording area at the tip. Different types of metal are used, e.g., stainless steel, tungsten, iridium, platinum-iridium, elgiloy, etc. Quarzglass, Teflon (TFE), polyimide (Kapton), or parylene are normally used for the insulation of metal wire neural probes. Different methods to open the electrode tip are developed for different types of insulation and different requirements for electrode impedance control. Figure 1-2 shows the SEM picture of the tip of a commercially available

metal-wire neural probe which is coated with parylene C and opened by laser [24]. Some of the metal-wire neural probes have a very sharp tip for tissue penetration, but the problem is that the size and the position of the electrode opening is hard to control.
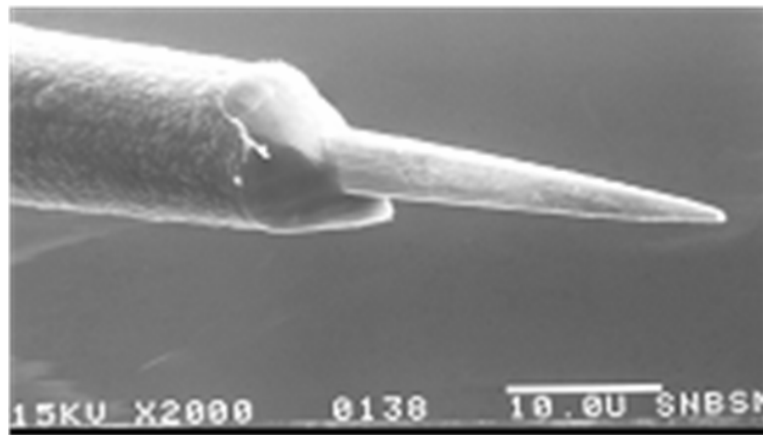
Figure 1-2   The SEM picture of a parylene coated metal wire neural probe [24]
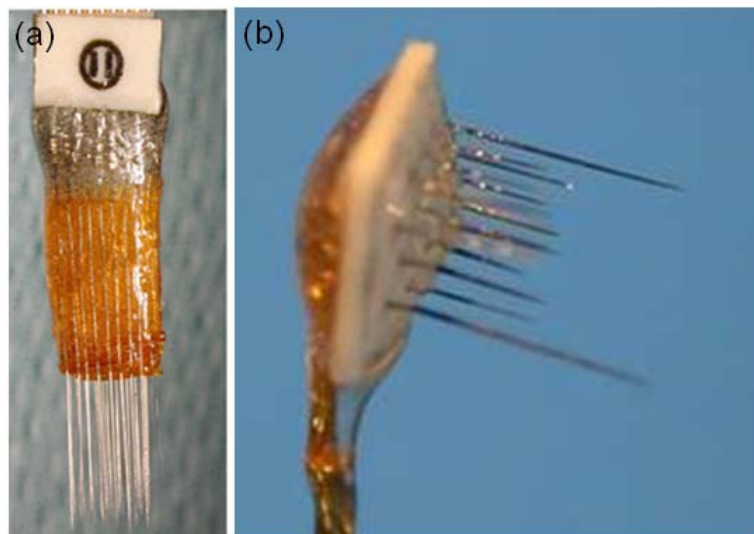
Figure 1-3   (a) An electrode array made by gluing individual metal wire electrodes [25];

(b) a microwire electrode array made by assembling metal wires on a ceramic plate

A multiple-electrode array can be made by gluing individual metal wire electrodes together (Figure 1-3(a)) [25] or by using cutoff wire bundles [26, 27]. Figure 1-3(b) shows a

microwire electrode array made by assembling metal wires on a ceramic plate [24]. Although microwire electrode arrays are still used extensively for both acute and chronic extracellular recording, one metal wire can only have one isolated sensing electrode, which limits the use of metal wire neural probes for high-density microelectrode arrays. The microwire electrode arrays are also limited in their geometries and reproducibility, causing considerable insertion damage, and tending to splay out in tissue, making exact site placements uncertain.

KCl-filled glass micropipettes [2, 28-30] are another type of traditional neural probe, which allow penetration of the cell membrane, and are generally useful for intracellular studies. The use of KCl-filled glass micropipette neural probes is limited by high impedance and the difficulties in making multiple electrodes.

1.1.3   MEMS Neural Probes

The probe substrate is arguably the most important part of the entire structure. It must be biocompatible, small enough to avoid traumatizing the tissue, and, ideally, strong enough to penetrate the pia arachnoid membrane over the brain. Silicon has well-recognized advantages in probe fabrication. It allows use of the well-established technologies and equipments developed for the semiconductor industry.

MEMS (Microelectromechanical Systems) technology has been successfully adopted for the production of silicon neural probes. A multitude of designs of silicon neural probes have been developed for in vivo and in vitro applications. Silicon photolithography process allows for unsurpassed control over electrode size, shape, texture, and spacing, allowing multiple recording sites to be placed at variable heights on a single electrode shank. Such control provides the experimenter with absolute knowledge of the recording location,

the ability to place the recording sites at different depths to suit the geometry of the neural system under study, and a larger overall number of recording sites on a smaller volume than is possible on metal wire arrays or bundles. Circuits can be integrated directly on the probes for better signal acquisition [31-40], and MEMS add additional possibilities, such as microfluidics for drug delivery [41-43]. Even integrated micro actuators driving the electrode shank in order to track the neuron movement is made possible.

1.1.3.1 The Michigan Probes

The Michigan probes were originally developed by K. D. Wise and J. B. Angell at the Stanford University (as early as 1969) [44]. The University of Michigan has produced a variety of penetrating electrodes in single-shaft, multi-shaft, and 3-D-stacked layouts (Figure 1-4(a)) [31-40, 43-55], some of which are supplied with microelectronics.
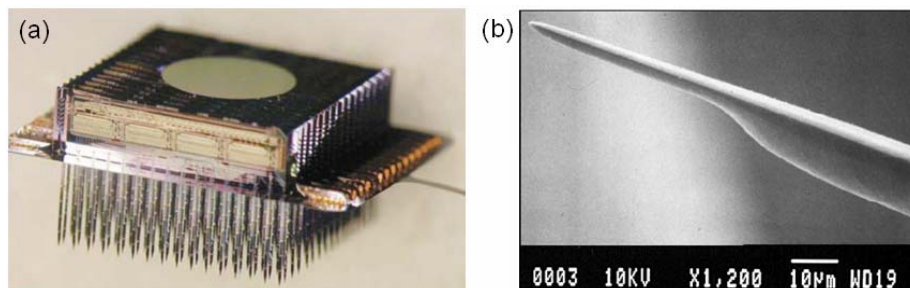
Figure 1-4　(a) The Michigan 3-D neural probe array; (b) SEM picture of the tip of the Michigan probe [45]

Figure 1-5 shows the typical process flow of the Michigan probes. Boron-etch-stop process is used for the fabrication. The theory is that EDP (ethylene diamine pyrocatechol) etching rate for p-type silicon is much slower than for pure silicon. Boron diffusion is at first performed on silicon to define the substrate shape (shape of the electrode probes), and followed by EDP wet etching to release the probes. This gives the electrodes a rounded

cross section and a rounded sharpened tip (Figure 1-4(b)). Au, Pt, or Ir is used for recording

sites.
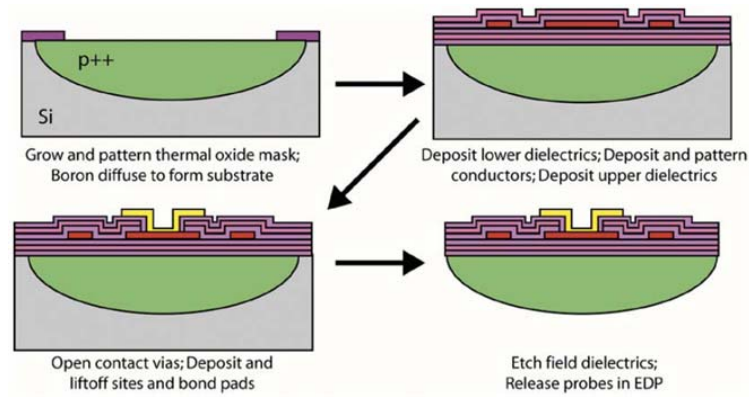
Figure 1-5　The typical process flow of the Michigan probes [45].
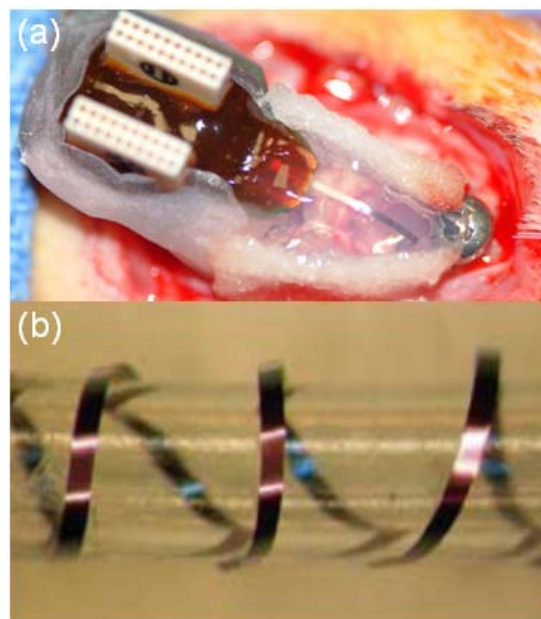
Figure 1-6　(a) The Michigan probes with silicon ribbon cable bonded with Omnetics

connectors; (b) the silicon ribbon cable for the Michigan probes [45]

Although the Michigan probes have been successfully used for a lot of applications,

the limitations of the Michigan probes are apparent.

The Michigan probes made by wet etching can only reach limited probe thickness (the typical thickness of the Michigan probes is 15 μm), and need open pia and even special guide tools for insertion because of the mechanical weakness of the probes. This may cause severe damage to the brain.

Insulation on top of silicon substrate is made with triple layer of silicon dioxide, silicon nitride, and silicon dioxide. Silicon dioxide is known to hydrate over time, though people claim stable recordings for over a year.

The interconnection is made with polysilicon which is a 4–5 μm thick silicon cable (Figure 1-6) [45, 56, 57]. Weaknesses of the thin silicon-film cable are reported: the cable is easy to break, provides low yield for longer lengths because of the high aspect ratio, and is not robust enough. Polymer cable is a good substitute.

1.1.3.2 The Utah Electrode Arrays

The University of Utah invented a new method to fabricate multiple-electrode arrays [58, 59], which have been widely used [60-64].

The Utah electrode arrays are made from conductive p-type silicon (boron doped) blocks. A diamond saw creates a grid pattern on the surface and glass is deposited on the grid to create insulation between the electrode bases. Electrode pillars are made by again sawing a grid on the other side of the silicon. Acid etching smoothes the pillars and creates the sharpened probe tips, which are coated with metal. Polyimide is used to coat the probes, with the tips exposed. Figure 1-7(a) shows the SEM pictures of the Utah array with 100 electrodes.

The Utah electrode arrays are built in the direction of the probes. Arrays are built pointing up, as opposed to all other silicon neural probes which are built lying down. As a result, the probe length of the Utah electrode arrays is limited by the silicon wafer thickness. The longest reported probe length is only 1.5 mm. Only one electrode site can be made on any one probe shank, and the fabrication process is not a batch process, therefore suffering from low production rates.

The interconnection of the Utah electrode arrays is made of a bundle of insulated 1.0 mil Au/Pd wires bonded on the back of the array (Figure 1-7(b)). The stiffness of the metal wire bundle makes these unfeasible for chronic implantation in the human brain, especially for the high-density electrode arrays.
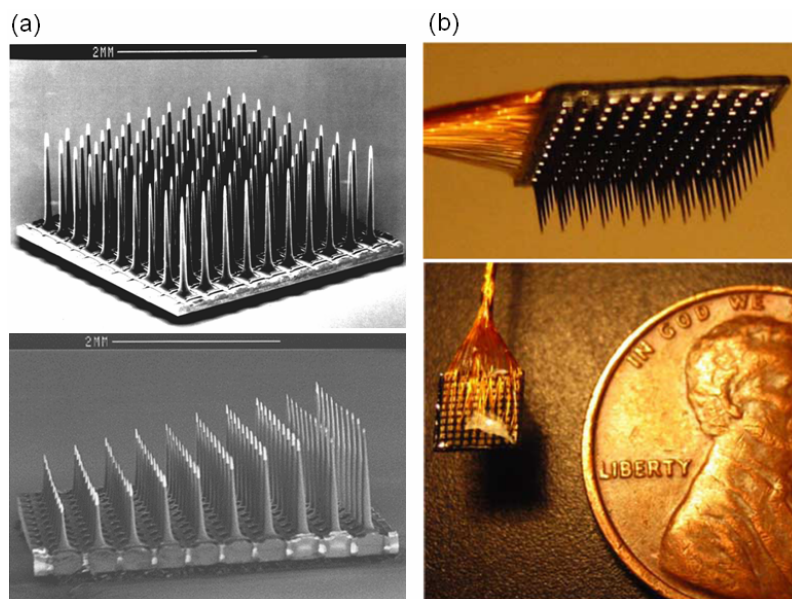
Figure 1-7   (a) SEM pictures of the Utah electrode arrays; (b) the Utah electrode arrays bonded with metal wire interconnection cable [60]

1.1.3.3　The SOI Neural Probes
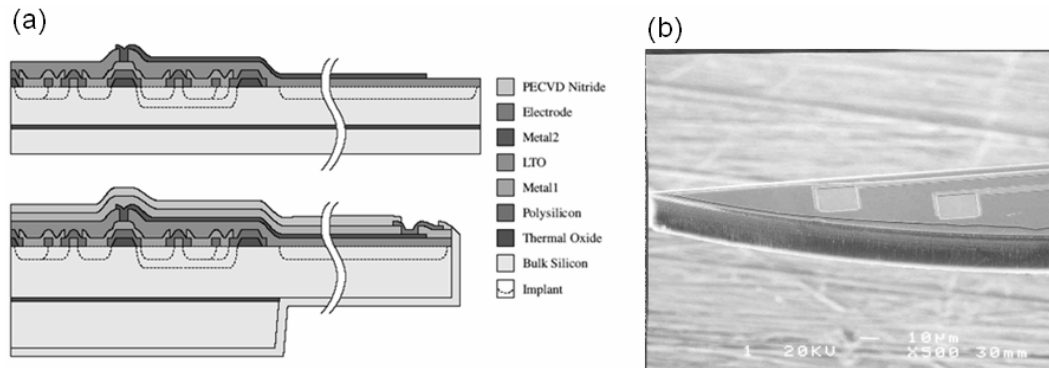
Figure 1-8　(a) The cross section of the SOI neural probes (b) SEM picture of the tip of

the SOI neural probe [41]

Figure 1-9　A SOI neural probe chip mounted on a flexible printed circuit board [65]

With the invention of silicon plasma etching technology in 1990s, new technologies were developed to fabricate neural probes by dry plasma etching, which is more reliable, and with higher fabrication yield rate than wet etching. Plasma-etched (with the combination of KOH wet etching) neural probes were developed at Caltech and Stanford in 1997 [66]. An improved technology to fabricate silicon neural probes in SOI (Silicon on Insulator) substrate by plasma etching was developed separately at UC Berkeley [41, 67],

and in Sweden [65, 68]. The cross section of the SOI neural probes and SEM picture of the tip of the SOI neural probe are shown in Figure 1-8. Plasma etching rates for SiO_2 are much slower than for silicon. SOI technology uses SiO_2 as an etch-stop layer, the probe thickness is defined by the thickness of the device layer of the SOI wafer. The SOI neural probes are made by CMOS-compatible batch process with multiple electrode sites on one probe shank. Probes with different thicknesses can be made by choosing SOI wafers with different device layer thicknesses. However, only one thickness of probe can be made from the same wafer. Moreover, the SOI wafer is expensive, increasing the fabrication cost of the probes.

One interconnection solution made by Norlin [65] for the SOI neural probes is to use a flexible printed circuit board (Figure 1-9). However, the cable can not be fabricated as small as the probe size, and a lot of wire bonding and epoxy work is needed, which is undesirable in a batch process.

1.1.3.4 The Polymer Neural Probes

In addition to the normal silicon nitride or silicon dioxide insulation deposited during the fabrication of silicon electrodes, selected biocompatible polymers (such as polyimide [69], parylene C) are used to coat silicon-based probes. As we discussed above, polyimide was used to coat the Utah electrodes arrays [58, 59]. Parylene C was used as insulating layer on silicon probes by Xu [70]. But for the current polymer coated silicon probes, each probe shank contains only a single recording site, and a special process was required to open the probe tips.

A flexible polyimide neural probe was developed in the Arizona State University [71]; similar devices were also reported by the University of Tokyo [72]. As shown in Figure 1-10, the electrode metal layer is sandwiched between two polyimide layers without

silicon structure. The 3-D probes are formed by bending the polyimide shanks out of the 2-D plane. The flexibility of polyimide may improve the mechanical impedance mismatch between a rigid electrode and soft tissue resulting in tissue damage if micromotion of the electrode occurs. A major drawback to this design was that the electrodes were not stiff enough to pierce brain tissue on their own, so implant sites had to be created with wire or a scalpel before insertion.
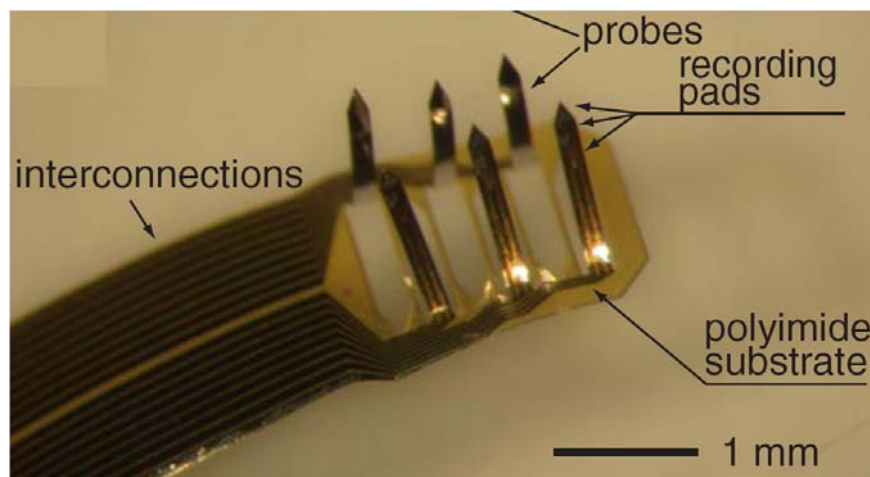
Figure 1-10   A flexible polyimide neural probe [72]

An improved polyimide probe was reported by Lee et al. [73]. The polyimide electrodes were integrated with thin silicon (5-10 μm) backbone to increase stiffness. A similar polyimide probe with molybdenum backbone (15 μm) was developed in the Johns Hopkins University [74]. Polyimide-based probes are prone to failure due to possible moisture absorption by polyimide.

Polymer materials are also used to make the interconnect cables. For example, microfabricated polyimide cables [75] and PDMS cables [76] are reported for the

interconnections of the silicon neural probes. But different bonding methods are still required to connect the polymer cables with the microfabricated silicon probes.

1.2   Applications of Neural Probes for Neural Prosthesis

A neural prosthesis is a direct brain interface that enables a primate, via the use of surgically implanted electrode arrays and associated computer algorithms, to control external electromechanical devices by pure thought alone. The first beneficiaries of such technology are likely to be patients with spinal cord damage, peripheral nerve disease, or ALS (amyotrophic lateral sclerosis, also known as Lou Gehrig's disease). In the United States alone, there are 2.28 million patients with some form of paralysis.

A primary issue in neuroprosthetic research is the choice of brain area from which prosthetic command signals are derived. Current studies around the world have focused primarily on deriving neuroprosthetic command signals from the motor cortex [77-80]. Recordings from multiple neurons are "decoded" to control the trajectories of a robotic limb or a cursor on a computer screen. In addition, progress has been made in using electroencephalogram (EEG)-based signals to derive neuroprosthetic commands.

At Caltech, however, we have pursued a novel approach, which is to use high-level cognitive signals for controlling neural prostheses (Figure 1-11) [81-84]. Read-outs are made of the goals and intentions of the subject, rather than the instructions on how to obtain those goals. Smart output devices—such as robots, computers, or vehicles—using supervisory control systems, then manage carrying out the physical tasks required to complete the intended goal. The cognitive signals that can be read-out are myriad and can include the expected value of an action and, perhaps in the future, speech, emotional state, and other higher cortical functions. An "expected value signal" is used by the brain to make

decisions and can be used by prosthetics to interpret a subject's decisions, preferences, and motivation—all of which would help a paralyzed patient communicate better with the outside world.
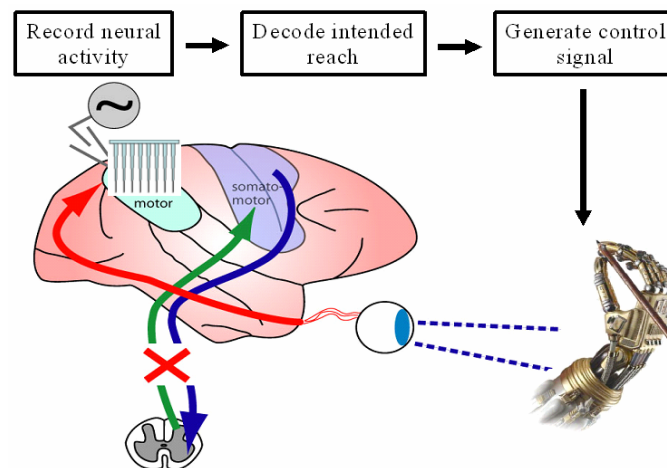
Figure 1-11   Schematic of the pathway of information flow for the cognitive-based neural prosthetic paradigm

1.3   Current Challenges of Neural Probe Fabrication

To achieve the goal of neural prosthesis, a 3-D neural probe is needed to record the cortex cognitive signals. Although people have put great effort into making neural probes in the last several decades, all of the various types of neural probes developed are still far from being satisfactory.

Although most neuroscience research continues to be conducted using the well-established microwire electrodes, the next generation of electrode arrays being developed is predominantly silicon based. Silicon micromachined electrodes allow more complex designs and thus greater flexibility in strategies designed to minimize the foreign-body response and maximize the control over electrode placement. The emergence

of silicon micromachining technology has yielded increasingly smaller and higher-electrode-count arrays capable of recording from greater volumes of neural tissue with improved spatial discrimination.

Ideally, a 3-D multielectrode neural probe array should have integrated electronics for high signal-to-noise ratio, and flexible cables for through-skull interconnection. Unfortunately, there are two major problems with the current devices. The first one is related to insulating/protecting materials. It's granted that probes have to use silicon when IC is necessary. The question is about insulating materials such as SiO_2 and Si_3N_4, which are all subject to body-fluid corrosion. Worse yet, they are brittle and have reliability issues under stress. The second problem is related to through-skull interconnection. Signals obtained by probes have to be cabled out of the skull. Even with telemetry, a cable is still needed to link the in-cortex probes to a telemetry platform that can only be safely mounted above the skull. Cables are important. As we discussed above, the existing silicon ribbon cables for the Michigan probes, metal-wire cables for the Utah electrode arrays and flexible PCB cables for the SOI probes all suffer from low reliability, high stiffness and difficulties of integration, and are therefore not feasible for high-density probe arrays. Microfabricated polymer (e.g. polyimide) cable is a good approach, but vast bonding work is still needed to connect the polymer cables with the silicon probes. An ideal case is a microfabricated polymer cable monolithically integrated with the neural probes during the probes fabrication, therefore no extra bonding work is needed to connect the cables and the probes.

Current applications of neural probes for chronic implantation in monkey or human brains require a strong mechanical property of the probes in order to penetrate the brain pia. The current silicon probes—for example, the Michigan probes made by wet etching—can

only reach limited probe thickness, and need an open pia and even special guide tools for insertion because of the mechanical weakness of the probes. This may cause greater damage to the brain.

Some other issues with the existing neural probes include: special fabrication processes leading to low yield and high cost (the Michigan probes); lack of IC integration leading to high noise (the Utah electrode arrays); short probes limited by technology (the Utah electrode arrays); low design flexibility; and low yield when working with large number of electrodes.

Another big challenge of the existing silicon neural probes is that none of them has the ability to move. The array's useful signal yield may be low if the electrodes' active recording sites lie in electrically inactive tissue, are distant from cell bodies (which generally produce the largest extracellular signals), or sample cells with non-optimal receptive fields for the task at hand. Even if the initial placement is satisfactory, fixed-geometry electrode arrays can drift in the brain matrix due to tissue movement caused by respiratory or circulatory pressure variations and mechanical shocks. This drift can lead to the separation of the electrode from the vicinity of active cells, thereby lowering signal yield. Ideally, it would be advantageous to be able to readjust the electrodes continuously after they are implanted to overcome these effects. Such continual adjustment would significantly improve the quality and yield of signals harvested by an electrode array. Electrodes that could break through scar tissue after its build up would also be useful. Manual adjustment of electrodes, which is the standard practice today, is tedious and impractical for paralyzed patients. Electrodes that could continuously and autonomously position themselves so as to optimize the neural signal would provide a great advantage.

1.4   Parylene MEMS Technology

With combination of the advantages of MEMS technology and parylene technology, parylene MEMS technology makes it possible to develop a new generation of 3-D neural probes for chronic implantation of a neural prosthesis system with better functions.

1.4.1   Introduction to MEMS Technology

Born from IC (Integrated Circuit) technology, MEMS (Microelectromechanical Systems) is growing as a revolutionary technology that enables fabrication of mechanical elements, electronics, sensors, and actuators on common substrate. The advantages of MEMS technology include: suitability for high-volume and low-cost production; reduced size, mass, and power consumption; high functionality; improved reliability; novel solutions; and new applications. Because of its root in the IC industry, many of MEMS basic processing techniques are borrowed or adapted from IC technology, such as photolithography, oxidation, diffusion, ion implantation, chemical vapor deposition (CVD), evaporation, sputtering, wet chemical etching, and dry plasma etching. There are a number of features common in MEMS fabrication processes that are not as common in IC fabrication; these are: nonplanar substrate (i.e., relatively large 3-D features); the use of thick photoresist layers (for structure purposes or for long etching time); relatively high aspect ratio structures; relatively large feature sizes; unusual processing steps; and unusual materials (particularly important in terms of adhesion).

Silicon micromachining has been a key factor for the vast progress of MEMS. Silicon micromachining comprises two technologies: bulk micromachining, in which structures are etched into silicon substrate and surface micromachining, in which the

micromechanical structures are formed from layers and films deposited on the silicon surface (Figure 1-12).
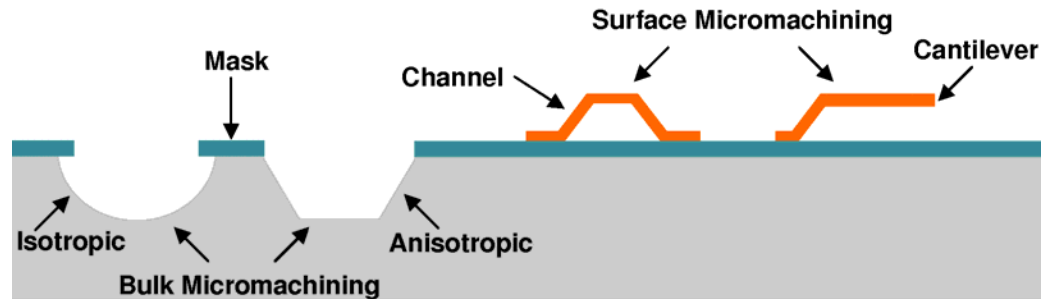
Figure 1-12   Illustration of bulk micromachining and surface micromachining [85].

1.4.1.1   Bulk Micromachining

Bulk micromachining describes the fabrication process of a device taking advantage of all three space dimensions. In most applications single crystalline silicon is used as bulk material. Bulk micromachining defines structures by selectively etching inside a substrate. Isotropic wet etchant such as HNA (hydrofluoric acid + nitric acid + acetic acid), and anisotropic wet etchant such as solutions of KOH (potassium hydroxide), EDP (ethylene diamine pyrocatechol), TMAH (tetra-methyl-ammonium-hydroxide), and hydrazine-water are used. These anisotropic wet etchants have different etch rates in different crystal orientation of the silicon [86]. By combining anisotropic etching with boron implantation (P+ etch-stop) and electro-chemical etch-stop technique, varied silicon microstructures can be bulk machined.

Dry etching occurs through chemical or physical interaction between the ions in the gas and the atoms of the substrate. The nonplasma, isotropic dry etching is possible using XeF_2 (xenon difluoride) or a mixture of interhalogen gases and provides very high selectivity for aluminum, silicon dioxide, silicon nitride, photoresist, etc. The most

common dry etching of bulk silicon is plasma etching and RIE (reactive ion etching), in which the external energy in the form of radio frequency (RF) power drives chemical reactions in low-pressure reaction chambers. A wide variety of chlorofluorocarbon gases, sulfur hexafluoride, bromine compounds and oxygen are commonly used as reactants. The anisotropic dry etching processes are widely used in MEMS because of the geometry flexibility and the less chemical contaminations as compared with wet etching. High aspect ratio microstructures can be obtained by deep reactive ion etching (DRIE) with "Bosch process", which is a room temperature process based on continuous cycling subsequent passivation and etching steps.

1.4.1.2 Surface Micromachining

Unlike bulk micromachining, where a silicon substrate (wafer) is selectively etched to produce structures, surface micromachining is based on the deposition and etching of different structural layers on top of the substrate. Surface micromachining starts with a silicon wafer or other substrate and grows layers on top. These layers are selectively etched by photolithography and either a wet etch involving an acid or a dry etch involving an ionized gas or plasma. Surface micromachining requires a compatible set of structure materials, sacrificial materials, and chemical etchants. The structure materials must posses the physical and chemical properties that are suitable for the desired application. The sacrificial layers are used to make suspended structures. The sacrificial materials must have good properties to avoid device failure during fabrication. These properties include good adhesion and low-residual stresses to eliminate device failure by delamination and/or cracking. Common sacrificial materials are photoresist, polyimide, metals, phosphosilicate glass (PSG), and polysilicon.

1.4.2 Introduction to Parylene

Parylene is the generic name for members of a unique family of thermoplastic polymers that are deposited by using the dimer of para-xylylene (di-para-xylylene, or DPXN) [87]. Discovered by Dr. Michael Mojzesz Szwarc at the University of Manchester, England, in 1947 and commercialized by Union Carbide Corporation in 1965, parylene is used in several industries because of its superior properties. The primary application is PCB (printed circuit board) coating in the electronics industry, where parylene protects the delicate electronic devices against moisture and corrosive environments. Figure 1-13 shows the chemical structures of the three most commonly used parylene types: parylene N, parylene C, and parylene D, and a new parylene variant: parylene HT. Parylene N is poly-para-xylylene, a completely linear and highly crystalline polymer. Parylene C is basically parylene N with a chlorine atom replacing one of the aromatic hydrogens. Parylene D is similar to parylene C but with two aromatic hydrogens being replaced with chlorine atoms. The benzene backbone of the parylenes makes them very chemically inert, while the polyethylene-like interconnect makes them flexible.
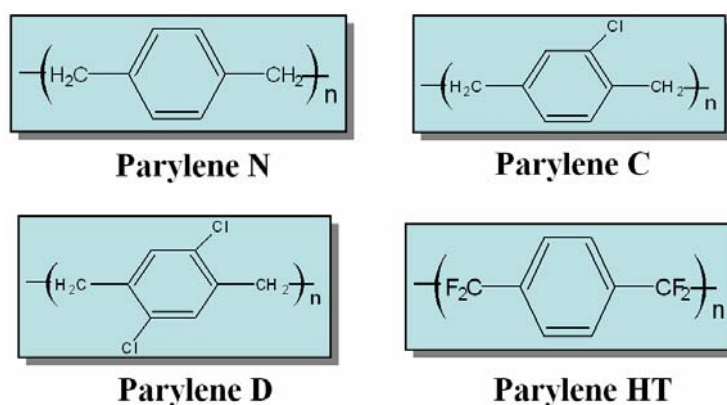
Figure 1-13   Chemical structures of parylene N, C, D, and HT

Detailed electrical, mechanical, thermal, barrier, optical, and other properties of parylene can be found on a parylene vendor's website [88]. A list of selected properties of parylene N, C, and D and HT are shown in Table 1-1.

Table 1-1   A list of selected properties of parylene N, C, D, and HT

Typical Properties of Parylene	Parylene N	Parylene C	Parylene D	Parylene HT
Typical Physical & Mechanical Properties				
Young's modulus, GPa	2.42	2.76	2.62	NA
Tensile strength, MPa	41–76	69	76	NA
Yield strength, MPa	43	55	62	NA
Elongation at break, %	20–250	200	10	NA
Density, g/cm^3	1.10–1.12	1.289	1.418	NA
Coefficient of friction: static	0.25	0.29	0.33	0.145
dynamic	0.25	0.29	0.31	0.130
Water absorption, % (24 hr)	<0.1	<0.1	<0.1	<0.01
Index of refraction, n_D^{23}	1.661	1.639	1.669	NA
Strong UV absorption, nm	<280	<280	NA	NA
Typical Electrical Properties				
Dielectric strength, Volts/mil, (short time at 1 mil)	7,000	5,600	5,500	5,400
Volume resistivity, Ω·cm, (23 °C, 50% RH)	1.4×10^{17}	8.8×10^{16}	1.2×10^{17}	NA
Surface resistivity, Ω·cm, (23 °C, 50% RH)	10^{13}	10^{14}	10^{16}	NA
Dielectric constant: 60 Hz	2.65	3.15	2.84	2.21
1 KHz	2.65	3.10	2.82	2.20
1 MHz	2.65	2.95	2.80	2.17
Dissipation factor: 60 Hz	0.0002	0.020	0.004	0.0002
1 KHz	0.0002	0.019	0.003	0.0020
1 MHz	0.0006	0.013	0.002	0.0010
Typical Barrier Properties				
Gas permeability, cm^3(STP)·mil/100in^2·24hr·atm, (25 °C)				
N_2	7.7	1.0	4.5	4.8
O_2	39	7.2	32	23.5
CO_2	214	7.7	13	95.4
H_2	540	110	240	NA
Moisture vapor transmission, g·mil/100in2·24hr, (37 °C, 90% RH)	1.50	0.21	0.25	NA

Typical Thermal Properties				
Melting temperature, ºC	420	290	380	>450
Glass transition temperature, ºC	NA	80-100	NA	NA
Continuous service temperature, ºC	60	80	100	350
Linear coefficient of expansion, ppm/ ºC	69	35	30–80	NA
Thermal conductivity, 10^{-4}cal/(cm·s·ºC)	3.0	2.0	NA	NA
Other Properties				
Best crevice penetration, times of the opening i.d.	40	8	NA	50
Certified biocompatibility	USP Class VI ISO-10993	USP Class VI ISO-10993	NA	USP Class VI ISO-10993

Parylene exhibits impressive mechanical strength and flexibility in a thin film coating. With Young's modulus of 2–3 GPa and an elongation-to-break percentage of more than 200%, parylene C is a perfect membrane material for large deflection applications.

Parylene is an excellent electrical insulator with high electrical resistivity. For example, the breakdown voltage for 1 μm thick parylene is over 200 volts. The parylene film is highly conformal and pinhole free. It is also an excellent barrier to gas and moisture. Parylene is extremely inert to most chemicals and solvents. Based on the manufacturer's study [89], solvents have minor swelling effect on parylene N, C, and D, with a 3% maximum increase in film thickness. The swelling is found to be completely reversible after the solvents are removed by vacuum drying. Inorganic reagents, except for oxidizing agents at elevated temperatures, have little effect on parylene.

Optically, parylene is transparent in the visible light range. It only absorbs light under 280 nm in wavelength, which unfortunately limits its UV applications.

Due to their slightly different chemical structures, the four types of parylene also differ in properties. Parylene N has good crevice penetration characteristics. However, parylene N also has the slowest deposition rate. Parylene D can withstand higher temperature

than parylene C. Parylene C has a useful combination of electrical and physical properties plus a very low permeability to moisture and other corrosive gases. Moreover, deposition of parylene C is faster than with the other two. Parylene C is the parylene of choice for most conventional and biomedical applications. Parylene HT is new variant which is expected to be good prospect with its better thermal stability, improved electrical properties, increased UV stability, better crevice penetration, lower coefficient of friction, and better barrier properties.

The parylene deposition process and the involved chemical processes are illustrated in Figure 1-14. The process starts with placing parylene dimer (di-para-xylylene), a stable compound in granular form, into the vaporizer, and the substrate to be coated into the deposition chamber. The whole system is pumped down to medium vacuum. The dimer is heated in the vaporizer and sublimes into vapor at around 150 °C. The dimer vapor enters the pyrolysis furnace that is maintained at 690 °C, where the dimers are cleaved into identical monomers (para-xylylene). In the room-temperature deposition chamber, the monomers reunite on all exposed surfaces in the form of polymers (poly-(para-xylylene)). The deposition takes place at the molecular level. The monomers are extremely active molecules having a mean free path on the order of 1 mm (under deposition pressure of around 100 mTorr), which results in superior penetration power and a high degree of conformability to the surfaces being coated. The coated substrate temperature never rises more than a few degrees above ambient. Additional components of the system include a mechanical vacuum pump and associated cold trap. Although parylene C structure is used in Figure 1-14, the process is almost identical for all four types of parylene, except for some slight differences in pyrolysis temperature and deposition pressure.
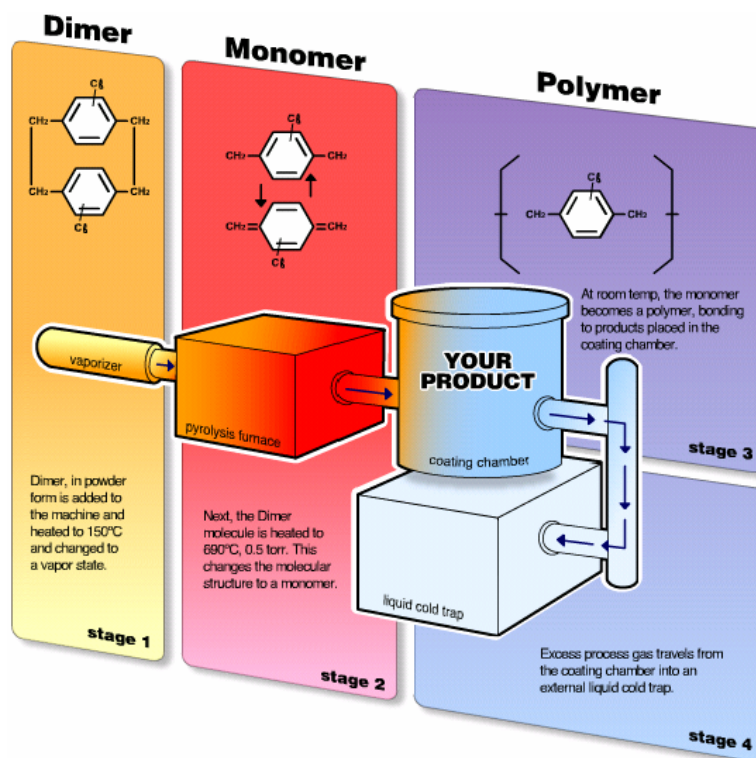
Figure 1-14   Parylene deposition system and the involved chemical processes

Typical coating thickness ranges from one to tens of microns. It can also be made as thin as hundreds of angstroms. The coating thickness can be controlled by the amount of dimer used. The normal deposition rate of parylene C is about 5 μm per hour. The deposition rate is directly proportional to the square of the monomer concentration and inversely proportional to the absolute temperature [88]. Higher deposition rates, however, can result in poor film quality, which often appears as a milky (cloudy) film, in contrast to the normal clear transparent ones.

1.4.3   Parylene Technology for Bio-implantable Devices

When foreign objects and materials come into contact with human body tissue, long-term resistance of these components to corrosive body fluids, electrolytes, proteins,

enzymes, and lipids is essential. Biomedical surfaces may require a protective coating to provide physical isolation from moisture, chemicals, and other substances. They may also need passivation, electrical insulation, and coating to reduce friction.

Most solvent-based liquid coatings such as silicones, acrylics, epoxides, polyesters, and urethanes may not meet toxicity and/or biocompatibility requirements and cannot be applied with precise control. Parylene films are formed from a pure molecular precursor (a monomer vapor), have no contaminating inclusions, do not "outgas," and form effective barriers against the passage of contaminants from substrates to both the body and the surrounding environment. Parylene is thin and pinhole-free, non-liquid (no meniscus effects), produces no cure forces (applied at room temperature), contains no additives (catalysts, plasticizers, solvents), is an excellent barrier (against moisture, fluids, and gases), inert (insoluble in most solvents), lubricious (with lubricity better than PTFE), highly dielectric, biocompatible and biostable, sterilization tolerant, and applicable to most vacuum stable materials (silicon, plastics, metals, ceramics, fabrics, paper, even granular materials).

Parylene C has been widely used for coating bio-implantable devices. An important reason is that parylene C has been proven to be a terrific biocompatible material [90, 91]. It's USP (United States Pharmacopoeia) Class VI implantable plastic material [92], and conforms to material ISO-10993 Biological Evaluations for Medical Applications. It's the choice for pacemaker wire insulation. Parylene C is also probably the longest (~ 3 years) proven protective biocompatible material [93].

1.4.4 Applications of Parylene MEMS Technology

Because of its easy coating process, controllable conformal coating thickness, and compatibility with O_2 plasma etching process, parylene technology has been easily merged

with MEMS technology. From the 1990s, parylene MEMS technology has grown very fast for applications in many areas, e.g., biology, microfludics, chemistry, etc.

Figure 1-15 shows many important microfluidic devices fabricated by parylene MEMS technology [94-100]. These microfluidic devices all have compatible fabrication processes, which potentially can all be integrated with a single batch fabrication to make a true micro total analysis system.
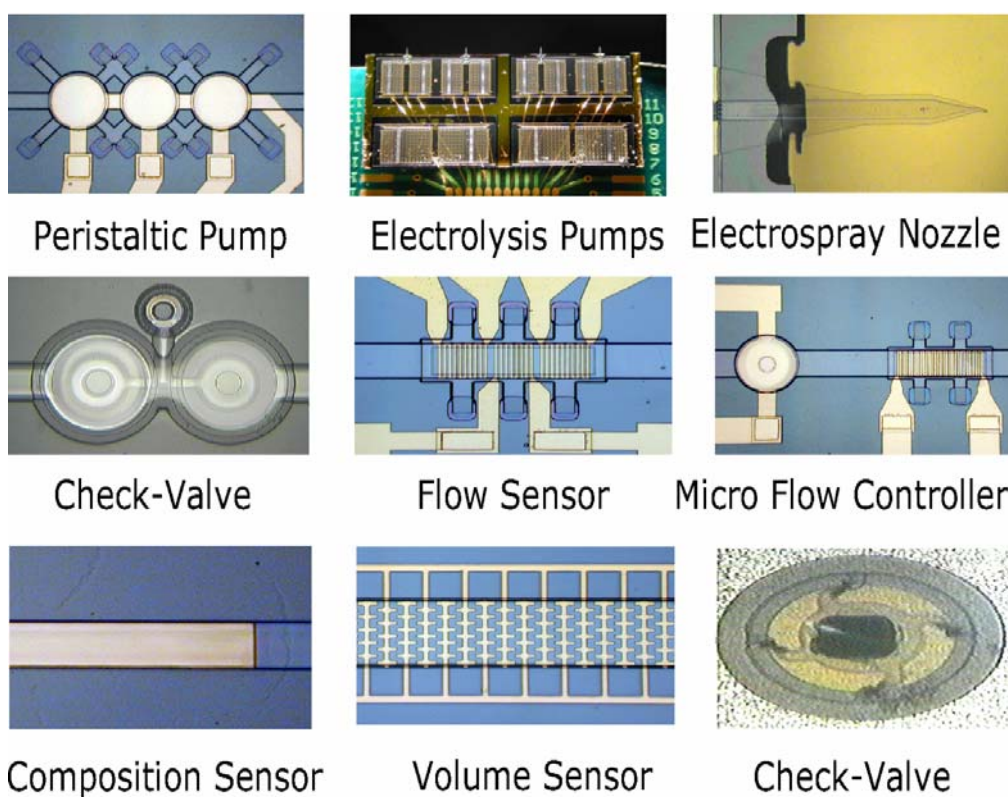
Figure 1-15　Parylene microfluidic devices

Figure 1-16 shows an integrated ion chromatography chip [101]. A parylene channel is fabricated on a silicon substrate for on-chip liquid chromatography. XeF_2 roughening and DRIE anchor technology were developed to enhance the adhesion between parylene and silicon substrate. The channel can survive inside pressures as high as 800 psi.
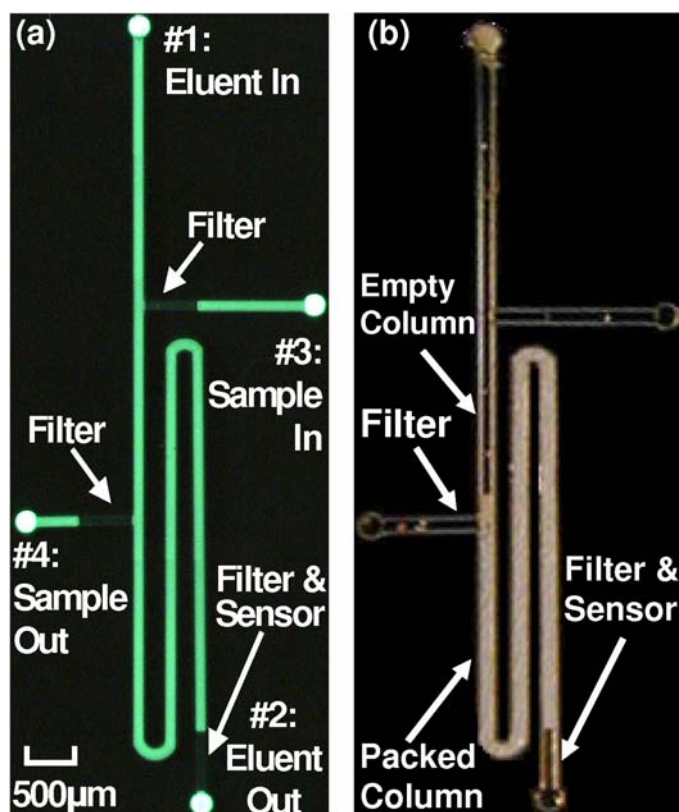
Figure 1-16   (a) Fluorescent overview picture of the integrated ion chromatography chip before column packing. (b) optical picture of the device after bead packing [101]

A parylene neuron cage (Figure 1-17) [102-104] is fabricated by a multiple-parylene-layer etching process with multiple photoresist sacrificial layers. The array of parylene neuron cages are for holding individual neurons that can extend axons and dendrites out of the tunnels to form a living network. An electrode at the bottom of each cage provides an ability to stimulate or record from each neuron, individually or simultaneously. This extracellular connection is non-destructive, providing an opportunity to study the behavior of the network over a period of weeks and to modify its connections with external stimulation.
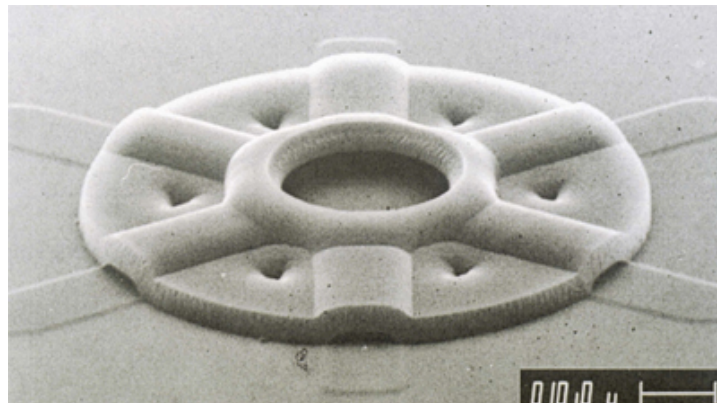
Figure 1-17　The SEM picture of the parylene neuron cage
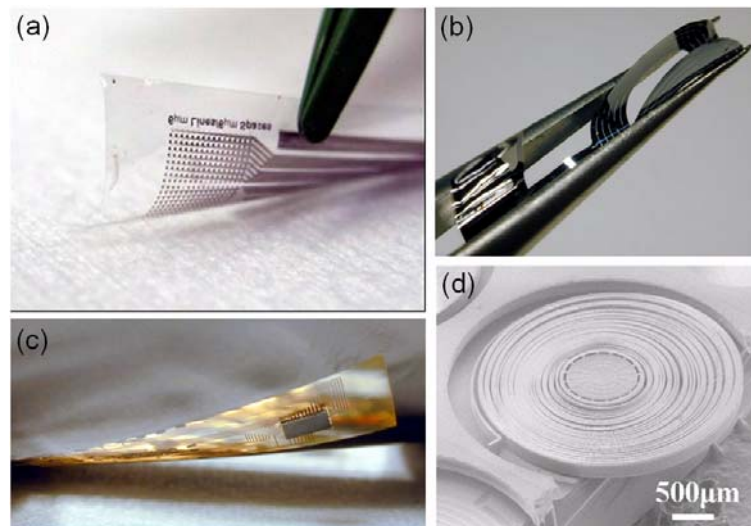
Figure 1-18　Parylene devices for a retinal prosthesis system: (a) parylene electrodes for

retinal stimulation; (b) parylene flexible coil for power and data transfer; (c) IC chip for

data processing integrated with parylene flexible cable; (d) parylene tube pressure sensor

for detecting the intraocular pressure change

　　　　Figure 1-18 shows devices developed by parylene MEMS technology for a retinal

prosthesis system. Figure 1-18(a) shows the high-density electrodes fabricated on parylene

flexible substrate for retinal stimulation [105-107]. The parylene flexible coil (Figure

1-18(b)) [108, 109] is for wireless power and data transfer. Parylene integration technology has been developed to package and connect the foundry IC with parylene flexible cable (Figure 1-18(c)) [110, 111]. Figure 1-18(d) shows the parylene tube pressure sensor for detecting the intraocular pressure change [112-117].

1.5   Summary

As we discussed above, neural probes become the most important tools to study neural activities. However, current neural probes are still far from being satisfactory because of limitations of the technologies.

The adoption of parylene MEMS technology for use in neural probe fabrication has great promise for making 3-D high-density probe arrays for chronic implantation of a neural prosthesis system with better functions. The work of this thesis presents the parylene neural probes with parylene flexible cables, and actuators for movable neural probes. We demonstrate the first applications of parylene MEMS technology on the fabrication of neural probes.

CHAPTER 2

PARYLENE NEURAL PROBES

2.1   Introduction

As we discussed in Chapter 1, silicon probes have well-recognized advantages in fabrication and application, compared with traditional metal-wire probes. Two main fabrication methods have been developed to make silicon probes. One is based on p+ etch stop and EDP wet etching technologies [45], the other depends on dry etching and silicon-on-insulator (SOI) technologies [41, 65, 67]. Each of these has its own unique set of advantages and limitations. Most of these probes use silicon dioxide or silicon nitride as insulating materials. In experimental conditions, these materials are subject to large amounts of stress, which can lead to failure. In addition, silicon dioxide is known to hydrate over time, which limits the probes' usefulness for long-term neural recording. With the properties of high electrical resistivity, mechanical flexibility, biocompatibility, and an easy deposition process, parylene is a good substitute. Parylene C was used as insulating layer on silicon neural probes by Xu [70], but each probe contained only a single recording site and a special

process was required to open the probe tips. Our work is the first to demonstrate the use of standard lithography processes to fabricate multi-site neural probes with parylene insulating/protective layers [118]. All dry etching processes have been developed to fabricate the parylene neural probes using double-side-polished (DSP) wafers.

2.2 Device Design
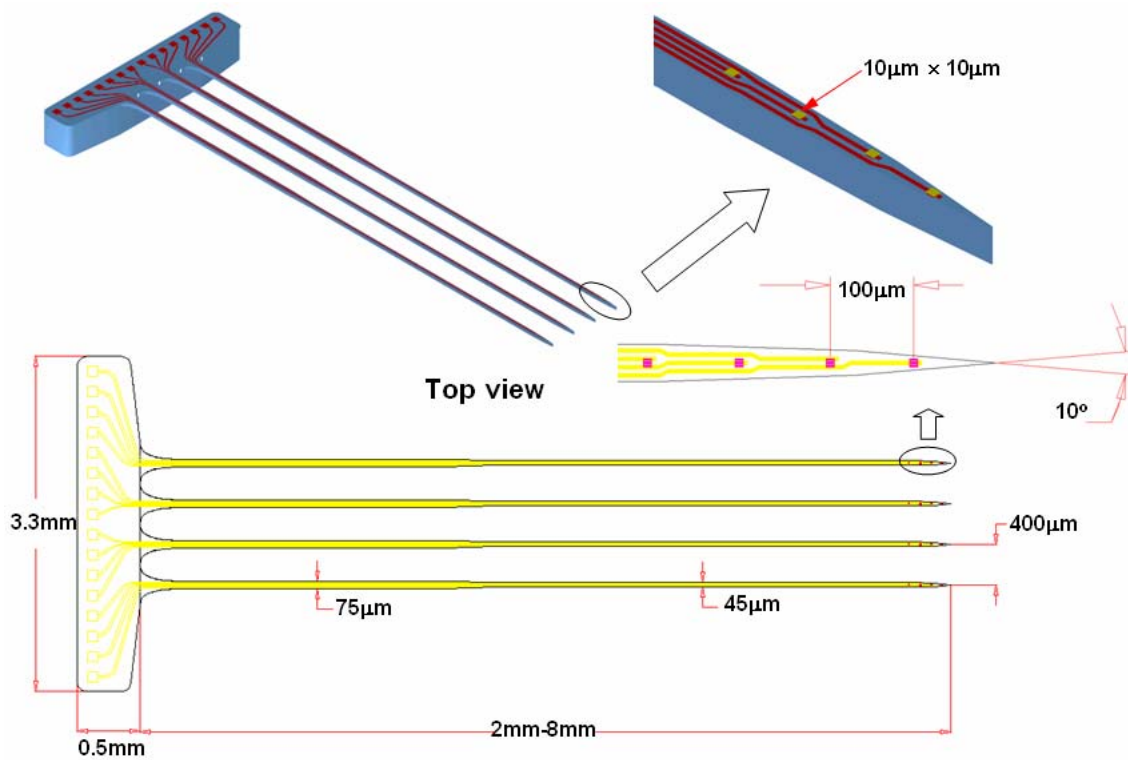
Figure 2-1   Schematic of the parylene probe structure and a typical CAD layout

The new parylene neural probes are made on a silicon substrate for mechanical support. Parylene insulating/protecting layers and metal layer with trace lines and electrode sensing sites are placed on top of the silicon substrate. Figure 2-1 shows the geometry design of a 2-D parylene neural probe array with 16 electrodes. The main design elements of the probe structure are: fine and pointed silicon shafts for penetration and insertion into neural

tissue, microelectrode sites of platinum distributed over the outermost section of the shafts; fine, narrowly spaced gold conductor traces ending in gold contact pads for external electrical interconnection; and a thicker silicon base plate as support for contact pads to allow easy handling of the probes.

In a typical design, there are four probe shafts in front of a thicker base plate. The thickness of the base plate is 520 μm – 530 μm, which is the thickness of the double-side-polished wafer. The shaft width is 45 μm at the outermost section, widening to 75 μm at the base plate. A curved corner at the base plate provides stronger mechanical support to the shafts. The shaft thickness is targeted to ~ 50 μm, but can be varied by controlling the DRIE etching. The shaft length varies from 2 mm to 8 mm and the shafts are spaced at 400 μm with four electrode sites on each of shanks. The electrode sites are 10 μm × 10 μm and distributed with 100 μm pitch. Platinum is selected as the electrode material, because of its chemical inertness. The shaft-tip taper angle is 10° with a chisel shape.

2.3   Fabrication

The probe fabrication process flow is shown in Figure 2-2, and is based on double-side-dry etching technology. The process starts with a double-side-polished silicon wafer: (a) First, XeF_2 etching is performed on top of the silicon surface. The silicon surface etched by XeF_2 has high roughness (Figure 2-3), which helps the parylene grab onto the silicon surface mechanically, greatly enhancing adhesion. (b) A 1.5 μm parylene C insulating layer is conformably deposited. (c) Cr/Au (~ 100 Å / 2000 Å) is thermally evaporated and patterned by lift-off to form the conduction traces (Figure 2-4). (d) A second

parylene C layer (~ 1.5 μm) is deposited as a protective layer; the electrode sites and bonding

pads are opened by plasma etching. (e) Ti/Pt (~ 200 Å / 2000 Å) is e-beam evaporated and

patterned by lift-off to form the electrode sites (Figure 2-5). (f) The parylene layers are

patterned along the probe shape by plasma etching. (g) Front-side DRIE (deep reactive ion

etching) (~ 100 μm deep) is performed to define the probe shape into silicon. (h) Back-side

DRIE defines the probe thickness, and releases the probes. (i) All the mask and sacrificial

photoresist is released.
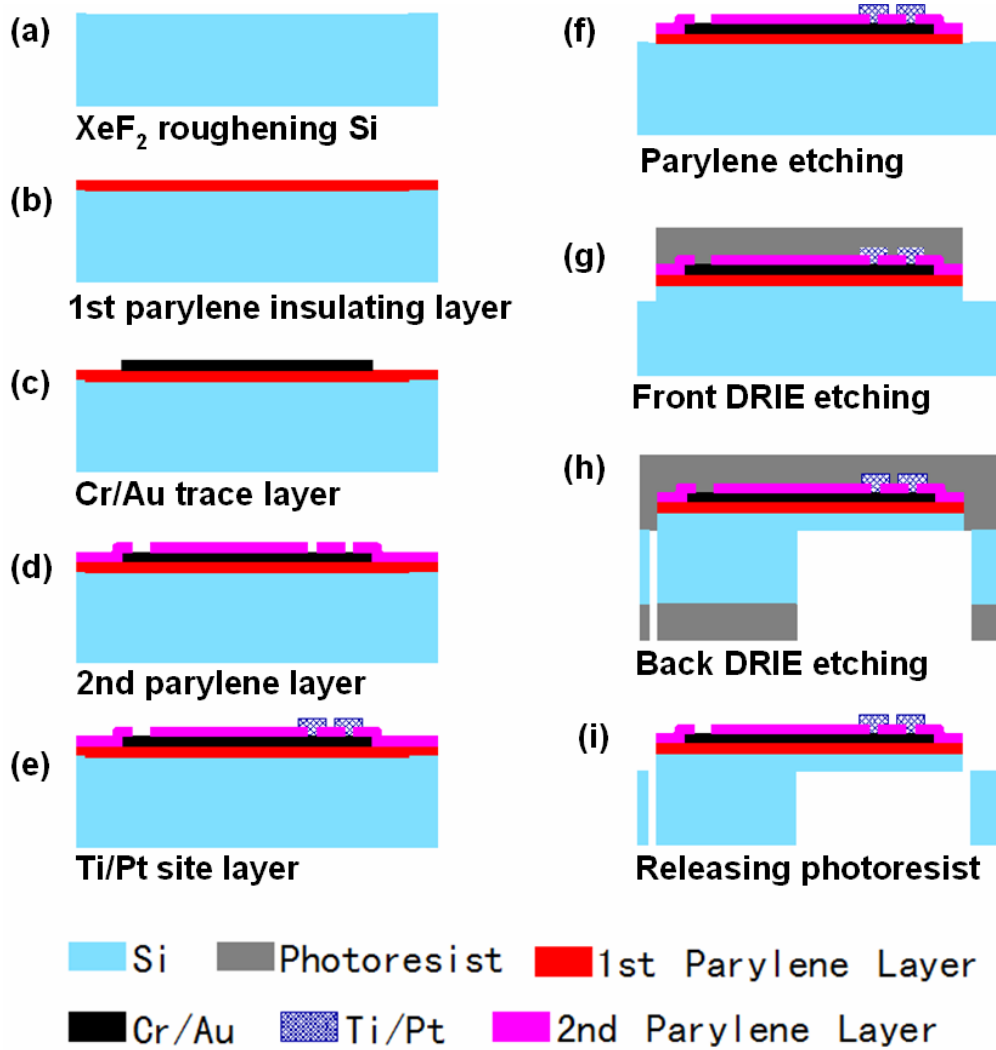
Figure 2-2　Fabrication process flow of the parylene neural probes

Instead of SOI wafers, less-expensive double-side-polished (DSP) wafers were used. Problems encountered included how to protect the probes during back DRIE etching and how to control the probes thickness without an oxide insulator layer. Experimental results show that the probes can be well protected by baked photoresist during back DRIE etching, as shown in Figure 2-6. In addition, by depositing protection photoresist on the back side of the finished probes to stop DRIE etching die by die, the probes' thickness can be well controlled within 5 μm on the whole wafer.
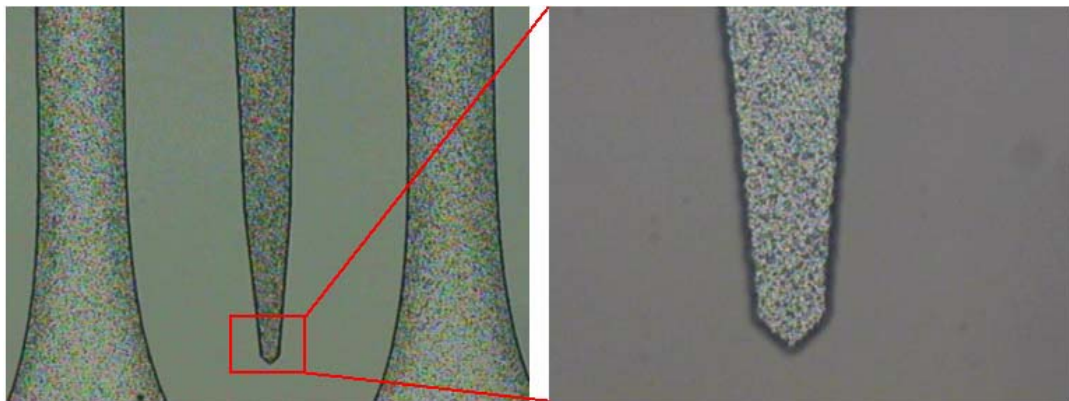
Figure 2-3　Silicon surface roughened by XeF$_2$ etching
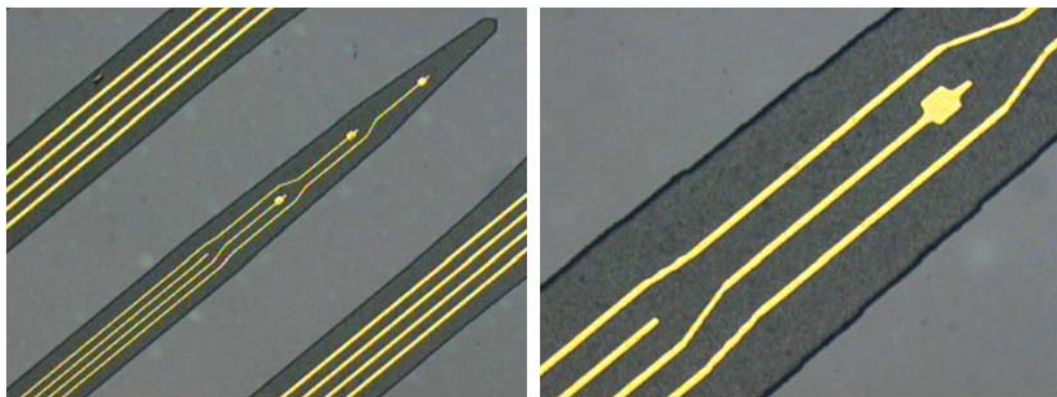
Figure 2-4　Au conductor trace line patterned by lift-off technology with minimum line

width of 2.5 μm
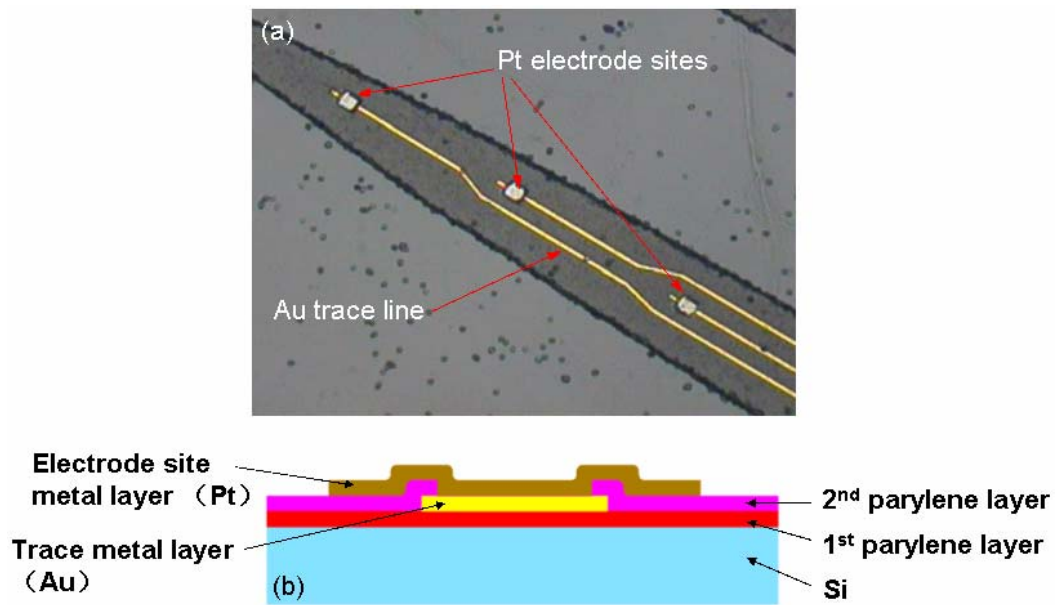
Figure 2-5 (a) Pt electrode sites patterned by lift-off technology; (b) cross section of

electrode site with two metal layers
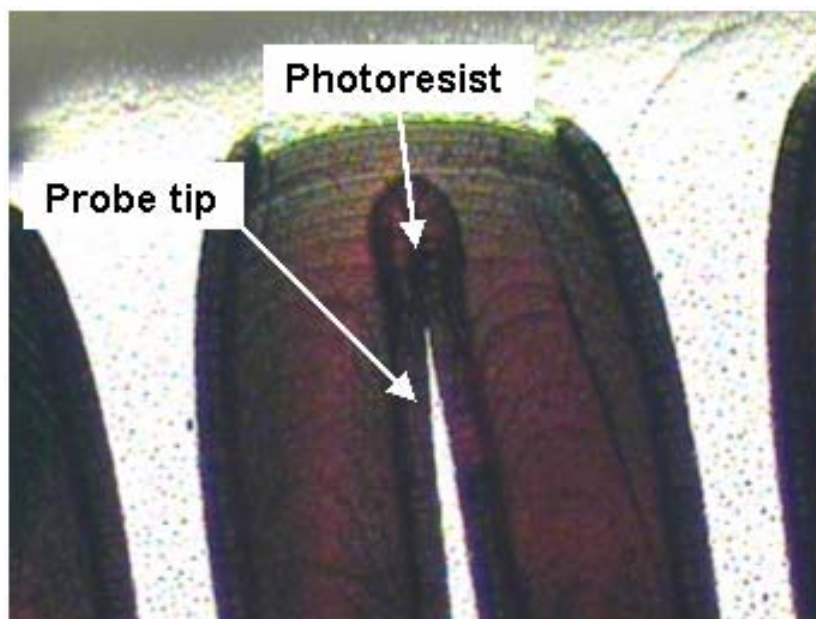
Figure 2-6 Photoresist protection for the probe tips during back DRIE etching

2.4   Testing Results and Discussions
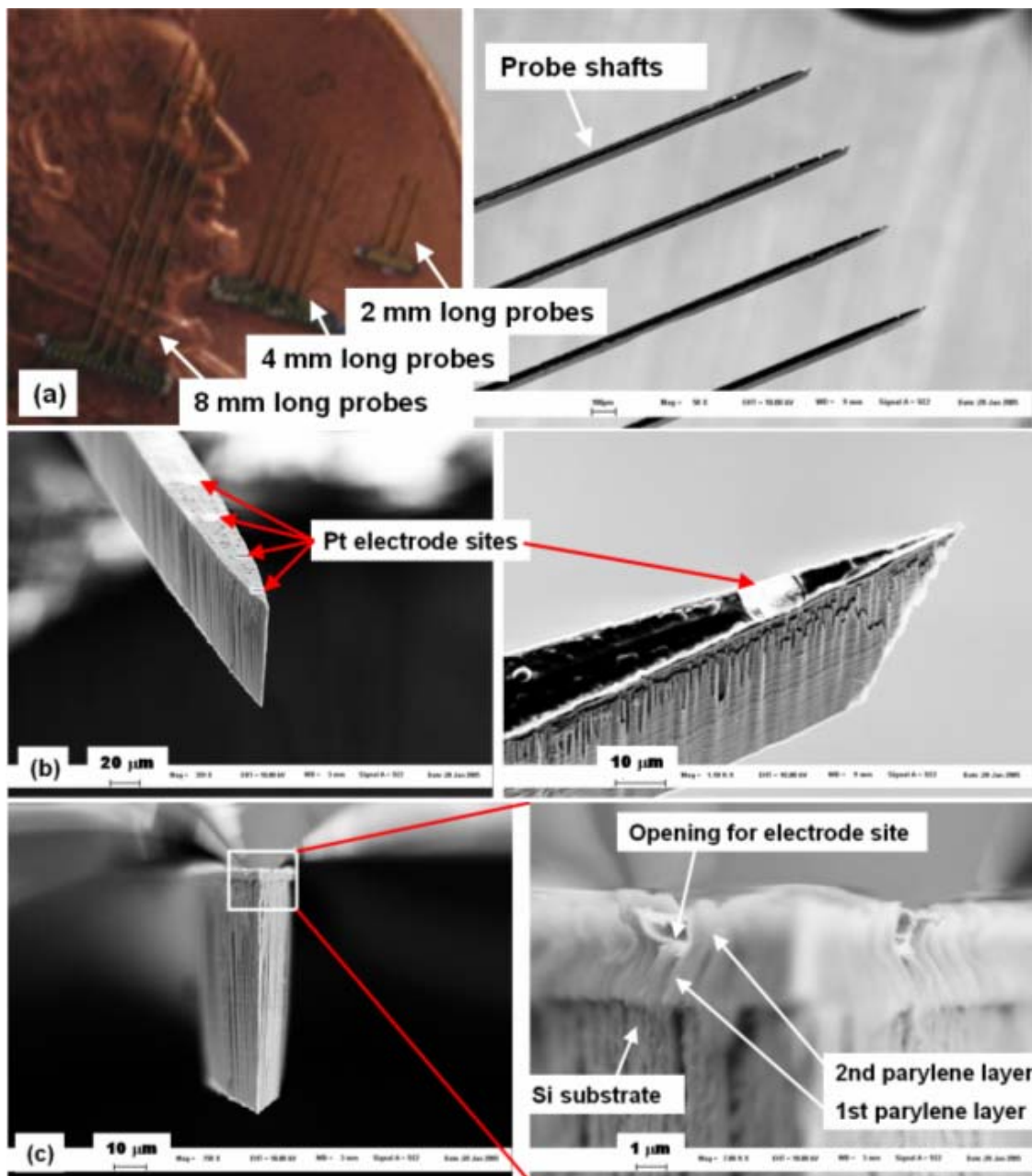
Figure 2-7   Optical and SEM pictures of the fabricated probes: (a) Pictures of the whole

probes and shafts; (b) SEM pictures of the probe tip with multiple electrode sites; (c) SEM

pictures of front-side view of the probe tip, showing the interface between parylene layer

and Si substrate and the interface between two parylene layers

Optical and SEM pictures of the fabricated probes are shown in Figure 2-7. The parylene layer shows very good adhesion on the roughened silicon substrate. No visible delamination or adhesion defect is found between the first parylene layer and the probe silicon substrate, nor between the two parylene layers. The probes were tested mechanically and electrically on rat cortex. The probes can be easily inserted into brain tissues without buckling or cracking. Electrode impedance is around 1.5 MΩ at 1 KHz. Neural signals were properly recorded. Figure 2-8 shows the sample filtered neural data recorded from one channel of the neural probe in rat cortex and the sample action potential waveforms.
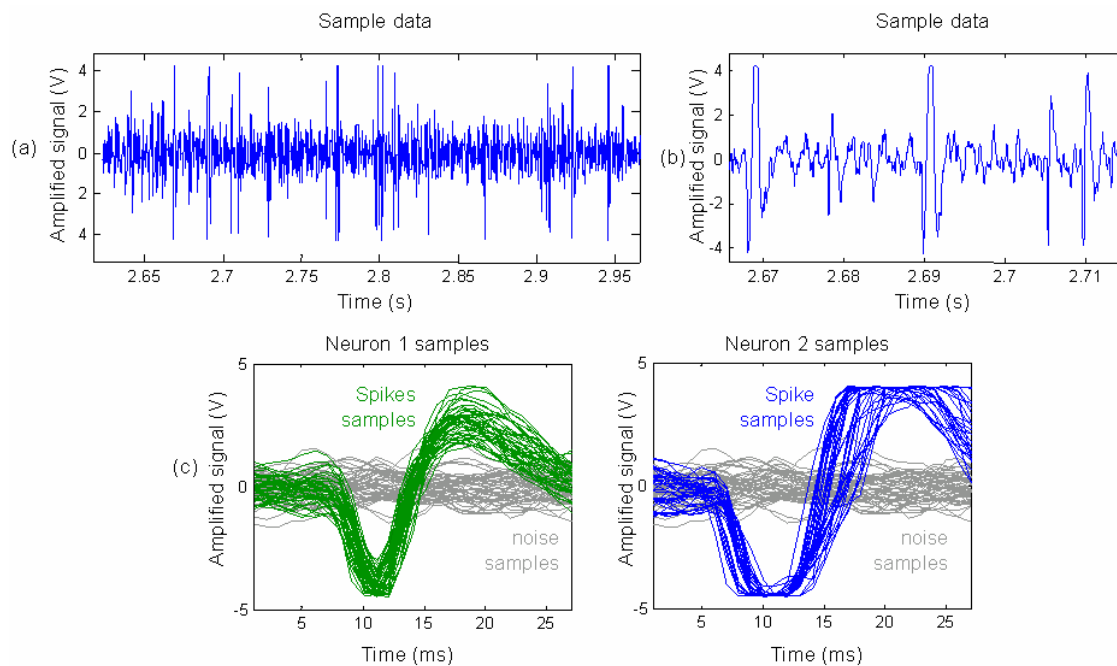
Figure 2-8   (a) Sample filtered neural data recorded from one channel of the neural probe in rat cortex; (b) sample filtered neural data recorded from rat cortex (Action potential waveforms from multiple neurons are visible in the signal.); (c) sample action potential waveforms, or "spikes," from two neurons detected in the neural signal (The waveforms are superimposed over samples of the base noise in the channel.)

2.5   Interconnection and Packaging

In order to interface the small probe chips with the comparatively larger amplifier system, the probes are packaged with a customized PC board. Figure 2-9(a) shows the schematic of the design for a 16-channel neural probe package. The probes are epoxy glued on the end of the PC board, wire bonding using conductive epoxy is used to make an electrical connection, and a big drop of epoxy coverage is used for mechanical support and protection. A commercial 16-channel (18-pin) male Omnetics 0.025" connector (Omnetics part number: #A8663-001) is used for the interconnection with the amplifier system. The Omnetics connector soldered on the PC board is shown in Figure 2-9(b). Figure 2-9(c) shows the packaged neural probes.
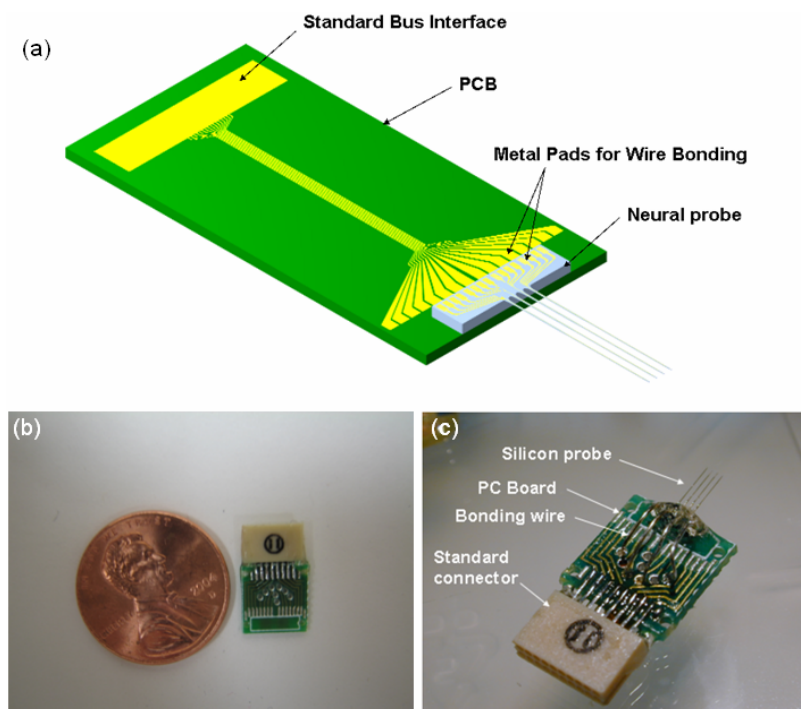
Figure 2-9   Schematic of 16-channel neural probe package; (b) PC board with 16-channel Omnetics connector; (c) packaged neural probes

2.6   Summary

We have designed, fabricated, and characterized a new parylene silicon neural probe. An all-dry process has been developed to fabricate the new multi-site neural probes with parylene insulating/protective layers. The parylene coating/etching process has been integrated with double-side DRIE etching to make the neural probes. Instead of silicon-on-insulator (SOI) wafers, less-expensive double-side-polished (DSP) wafers are used. With the advantages of parylene material, the probes perform with good mechanical and electrical properties. Neural signals were properly recorded from rat cortex.

CHAPTER 3

NEURAL PROBES WITH PARYLENE FLEXIBLE CABLES

3.1 Introduction

For chronic neural probes, communication between the implanted probes and the outside word must be achieved via a multichannel interconnect cable. Even if telemetry is used, a cable is still necessary to link the probes to a telemetry platform. Many attempts were made to solve this problem. A bundle of metal wires were used as the interconnect cable for the floating metal wire arrays [24] and the Utah electrode arrays [60], but the stiffness of the cable is too large for chronic implantation, especially for the high-density electrode arrays. The vast wire bonding work, which is used to connect the cables with the electrode arrays, severely limits the productivity. The flexible printed circuit was used by Norlin et al [65]. However, this cable cannot be fabricated as small as the size of the probe, and it still requires painstaking bonding and epoxy gluing work. One example of microfabricated

cable is the silicon-based ribbon cable [45, 56, 57] for the Michigan probes. Shallow boron diffusion is used to define the cable substrate. The overall thickness of the cables is 4–5 μm, which makes the cables flexible. However, the authors report that the cables are not robust. Low yield is also reported for longer-length cables because of the high aspect ratio. Obviously, polymer technology is a good substitute. We demonstrate an all-dry process to fabricate parylene cables monolithically integrated with probe arrays [119-121]. With the parylene flexible cables, the probes can be easily assembled to a high-density 3-D array for chronic implantation. PPO (Parylene-PCB-Omnetics connector) high-density packaging technology has been developed to bond the neural probes with standard commercial connectors.

3.2   Concept of New Parylene Probes

With the advantages of parylene technology, we propose to develop better chronic implantable neural probes, which will overcome the shortages and limitations of the current neural probes. Figure 3-1 shows the schematic of the design of novel parylene neural probes for chronic implantation. The key points of the improvement include: multiple electrode sites on the probe tip with parylene layer insulation and protection; monolithically integrated parylene flexible cable with multichannel to connect the front probe part to a silicon-based out-of-skull wireless communication unit; on-chip foundry IC embedded by a "Chip-Drop-In" parylene integration technique [110, 111] with electronic functions (e.g., preamplifier on the front probe part, multiplexer, AD converter, microcontroller, RAM, EPROM, wireless interface, power interface, and power management, etc.). All the fabrication processes are wafer-scale batch processes and compatible with standard MEMS processes. Because of the flexibility of the design, the length of the parylene cable can be

easily changed. That means extremely long flexible cable can be made for chronic implantation. A 3-D high-density probe array can be easily made by stacking the 2-D probe plates together, as shown in Figure 3-1. Because the parylene cables are already integrated with the probe, no bonding issue needs to be addressed here. Figure 3-2 shows how we could use the new parylene probes with parylene flexible cables for a chronic implantation. The front probe part is implanted under the skull, floating in the brain. Parylene flexible cables go through the skull and connect with the out-of-skull connection part. The flexible connection greatly reduces the damage either to the probes or to the brain due to the relative movement between the skull and the brain.
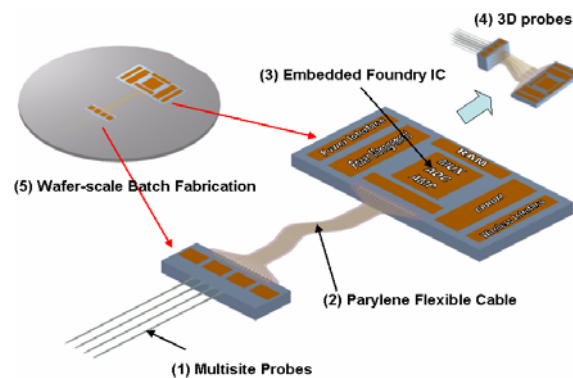
Figure 3-1　Schematic of the design of novel parylene neural probes for chronic
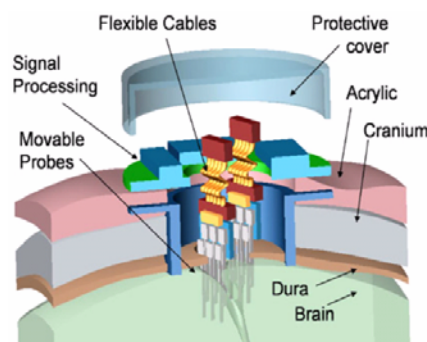
implantation

Figure 3-2　Schematic of cortical implantation using neural probes with parylene cables

3.3   Device Design
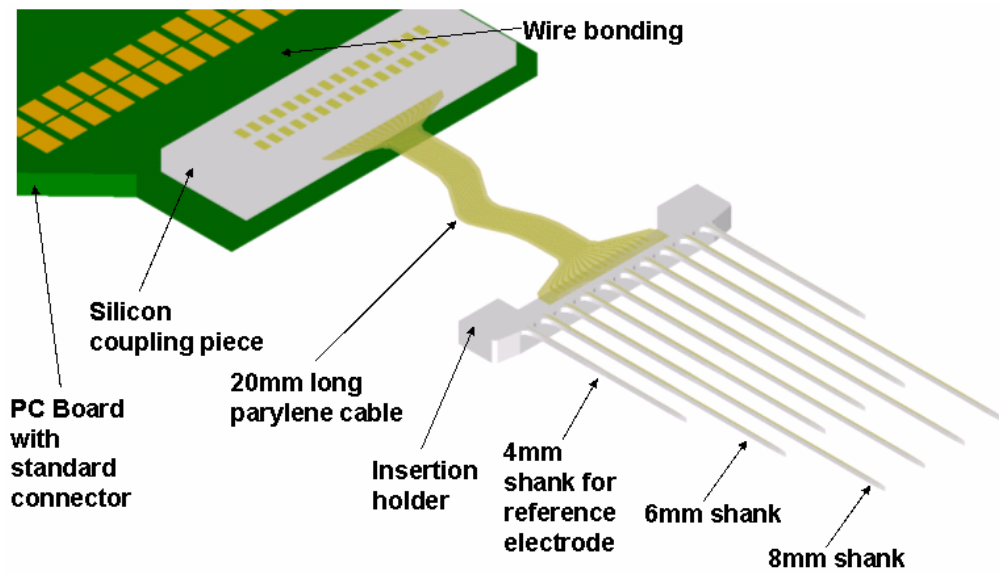
Figure 3-3   Schematic of the design of parylene neural probes with flexible cables for

chronic implantation in monkey cortex
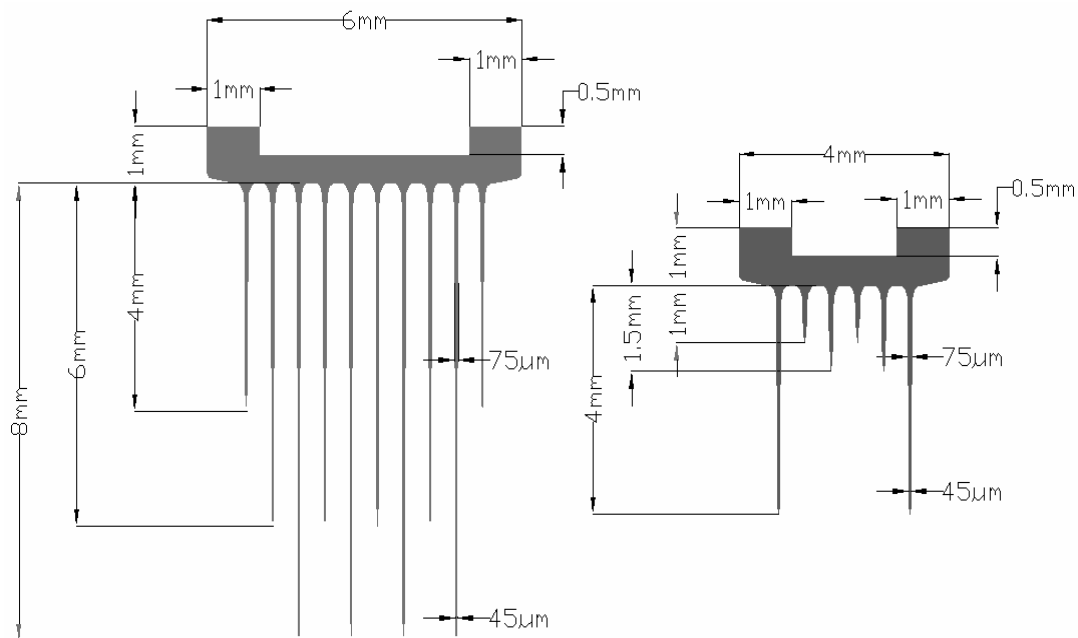
Figure 3-4   Layout design of the floating silicon probes

Schematic of the design of the parylene neural probes with flexible cables for chronic implantation in monkey cortex is shown in Figure 3-3. The front part is made up of floating silicon probes, which are connected with the silicon coupling part via a 20 mm long flexible parylene cable. Wire bonding is used to electronically connect the silicon coupling to a small PC board. Figure 3-4 shows two layout designs for the floating silicon probes: long-shank probes and short-shank probes, aiming at different neuron layers in the monkey cortex. For the long-shank probes, eight shanks (6 mm and 8 mm long, alternately, 500-μm spacing) with four gold electrode sites each (20 μm × 20 μm in 300μm spacing) are placed in front of a thicker plate, resulting in a 32-site 2-D probe array. Reference electrodes are on the two outside 4-mm-long shanks. The short-shank probes have four shanks (1 mm and 1.5 mm long, alternately, 500-μm spacing) with four gold electrode sites each (20 μm × 20 μm in 200-μm spacing), therefore, a 16-site 2-D probe array is made. Two outside 4-mm-long shanks are designed as the reference electrodes and the anchors. In this new design, multi-site electrodes are sandwiched by insulating/protecting parylene layers. The target shaft thickness is 100 μm; the shaft width is 75 μm at the bottom and 45 μm at the outermost section. The lateral taper angle of the chisel-shaped tip is designed to 10°. The width of the trace lines on the outermost shaft section is 2 μm.

With the 20-mm-long parylene flexible cable, the 3-D probe array can be easily assembled by stacking multiple 2-D probe plates together. Figure 3-5 shows an illustration of a 3-D probe array with 8 × 2 probes, and 64 sensing electrodes, and 4 reference electrodes.
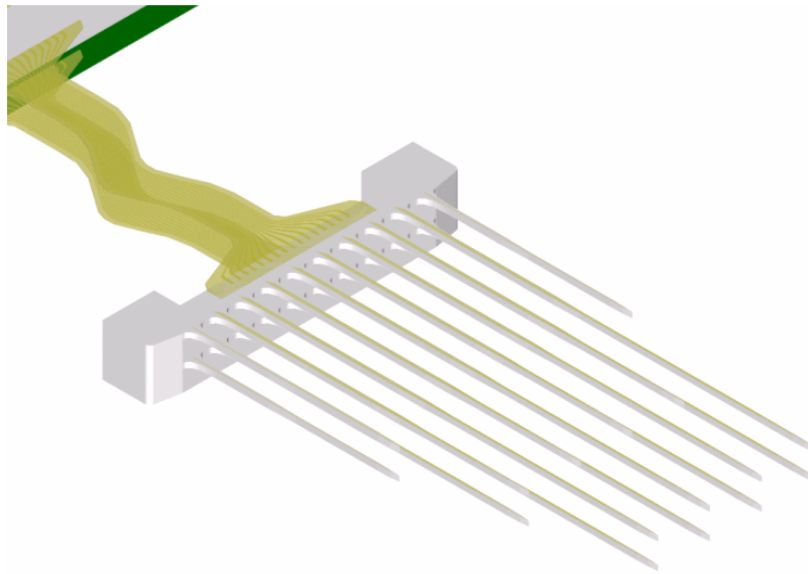
Figure 3-5   Illustration of the use of parylene flexible cable to make 3-D neural probe

array

3.4   Fabrication Process
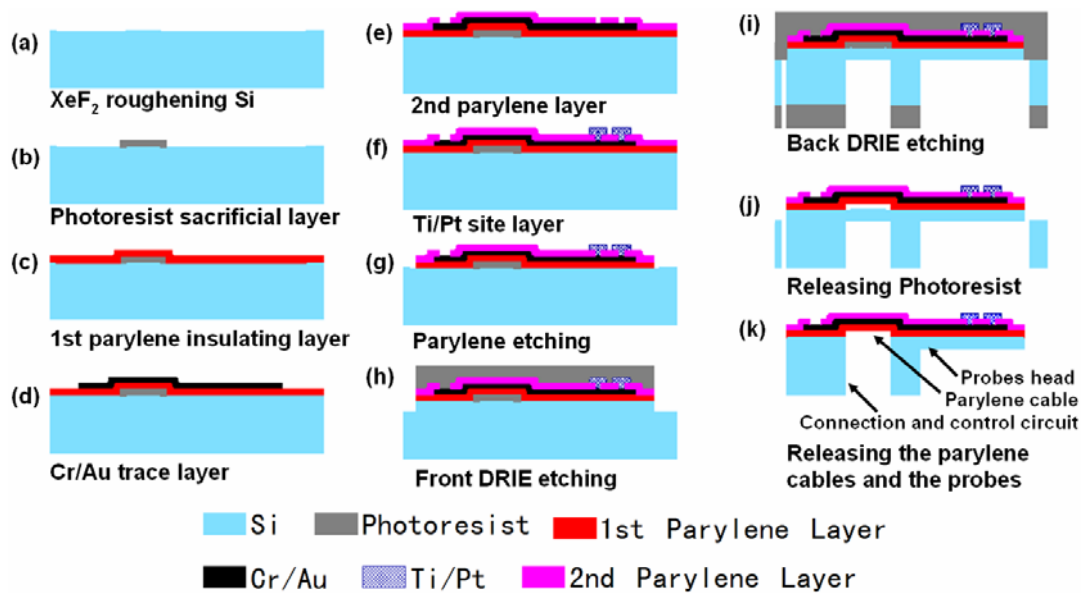
Figure 3-6   Fabrication process flow of the parylene neural probes with monolithically

integrated parylene flexible cables

The fabrication process flow of the parylene neural probes with monolithically integrated parylene flexible cables is shown in Figure 3-6, and is based on DRIE double-side-etching technology. Lift-off parylene skin technique is used to fabricate the flexible cables. Instead of silicon-on-insulator (SOI) wafers, less-expensive double-side-polished (DSP) wafers are used. (a) XeF_2 etching is performed on the probe's top silicon surface to enhance the adhesion between silicon and parylene. (b) A photoresist sacrificial layer is patterned on the place where the parylene cables will be placed. (c) A 8-μm parylene C insulating layer is conformably deposited. (d) Cr/Au (~ 200 Å / 2000 Å) is thermally evaporated and patterned by lift-off to form the conduction traces. (e) A second parylene C layer (~ 2 μm) is deposited as a protective layer; the electrode sites and bonding pads are opened by plasma etching. (f) Ti/Pt (~ 200 Å / 2000 Å) is E-beam evaporated and patterned by lift-off to form the electrode sites. (g) The parylene layers are patterned along the probe shape by plasma etching. (h) Front-side DRIE (deep reactive ion etching) (~ 150 μm deep) is performed to define the probe shape in silicon. (i) Back-side DRIE defines the probe thickness and releases the probes. (j) All the mask and sacrificial photoresist is released. (k) The thin silicon film underneath the parylene cables is broken to release the probes.

A stepper mask stitching technology has been used to route the 20-mm-long parylene cables. Because the die size for the stepper in the Caltech Micromachining Lab is 10 mm × 10 mm, three dies are combined together for the whole device fabrication, as shown in Figure 3-7. The connection area of the two neighbor dies will be exposed twice by stepper, so compensation in mask design is necessary for high-resolution devices. The stepper exposure time and development time must also be tested and precisely controlled. Figure 3-8 consist of the pictures of the processing wafer, showing the combination of the

stitched dies; apparently the throughput of the process is relatively low. Only 14 long-shank

probes and 14 short-shank probes can be processed on one four-inch wafer.
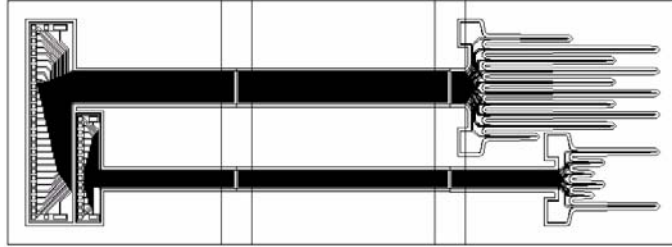
Figure 3-7   Mask design of the parylene neural probes with parylene flexible cables using

stepper mask stitching technology
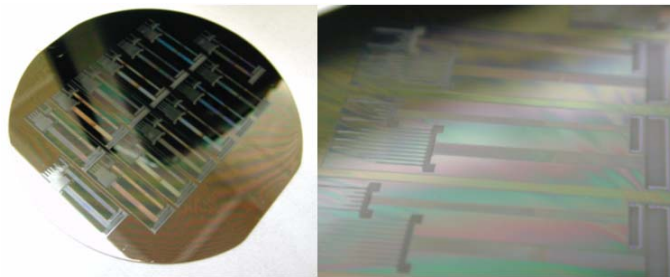
Figure 3-8   Pictures of the processing wafer for the parylene neural probe with parylene

flexible cables

3.5   Fabrication Results

Optical and SEM pictures of the fabricated probes are shown in Figure 3-9. The

parylene layer shows very good adhesion to the roughened silicon substrate. No visible

delamination or adhesion defect is found between the first parylene layer and the probe

silicon substrate, nor between the two parylene layers.
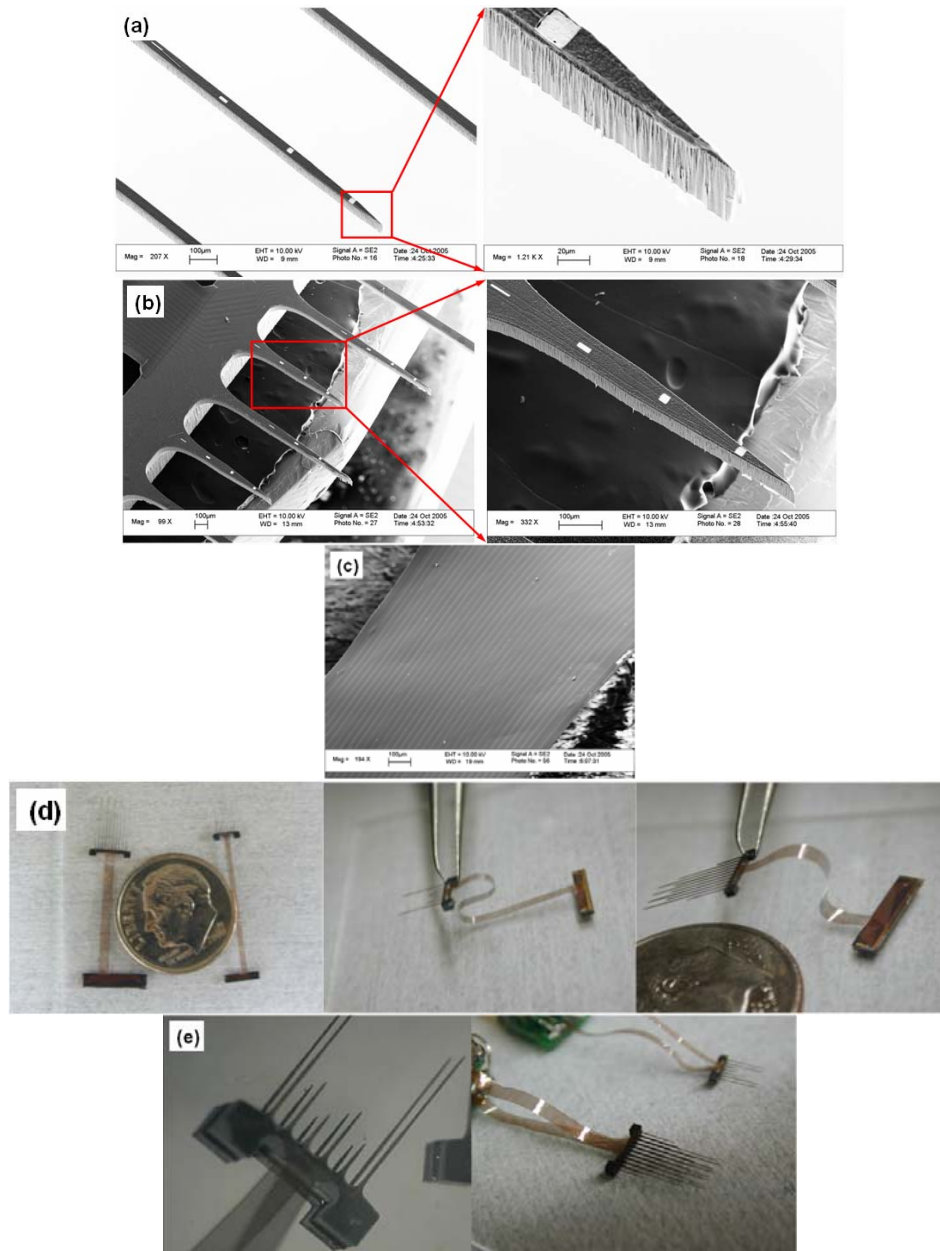
Figure 3-9   Pictures of the fabricated probes: (a) SEM pictures of the long-shank probes;

(b) SEM pictures of the short-shank probes; (c) SEM picture of the parylene cable; (d)

optical pictures of the 2-D probe arrays with parylene cables; (e) optical pictures of the 3-D

probe arrays (4 × 2 with 32 electrodes and 8 × 2 with 64 electrodes) stacked by two 2-D

probe plates

The probes were tested mechanically and electrically on rat cortex. The probes can be easily inserted into brain tissues without buckling or cracking. The 3-D probe arrays (4×2 with 32 electrodes and 8×2 with 64 electrodes) with parylene cables are shown in Figure 3-9(e). The parylene cable is shown in Figure 3-9(c), which is 20 mm long, 1.5 mm wide, and has 34 parallel Cr/Au trace lines (20 μm wide) inside. Longer cables and more trace lines can be made using the same method. The parylene cable is monolithically fabricated with a probe array and an out-of-skull connection part, and links the two parts together mechanically and electrically.

3.6   PPO High-density Packaging Technology

3.6.1   Current Packaging Issues

As we described, the parylene flexible cables go through the skull and link the front probe part with the out-of-skull connection part. Because wireless technology has not been ready for most of real applications, the interconnection between the out-of-skull connection part and the stack amplifier system is still a big challenge at this time, especially for the high-density electrode array (e.g., 100 electrodes).

The devices described in Chapter 2 and in the previous part of this chapter are designed to use a traditional wedge bonder to bond gold wires to the metal pads on the connection part of the devices, and to connect to the copper pads on the PCB. The gold-wire wedge bonder uses ultrasonic energy and press force from the bonding probe tip to form the wedge bond. Figure 3-10(a) shows the cross section of the metal pads on the connection part. Instead of SiO_2, we use parylene as the insulation layer under the metal pads. Because parylene is a soft material with Young's modulus of 2.76 GPa, experimental results show that the parylene layer cannot survive under the press force from the bonding

probe during the wedge bond. As a result, both the metal pads and the parylene layer are scratched and destroyed by the bonding probe tip (Figure 3-10(b)), causing the bonding failure. An alternative solution for bonding the devices is to use conductive epoxy, Figure 3-10 shows one device bonded by gluing metal wires on the bonding pads using conductive epoxy. But the resolution of the conductive epoxy bonding is very low; also making this temporary solution no good for high-density packaging.
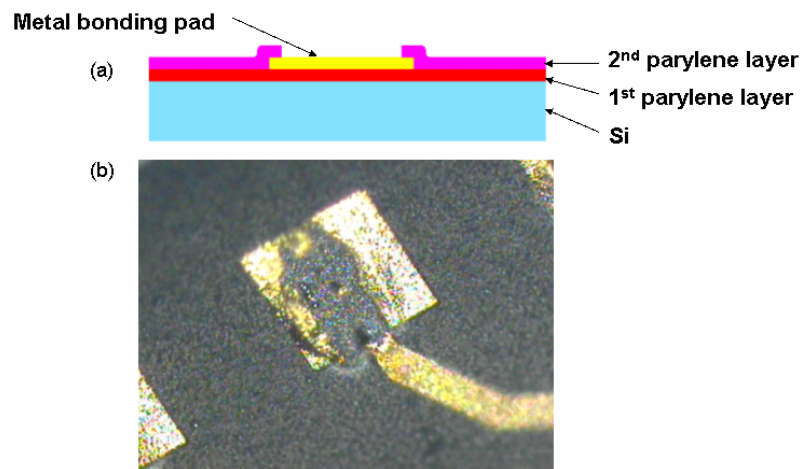
Figure 3-10   (a) Cross section of the metal pads for the wire bonding design; (b) metal pad destroyed by wedge bond
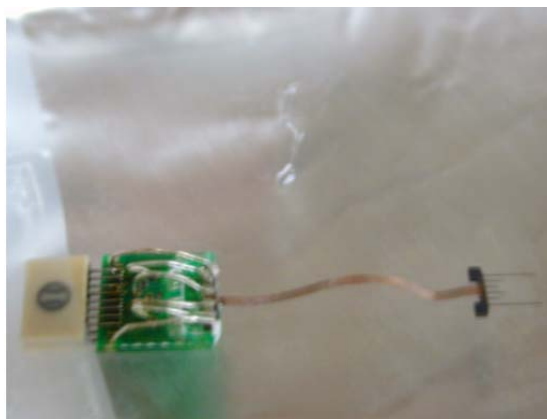
Figure 3-11   Neural probes bonded using conductive epoxy
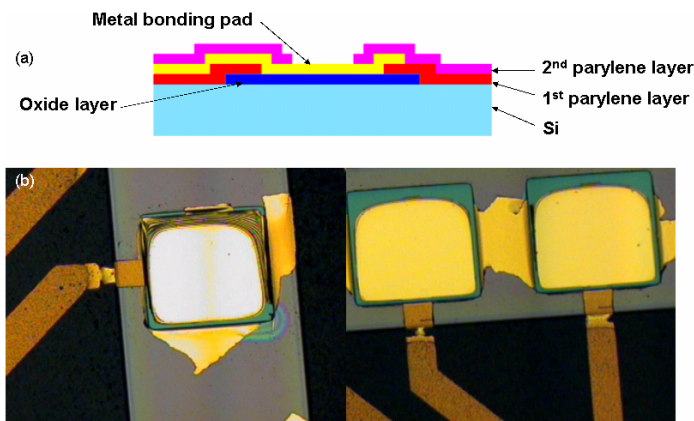
Figure 3-12   (a) Cross section of the metal pads with SiO_2 layer underneath; (b) pictures of the process problem of the lift-off metal patterning over a step height

From above discussions, we can see that the soft parylene layer under the metal pads cause the failure of the wedge bond. A modification in device fabrication has been made by substituting parylene with a SiO2 layer under the metal bonding pads to provide a solid support for wedge wire bonding. Figure 3-12(a) shows the cross section of the modified device. However, a new fabrication problem arises during the lift-off metal patterning. The lift-off process is used to pattern the metal layer in order to achieve high resolution of the trace lines on the neural probe shanks. The time for development needs to be precisely controlled. However, due to the step height between the bonding pads and the trace lines, some photoresist residue are unable to be developed away around the edges and corners of the SiO_2 area, which causes discontinuity between the bonding pads and the trace lines in that area. Figure 3-12(b) shows the bonding metal pads after patterning the metal layer. Apparently the solution of adding SiO2 layer under the bonding metal pads is not feasible.

3.6.2   New Concept of PPO Packaging

A new concept of PPO (Parylene-PCB-Omnetics connector) high-density packaging technology has been developed for the parylene neural probe's interconnection with the amplifier system. Figure 3-13 shows a commercially available setup for interconnection to Plexon data acquisition systems with Omnetics connectors. The Nano's Omnetics connectors have high-density pins—for example, the center-to-center distance of the 16-channel (18-pin) male Omnetics 0.025" connector (Omnetics part number: #A8663-001) is only 0.025 in (635 μm). If we can match and connect the bonding metal pads of the neural probes with the pins of an Omnetics connector, a direct high-density interface can be made for the data acquisition system.
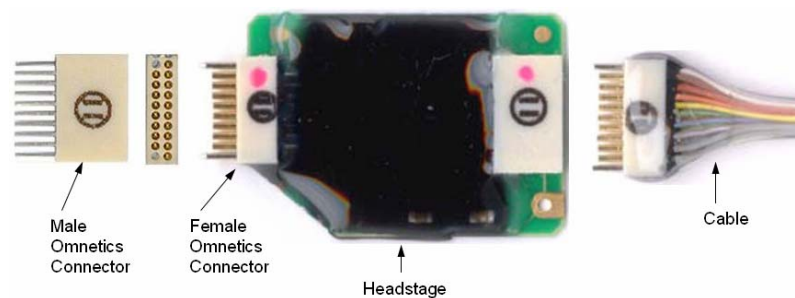
Figure 3-13   Interconnections to Plexon data acquisition systems with Omnetics

connectors

Figure 3-14 shows the schematic of the PPO (Parylene-PCB-Omnetics connector) high-density packaging concept. The neural probe's connection is changed to a parylene sheet without silicon substrate. Metal pads with through holes in the center are built on the parylene connection sheet. The pins of Omnetics connectors go through a customized PC board and into the holes in parylene connection sheet. Conductive epoxy is used to make the electrical connection between the metal pads on the parylene connection sheet and the

pins of the Omnetics connectors. A drop of biocompatible epoxy is then used to provide mechanical protection of the bonding. The PC board provides the mechanical support of the connection.
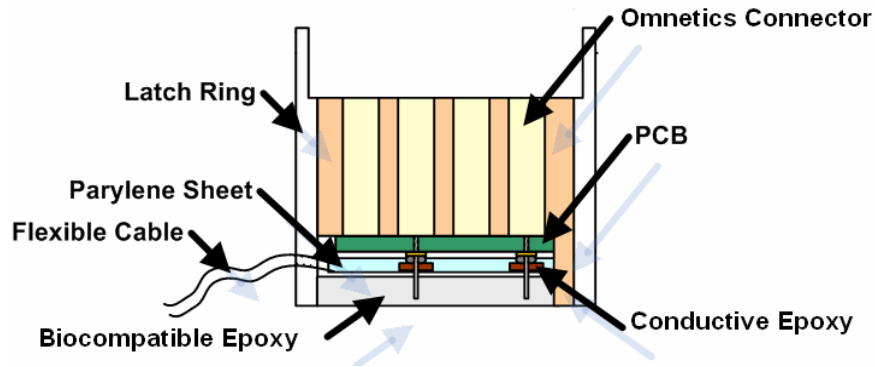
Figure 3-14　Schematic of the PPO (Parylene-PCB-Omnetics connector) high-density packaging concept

3.6.3　Neural Probes with PPO High-density Packaging

3.6.3.1　Device Design

Parylene neural probes are designed for chronic implantation in rat cortex. The new design includes a parylene sheet connector for PPO high-density packaging. Figure 3-15 shows the layout of the design. Figure 3-15(a) is the layout of the whole device, Figure 3-15(b) is the layout of the front probe part and Figure 3-15(c) is the layout of the parylene sheet connector.

The neural probes are designed for sensing the neuron activities in the surface layer of the rat cortex. On one 2-D probe plate, there are totally seven probes shanks with two 600 μm long, two 700 μm long, two 800 μm long and one 900 μm long. The probes are placed in a "V"-shape with the longest one in the center and the shorter ones on the sides. Compared with other probes with the same length, the "V"-shape design has proven to

have the best insertion ability by in vivo test. Another benefit of the "V"-shape design is that the electrodes are distributed on probe shanks with different lengths, therefore a single implanted device could test neuron activities at different depths. The separation of the probe shanks is 400 μm, the target shank thickness is 100 μm, and the shank width is 75 μm. The lateral taper angle of the chisel-shaped tip is designed to 10°. Two types of electrodes are designed for different applications: a high-impedance electrode is 5 μm × 5 μm; while a low impedance electrode is 400 μm^2 in a trapezoid shape. The trapezoid-shaped electrode design places the electrode as close to the probe tip as possible. All the sensing electrodes are in 125 μm space. Two reference electrodes are placed on the base of the 800-μm-long shanks. The reference electrode is in a rectangle shape with the size of 170 μm × 20 μm.
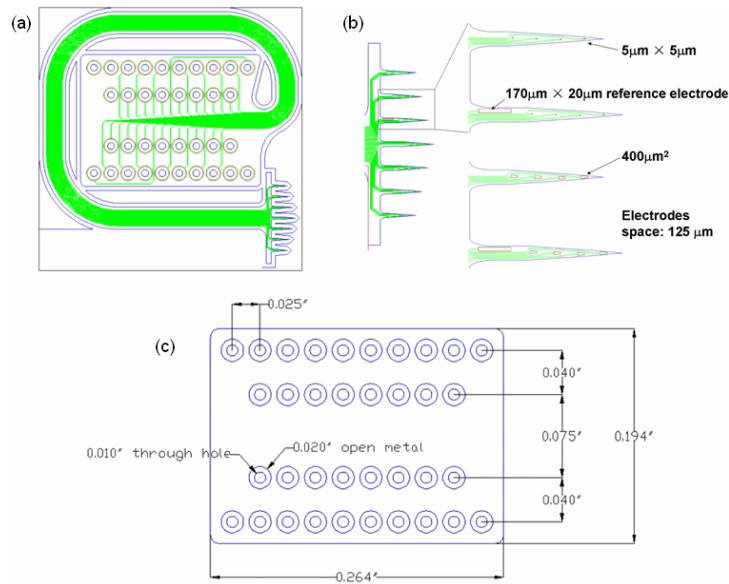
Figure 3-15   Layout design of the neural probes for rat chronic implantation with PPO high-density packaging: (a) layout of the whole device; (b) layout of the front probe part; (c) layout of the parylene sheet connector

We designed the cable of the new design in a round route fashion instead of a straight cable to minimize the use the mask area and to increase the fabrication throughput.

As shown in Figure 3-15(c), the parylene sheet connector design includes the metal pads matching two parallel 16-channel (18-pin) male Omnetics 0.025" connectors. The diameter of the through hole and the inner diameter of the metal pad ring is 0.01 in. The outer diameter of the metal pad ring is 0.02 in. The center or center distance between two metal pad rings is 0.025 in.

3.6.3.2 Fabrication Process

The fabrication process flow of the parylene neural probes with PPO high-density packaging is shown in Figure 3-16. The same double-side DRIE etching and the lift-off parylene skin technique are used. The process starts with a double-side-polished wafer. XeF_2 silicon etching is first performed on the silicon surface. A photoresist sacrificial layer about 1.5 μm thick is then patterned on the surface where the flexible cables and parylene sheet connector will be placed. A parylene C insulation layer about 8 μm thick is coated, and a Cr/Au (~100 Å / 2000 Å) metal layer is then thermally evaporated and patterned by lift off. Another parylene C protective layer about 2 μm thick is coated and patterned using RIE O_2 etching to open the electrode sites and metal bonding pads. Another RIE O_2 etching is then performed to etch through both parylene layers and define the shape of probes, parylene cables, and parylene sheet connectors. The through holes on the parylene sheet connectors are etched at the same time. Front-side DRIE is performed to etch into silicon substrate about 150 μm deep. Back-side DRIE etch defines the thickness of the neural probes (~ 100 μm). All the mask and sacrificial photoresist is released in ST-22 solvent.

The probe is released by breaking off the silicon wafer. Finally an annealing process (200 ^{o}C in vacuum oven for 48 hours) is performed to enhance the adhesion between the two parylene layers.
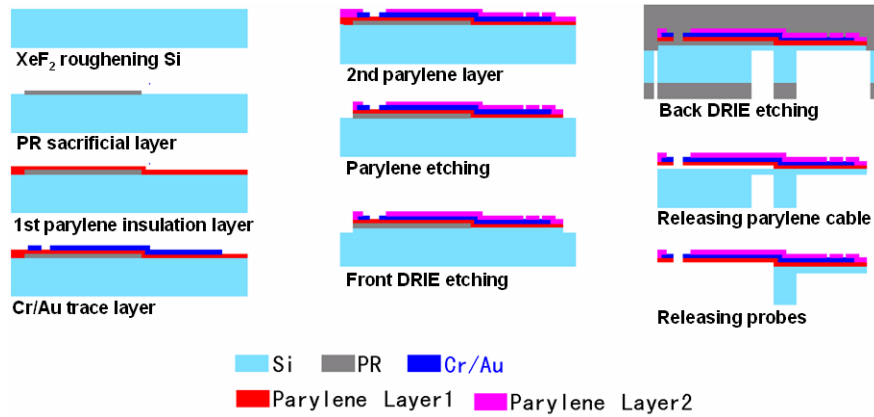
Figure 3- 16   Fabrication process flow of the parylene neural probes with PPO

high-density packaging

3.6.3.3   Fabrication Results

The fabricated parylene neural probes with PPO high-density packaging are shown in Figure 3-17: (a) shows the optical pictures of the fabricated devices, (b) shows the sensing electrodes after being opened by RIE O_2 plasma etching, (c) shows the SEM pictures of the probes with 400 μm^2 trapezoidal electrodes, (d) shows SEM pictures of the probes with 5 μm × 5 μm electrodes, and (e) shows the SEM pictures of the parylene flexible cables. The parylene flexible cable is about 2.5 cm long and 830 μm wide with 30 gold trace lines (10 μm) inside. As shown in Figure 3-17(a), the parylene cable is very flexible and can be easily stretched, while the parylene sheet connector maintains a flat shape which makes it very easy to match and assemble with the PCB and Omnetics connectors.
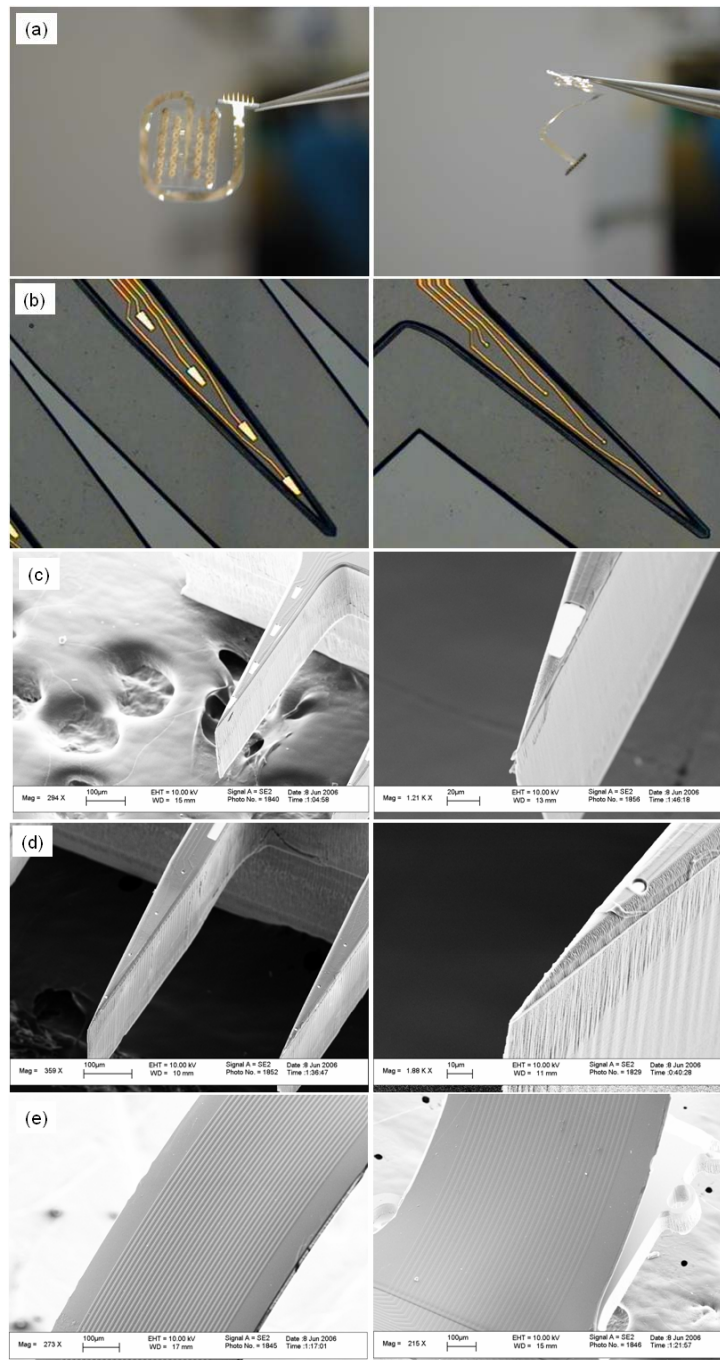
Figure 3-17　(a) Optical pictures of the fabricated neural probes with PPO high-density packaging; (b) the sensing electrodes after being opened by RIE O_2 plasma etching; (c) SEM pictures of the probes with 400 μm^2 trapezoid electrodes; (d) SEM pictures of the probes with 5 $\mu m \times 5 \mu m$ electrodes; (e) SEM pictures of the parylene flexible cables

3.6.3.4 Device Packaging

The parylene connection sheet of the device and the customized PCB have the same through holes, matching the position and size of the Omnetics connector pins. To bond the device, Omnetics connectors are first assembled on the PCB; the parylene sheet connector is then assembled along the pins of Omnetics connectors to the PCB, as shown in Figure 3-18(a). The PCB provides mechanical support of the packaging. Conductive epoxy is then painted along the Omnetics connector pin and on the metal pad of the parylene sheet connector to make electrical connection, as shown in Figure 3-18(b and c). After the conductive epoxy dries out, a drop of biocompatible epoxy is applied to provide mechanical protection of the packaging. Figure 3-19 shows the packaged devices with PPO packaging technology. Thirty channels are packaged using two 18-pin Omnetics connectors; 6 pins are left unused for this design.
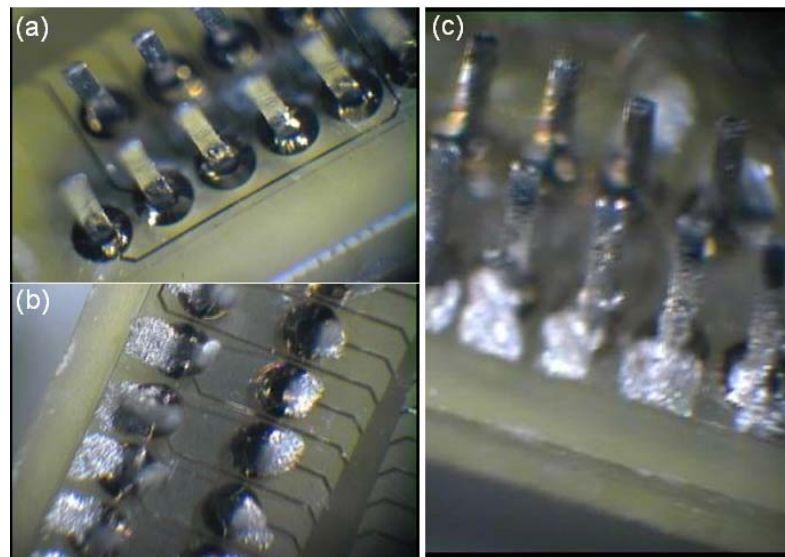
Figure 3-18   Assembled PPO connector with parylene sheet, PCB, and Omnetics connector; (b) top view of the PPO packaging after conductive epoxy is painted; (c) side view of the PPO packaging after conductive epoxy is painted
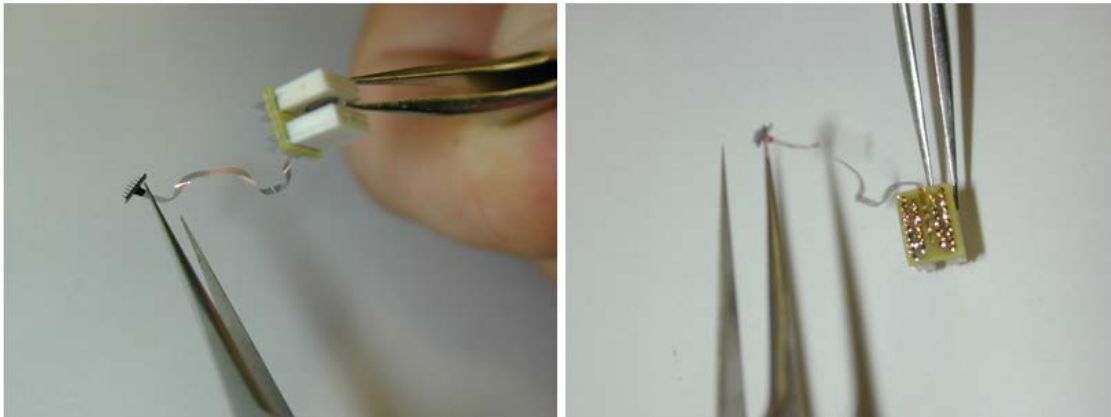
Figure 3-19   Packaged neural probes with PPO high-density packaging technology

3.7   Testing of the Neural Probes

3.7.1   Neural Probe Shank Rigidity Test

Current applications of neural probes for chronic implantation in monkey or human brain require a strong mechanical property in order to penetrate the brain pia. Other silicon probes such as the ones from Michigan, are made by wet etching, which limits the thickness of probe shanks. Michigan probes also require special guide tools for an open-pia insertion due to the mechanical weakness of it, which causes more severe damage to the brain tissues.

Our new double-side DRIE etching fabrication technology allows us to make the silicon probes strong enough to penetrate primate pia. The probe geometry design is very important for the mechanical structure of strong probes. Figure 3-20 shows one example of broken probe shanks after insertion through monkey pia due to failure of the weakness in probe structure. At the same time, however, the probe geometry has to be small enough to reduce insertion damage. Thus, animal test was conducted to help us balance these two trade-offs [122].
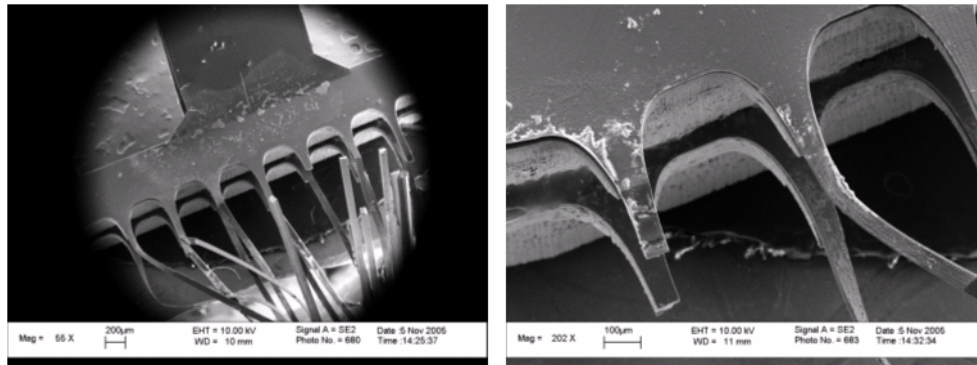
Figure 3-20   Broken probe shanks after insertion through monkey pia due to failure of the weakness in probe structure

In order to test the mechanical properties of the new neural probes, testing silicon probes are designed for in vivo tests. The testing silicon probes are the same as the complete devices except for the metal electrodes and parylene cables. A parylene layer is placed on top of the silicon probes' shank, so that the testing probes perform with the same mechanical properties as the complete device. As shown in Figure 3-21, testing probes with different geometry parameters (e.g., probe shank length L, probe shank base width W, probe shank thickness T, top parylene layer thickness T1) have been fabricated for in vivo rigidity testing. Fabricated testing silicon probes are shown in Figure 3-22. Probes with 5 shanks and 9 shanks in a "V"-shape have been made.
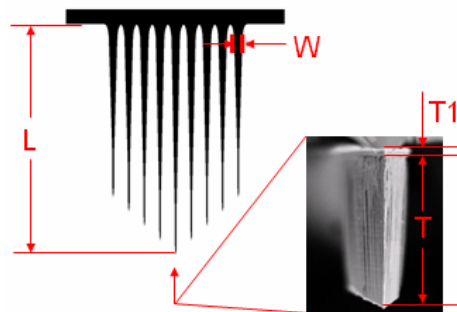
Figure 3-21   Parameters of the silicon probes for rigidity testing
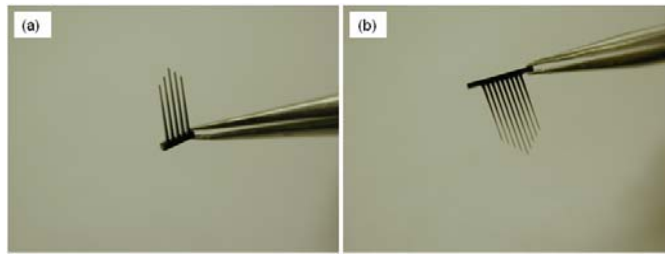
Figure 3-22   Fabricated silicon probes for rigidity testing: (a) probes with 5 shanks; (b)

probes with 9 shanks

Silicon probes with different geometries are tested for penetration of rat dura by hand insertion. The test results are shown in Table 3-1. The probes without top parylene layer are very brittle and all failed in the in vivo tests. The results prove that the parylene insulating/protecting layer greatly improves of the probe's mechanical properties. Figure 3-23 shows the probes which were successfully inserted into rat cortex through dura. A chronic implantation of the silicon probe in a rat brain tested probe biocompatibility. The animal recovered very well after 7 days. As is common knowledge, rat dura is slightly thicker than primate pia. A successful chronic implantation in monkey cortex by penetrating monkey pia was done using a complete device with metal electrodes and flexible parylene cables (Figure 3-24).
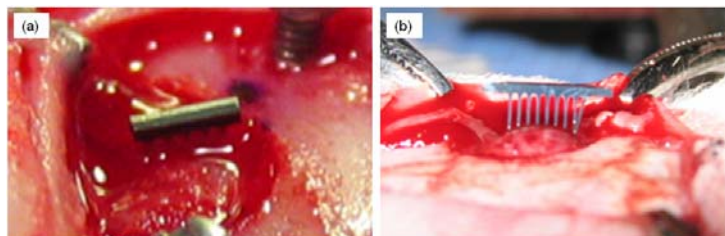
Figure 3-23   The probes which were successfully inserted into rat cortex through dura: (a)

probes with 5 shanks; (b) probes with 9 shanks. Pictures show the shank on the right side

was broken, because it hit the skull during insertion

Table 3-1   Silicon probe rigidity in vivo test results.

Probe No.	Probe shank length L (mm)	Probe shank base width W (μm)	Probe shank thickness T (μm)	Top parylene layer thickness T1 (μm)	Testing results (penetrating rat's dura)
1	1.0, 1.5	75	150	10	successful
2	6.0, 6.5, 7.0, 7.5, 8.0	75	150	10	failed
3	8.0	100, 120, 140,160,180,200	200	0	failed
4	6.0, 6.5, 7.0, 7.5, 8.0	200, 250	240	10	successful
5	6.0, 6.5, 7.0, 7.5, 8.0	175	100, 120, 140, 160, 180, 200	10	successful
6	6.0, 6.5, 7.0, 7.5, 8.0	150	100, 120, 140, 160, 180, 200	10	successful
7	6.0, 6.5, 7.0, 7.5, 8.0	125	100, 120, 140, 160, 180, 200	10	failed
8	6.0, 6.5, 7.0, 7.5, 8.0	100	100, 120, 140, 160, 180, 200	10	failed
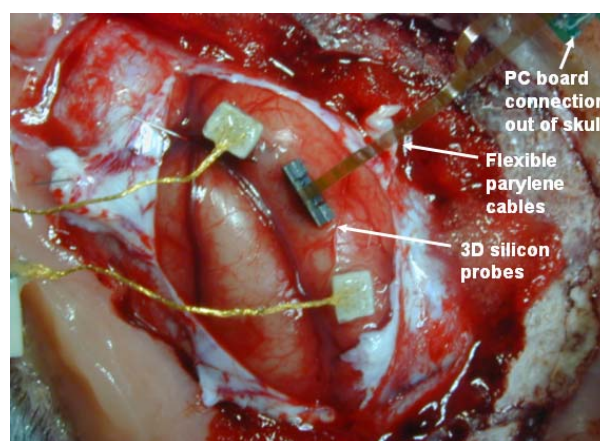
Figure 3-24   Successful chronic implantation in monkey cortex by penetrating pia using a complete device with metal electrodes and flexible parylene cables

3.7.2 Electrode Impedance Test

The electrode impedance is critical in the design of neural probes. The equivalent circuit of a microelectrode is shown in Figure 3-25 [23]. The physical origins of the components are as follows: Z_a is the input impedance of the amplifier, C_s is all the shunt capacitance to ground from the electrode to the input of the amplifier, R_m is the resistance of the metallic portion of the microelectrode, C_e is the capacitance of the electric double layer at the interface of the electrode opening and the electrolyte solution, R_e is the leakage resistance due to charge carriers crossing the electric double layer, R_s is the resistance of the saline bath between the metallic interface of the electrode and infinity (ground electrode) (This is sometimes called the spreading resistance.), and e_n is the potential created in the volume conductor with respect to a point at infinity by the extracellular currents flowing about a neuron during an action potential.
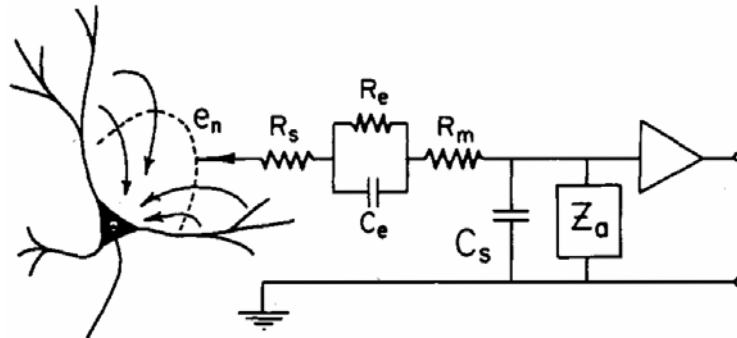
Figure 3-25   The equivalent circuit of a microelectrode

From rough calculation, we can find that the dominant part of the electrode impedance at 1 KHz is C_e, which is the capacitance of the electric double layer. Therefore the electrode impedance is dominated by the size of the electrode opening, as characterized by the electrode impedance dependence on the size of the plasma-etch-opened metal

electrodes. The testing data allow us to determine the optimum material and size of the electrodes for different applications [123].

As shown in Figure 3-26(a), simplified devices with only metal and parylene layers have been fabricated for characterization of the electrode impedance. Two types of metals, gold and platinum, are used for the electrode material. There are 28 electrodes fabricated on one device with the electrode opening area from 25 μm^2 to 3400 μm^2, as shown in Figure 3-26(b). Figure 3-26 (c) shows an SEM picture of one typical electrode.
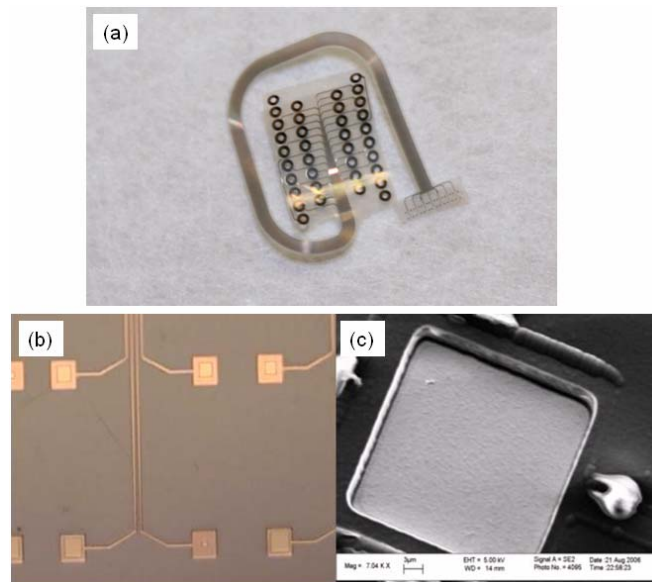
Figure 3-26   (a) Simplified device with only metal and parylene layers for characterization of the electrode impedance; (b) electrodes with different size of opening area; (c) SEM picture of one typical electrode

The fabrication process flow is shown in Figure 3-27: 1) Sacrificial photoresist is spin-coated on silicon. 2) Bottom parylene layer (8 μm) is coated. 3) E-beam evaporates the metal layer (Ti/Pt or Cr/Au with thickness 200 Å / 2000 Å) and patterns it by lift-off process. 4) Top parylene (2 μm) is coated. 5) RIE O_2 plasma etch is used to open the electrode sites

and to outline the structure. 6) Device is released and annealed at 200 ºC in vacuum oven for 48 hours.
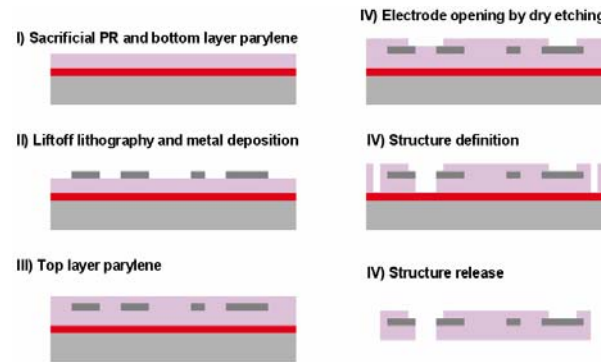
Figure 3-27   Fabrication process flow of the impedance characterization devices

Impedance values are obtained by recording the current while submersing the electrodes in saline solution and passing current through them. The impedance dependence on electrode size at 1 KHz for both gold and platinum metals is measured (Figure 3-28). We found that platinum electrodes have impedance values significantly lower than those of the gold electrodes, thus allowing higher specificity for the same impedance.
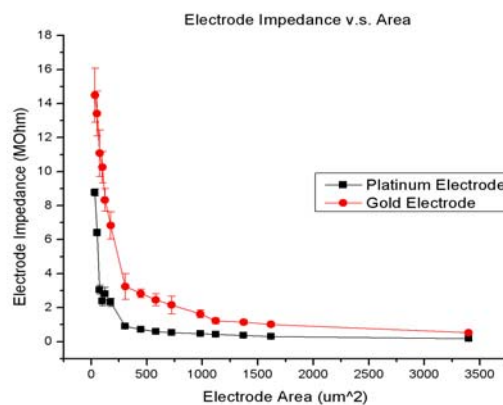
Figure 3-28   Gold and platinum electrode impedance mapping as a function of area at 1 KHz

3.7.3 Electrodes with Electroplated Platinum Black

Ideally, an electrode for sensing neural signals would have low impedance and high specificity with high signal-to-noise ratio (SNR). However, low impedance and high specificity are competing attributes, as low impedances allow the electrode to pick up a larger number of neurons. Also, impedance and area, and thus specificity, are inversely correlated, making it difficult to optimize both SNR and specificity. One solution is to electroplate platinum black on the electrode surface to increase the effective surface areas. Therefore, the electrode impedance can be lowered by orders of magnitude and at the same time have high specificity.
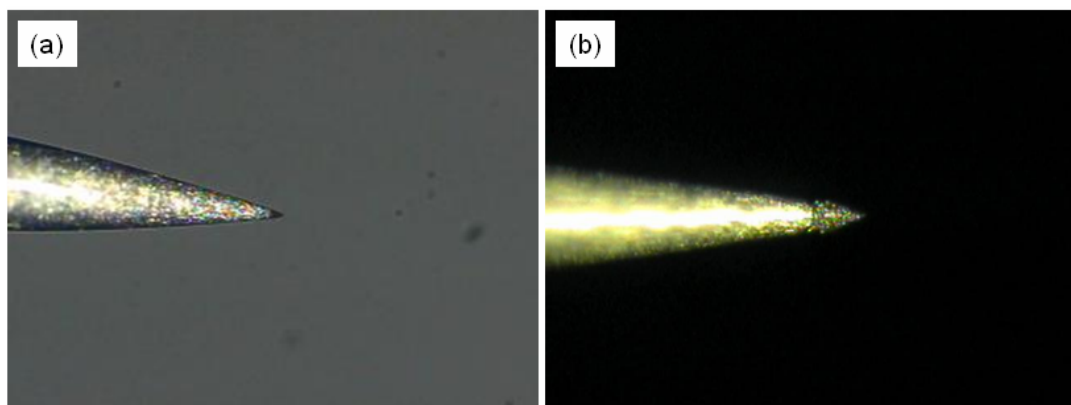
Figure 3-29   (a) The tip of a metal wire electrode without electroplated platinum black; (b) the tip of the same metal wire electrode after platinum back electroplating

Platinum black electro-plating is first performed on a metal wire electrode. Electroplating solution contains 1% chloroplatinic acid (Sigma C-3044), 0.0025% hydrochloric acid, and 0.01% lead acetate in water [124].   Electrodes were plated with 5 V DC through a 10 MΩ resistor for 10 sec. Figure 3-29 shows comparison pictures of the tip of the same metal wire electrode. Figure 3-30 shows the impedance test results of the same

metal wire electrode before and after electroplating with platinum black. The impedance of the metal wire electrode was greatly reduced by electroplating with platinum black. At 1 KHz, the impedance dropped from 24 KΩ to 9.2 KΩ.
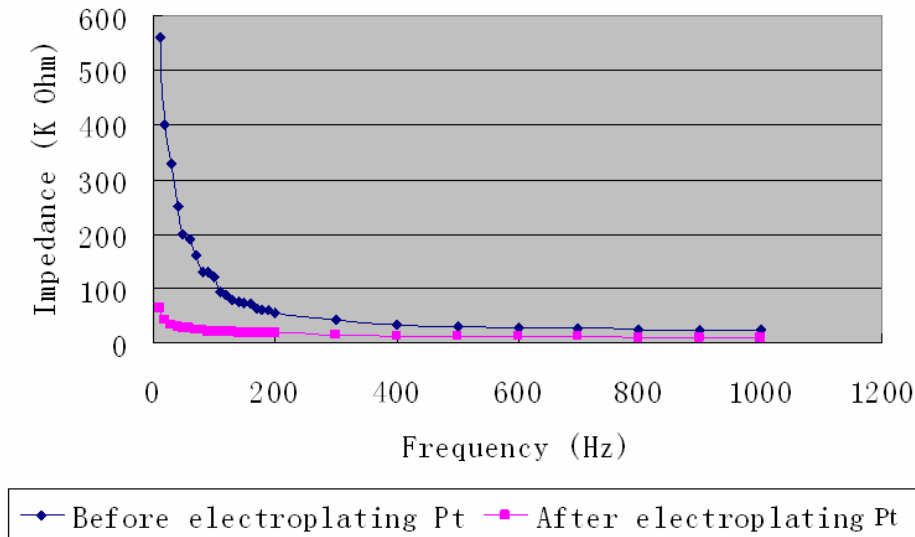
Figure 3-30   Impedance test results of the same metal wire electrode before and after electroplating with platinum black

Figure 3-31 shows SEM pictures of the 5 μm × 5 μm gold electrode of the parylene neural probes after 30 sec of platinum black electroplating using the same solution and setup. Figure 3-32 shows the impedance testing result. At 1 KHz, the impedance dropped from 1.1 MΩ to 9.28 KΩ, by about two orders of magnitude.

From the testing results, we found that electroplating with platinum black greatly reduces electrode impedance by increasing the electrode's effective surface area, while at the same time keeping the electrode size small enough for high-specificity sensing. The impedance drop can be controlled by the concentration of the electroplating solution and the electroplating time. However, black platinum may become loose and may be scraped

off by brain tissue during insertions, which may change the impedance of the electrodes and further contaminate the brain. This is one of the biggest concerns of this application. Further in vivo tests need to be done with platinum-back-electroplated electrodes before the technology is ready for use.
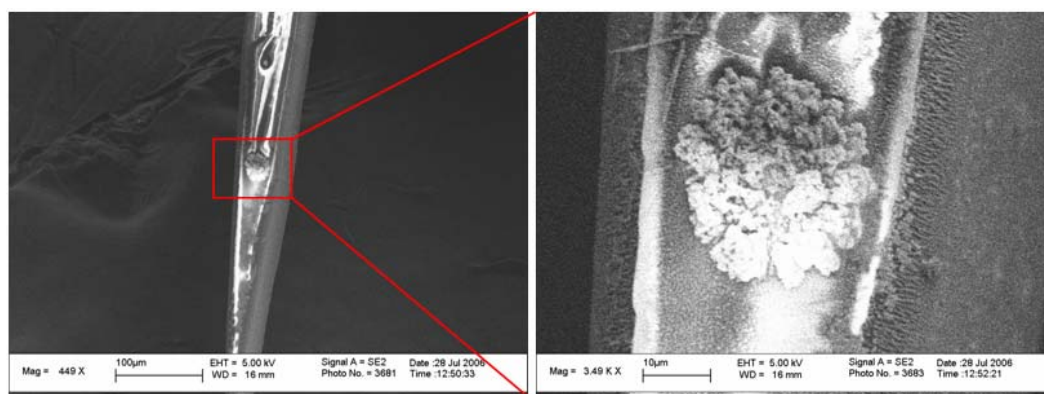
Figure 3-31   SEM pictures of the 5 μm × 5 μm gold electrode of the parylene neural probes after 30 sec of platinum black electroplating
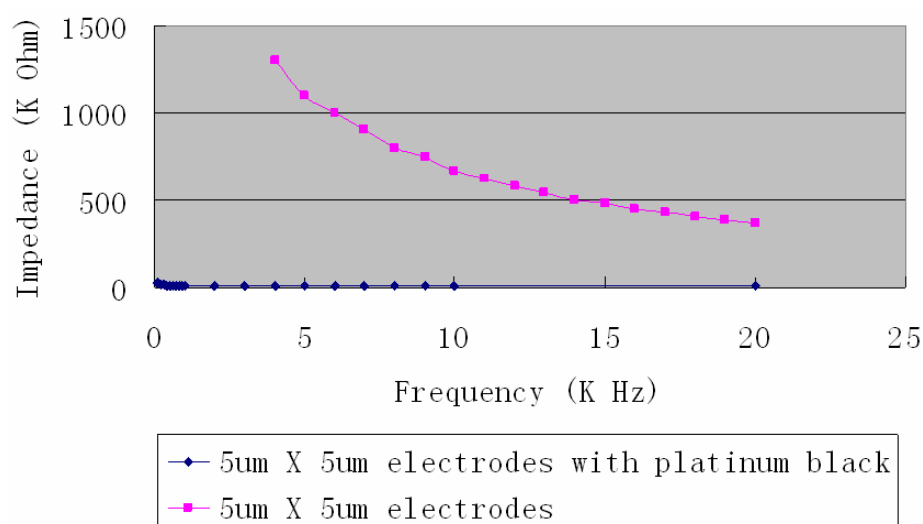
Figure 3-32   Impedance test results of the 5 μm × 5 μm gold electrode of the parylene neural probes before and after electroplating with platinum black

3.8   Summary

With good mechanical, electrical, and biocompatible properties, parylene is an ideal material for the insulating layer of neural probes and for making polymer cables for the high-density 3-D probe arrays used for chronic implantation. Experiments show the good dielectric property of parylene C as an insulating material on probes. An all-dry process was demonstrated to fabricate the new multi-site probe arrays with monolithically integrated parylene cables. PPO (Parylene-PCB-Omnetics connector) high-density packaging technology has been developed to bond the parylene neural probes with commercial connectors. Testing probes were fabricated for probe shank rigidity testing. The in vivo testing results provide reference for optimal geometric design of the probe shanks. The testing results also showed that the parylene layer greatly enhanced the mechanical properties of the probe shanks. Electrode impedance with different materials and different size of open areas was tested using testing devices. Preliminary testing results on electrodes electroplated with platinum black gave one solution for further improving the electrode performance.

CHAPTER 4

96-ELECTRODE CHRONIC

IMPLANTATION SYSTEM

4.1   Introduction

With the advantages of our new techniques, our parylene neural probes have great potential for making very high-density arrays. In this chapter, we will introduce our recent work on the 96-electrode chronic implantation system for monkey and human brains [125]. Improvements of the neural probes have been achieved. For the application to monkey and human brains, extremely long flexible parylene cable has been designed and fabricated. In order to improve the biocompatibility of the probes for chronic implantation, a new process has been developed to completely cover the silicon probe shank with a parylene layer. As we all know, parylene has better biocompatibility than silicon. A new type of 96-channel percutaneous connector has been designed and fabricated. The PPO (Parylene-PCB-Omnetics connector) high-density packaging technology which was

introduced in Chapter 3 is used to package the 3-D parylene probe array of 96 electrodes with the percutaneous connector.

4.2   Parylene Neural Probes with Long Flexible Parylene Cables

4.2.1   Device Design

The layout design of the parylene neural probes with long flexible parylene cables for the 96-electrode chronic implantation system is shown in Figure 4-1. The device includes three parts: the front probe part, the long flexible parylene cable, and the parylene sheet connector for percutaneous connector.

The eight probe shanks are placed in a "V" shape. The two longest shanks in the center are 5.1 mm long. The shanks on the sides are 4.6 mm, 4.1 mm, and 3.6 mm long, respectively. The probe shank base width is 170 μm, and the probe thickness is ~ 150–170 μm. The lateral taper angle of the chisel-shaped tip is 10°.

Four sensing electrode sites are on each shank, therefore 32 sensing electrodes are on each 2-D probe plate, and a 3-D (8×3) probe array with 96 electrodes can be made by stacking three 2-D probe plates. Four types of sensing electrodes are designed with aquare opening areas of 19.75 μm, 23.1 μm, 28.2 μm, and 33 μm. Reference electrodes are placed on the tip of 4.6-mm-long shanks with size of 25 μm $\times$ 1 mm. Platinum is used for the electrode material.

Long flexible parylene cable is designed using stepper mask stitching technology. As shown in Figure 4-1, the cable routes in three combined mask areas result in a cable design about 7 cm long. The number of second mask areas can be easily increased to extend the cable length. For example, a 12-cm-long cable can be made by using four

combined mask areas, and is long enough for chronic implantation in human brains. Parylene cable thickness is 13 μm—6.5 μm each for both the top and bottom parylene layers. The width of the parylene cable is 910 μm, with 34 channels (32 for sensing electrodes and 2 for reference electrodes) packaged inside. Platinum is also used for the trace lines (the same layer as the electrode metal layer). The width of individual trace lines is 10 μm with 10 μm apart. The thickness of the metal trace lines is 0.25 μm.

The parylene sheet connector is for the PPO high-density packaging. A modified design is made for the 96-channel percutaneous connector. One parylene sheet connector includes two parts matching two 18-pin Omnetics connectors with an angle of 60°. Three parylene sheet connectors will match six Omnetics connectors symmetrically distributed on a circular PC board for the 96-electrode system. The symmetric parylene sheet connector design enables the 3 devices for a 96-electrode system to be fabricated by the same mask design.
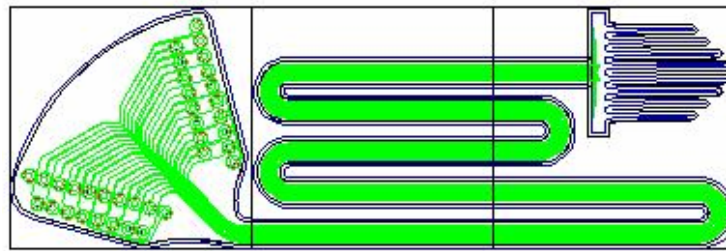
Figure 4-1   Layout design of the parylene neural probes with long flexible parylene cables

4.2.2   Fabrication Process

The fabrication process flow for making the parylene neural probes with long flexible parylene cables is shown in Figure 4-2. The process starts with a

double-side-polished wafer. A 0.5 μm melted parylene C layer is patterned on the probe shanks area to provide adhesion between silicon substrate and the next parylene layer. 1 μm of sacrificial photoresist layer is patterned in the place of the flexible parylene cable and the parylene sheet connector. The first layer of parylene C (6.5 μm) is then deposited, followed by a layer of lift-off electron beam platinum (0.25 μm) to define the trace lines, the electrodes, and connector pads. A second layer of parylene C (6.5um) is then deposited. Electrode sites and the device definition are then opened/etched by a two-step RIE (O_2 Plasma) process. Silicon probe shanks are subsequently etched by DRIE (deep reactive ion etching) from both sides of the wafer. The devices are later released in ST-22, annealed at 200°C in vacuum oven for 48 hours, and re-coated with 1 μm parylene for a total coverage to achieve biocompatibility. Finally, the electrodes are opened up again by RIE O_2 plasma etching.
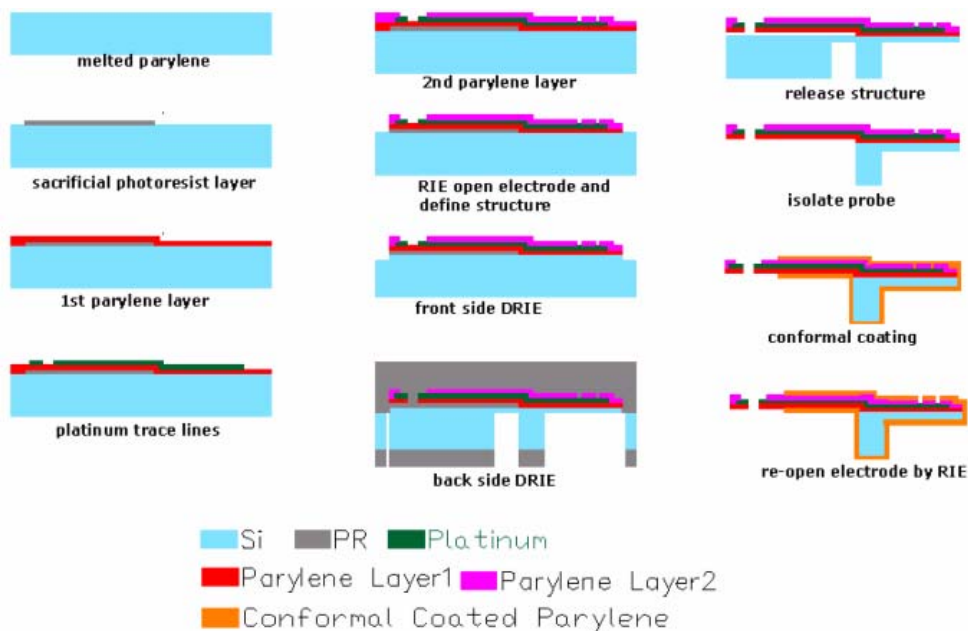
Figure 4-2　Fabrication process flow for the parylene neural probes with long flexible parylene cables

4.2.3 Fabrication Results

Figure 4-3 shows the picture of the 4-inch processing wafer of parylene neural probes with long flexible parylene cables. As we discussed above, the stepper-mask stitching technology is used. As a result, the throughput of the fabrication is relatively low. For the 4-inch wafer process, only 12 devices can be made at a time on one wafer. Fortunately after several runs of process development, the yield rate can reach as high as 90%. Figure 4-4 shows the SEM pictures of the fabricated neural probe shanks. Four types of sensing electrode with different open areas and reference electrodes are shown on the shanks. Figure 4-5 shows released parylene neural probes with 7-cm-long flexible parylene cables. (Because the annealing process has not been performed yet, the parylene cable curves up when it is free standing.)
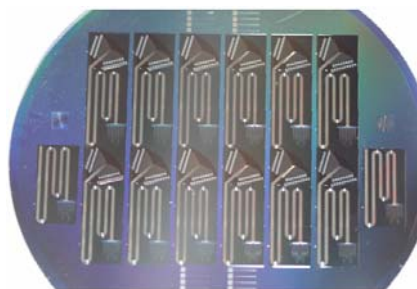
Figure 4-3   Processing wafer of parylene neural probes with long flexible parylene
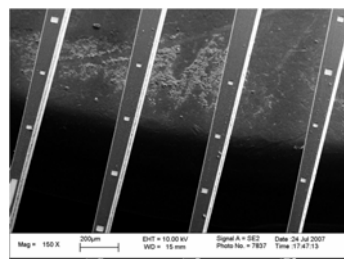
cables

Figure 4-4   SEM pictures of the fabricated neural probe shanks with electrodes
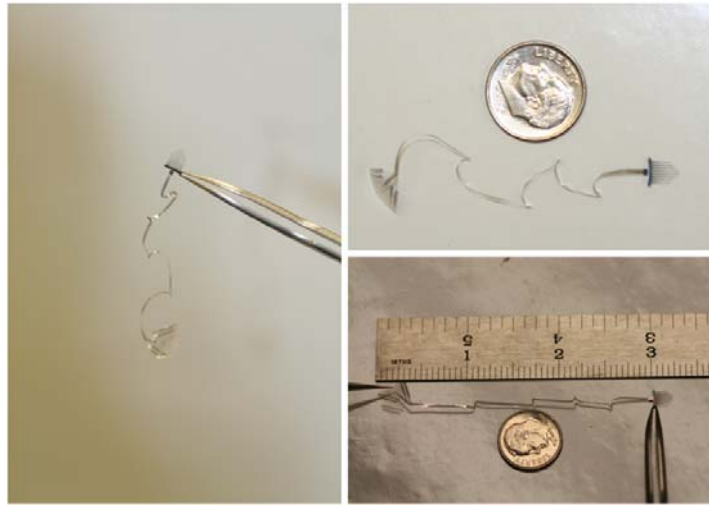
Figure 4-5   Released parylene neural probes with 7-cm-long flexible parylene cables

4.2.4   Process Challenges

4.2.4.1   Parylene-to-silicon Adhesion

As we described in the previous Chapters, XeF_2 etching is used to roughen the silicon surface and increase the mechanical adhesion between silicon substrate and parylene layer. However, the adhesion is not strong enough to survive the saline soaking test. And, as shown in Figure 4-6, the parylene layer had delaminated from the silicon shank after one week's implantation in the monkey brain.
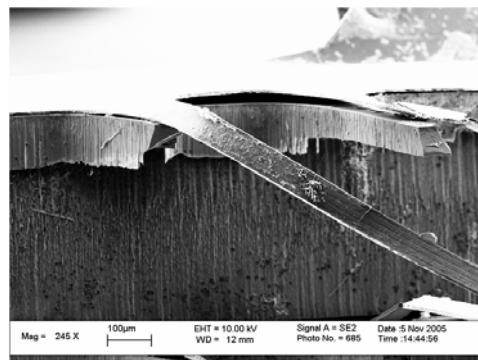
Figure 4-6   SEM picture of a failed device showing the delamination between parylene

layer and silicon substrate after one week's implantation

The melting temperature of parylene C is 290 ^{o}C. Previous work in the Caltech Micromachining Lab shows that after baking at 350 ^{o}C for 2 hours with N_2 flow, the molten parylene layer will glue to the substrate (silicon or glass), providing very strong adhesion. At the same time, the adhesion between the molten parylene layer and the normal parylene layer is also very good because they share the same material structure. In our neural probe fabrication in stead of a XeF_2-roughened silicon surface, 0.5 μm of molten parylene layer is used as an adhesion layer between the silicon substrate and the first parylene layer. Thus the parylene-to-silicon adhesion is greatly improved. Ongoing soaking test results show that the parylene-to-silicon adhesion is able to withstand more than 6 weeks of soaking in 90 °C saline.

4.2.4.2   Lift-off Metal Patterning

Because of very limited routing area on the probe shanks, patterning metal lines with very high resolution is the most pressing technique concern in putting multiple electrodes on a single probe shank. Chemical etching is a commonly used, easy method to pattern metal lines. But isotropic-etching undercut limits the resolution of this method. Figure 4-7 shows the Cr/Au lines coming off the substrate because of wet-etching undercut.

The lift-off process is a good alternate method to pattern metal lines with very high resolution. A photoresist specially developed for lift-off purposes, Lift-Off Resist (LOR), has been developed by Microchem Corp. (Newton, MA, USA), and LOR can be isotropically removed by developer. Figure 4-8 shows the typical lift-off process using LOR. A combination of LOR and normal photoresist, for example AZ 1518, can create a patterned photoresist structure with undercut, as shown in Figure 4-9(a). The undercut

structure provides a very clear edge to the patterned metal lines. Figure 4-9(b) shows the platinum lines patterned by lift-off process on the probe shanks. The highest line resolution achieved is 2.5 μm.
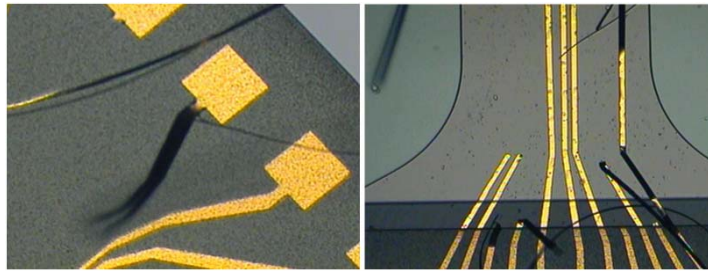
Figure 4-7   Cr/Au metal lines come off the substrate after etching patterning
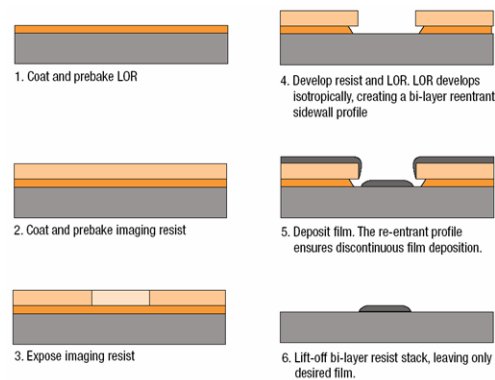
Figure 4-8   Typical lift-off process using LOR
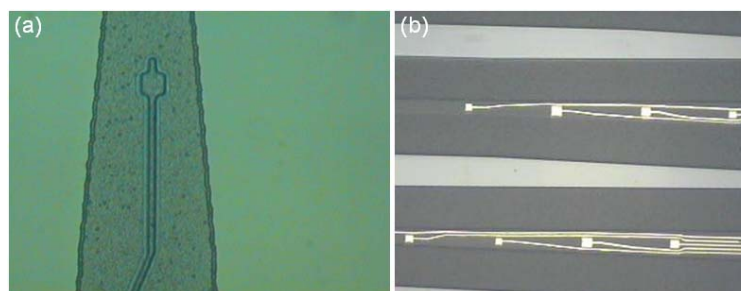
Figure 4-9   (a) Photoresist layer after development, showing undercut for lift-off process;

(b) Pt lines patterned by lift-off process with 5-μm resolution

4.2.4.3 Parylene Cracking
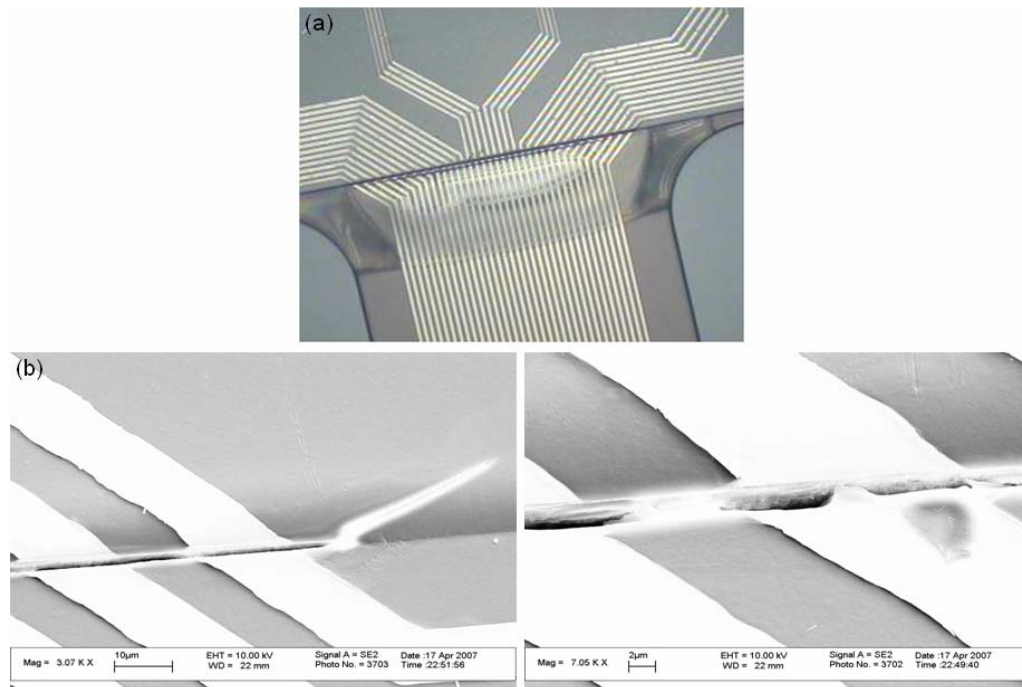
Figure 4-10   (a) Parylene cracks at the sacrificial photoresist step after platinum deposition (The sacrificial photoresist was attacked by solvent because of the crack in the parylene layer); (b) SEM pictures of the parylene cracks at the sacrificial photoresist step after platinum deposition

As determined by previous impedance testing, platinum electrodes have lower impedance than gold electrodes. Since platinum is also more chemically inert than gold, it makes a better material for the electrodes. For many types of neural probe, gold is still used for the trace lines of the electrodes, because of its easier process. For the sake of efficiency, our neural probes use one combined platinum layer for both electrodes and trace lines. But platinum has a higher deposition temperature than gold, creating a tighter thermal budget. Figure 4-10 shows the parylene cracks at the sacrificial photoresist step after platinum deposition because of thermal stress. The sacrificial photoresist was then attacked by

solvent because of the cracks in the parylene layer. To solve this problem, we had to adjust the thickness of the sacrificial photoresist and reduce the platinum deposition rate in order to reduce the thermal effect on the parylene layer.

4.2.4.4 Thick Photoresist for Plasma Etching

To be able to sustain soaking and lifetime testing, thick parylene layers are needed for the flexible parylene cable. The total parylene thickness of our neural probes is about 13 μm, including both parylene layers, which results in a long etching time. We use photoresist as a mask when etching parylene using RIE O_2 plasma etching; the etching rate of parylene and photoresist in RIE is roughly 1:1. The same photoresist mask is also needed for front DRIE etching of about 150 μm silicon. And the photoresist on the probe tip dissolves faster than the photoresist on larger features during the development and etching processes. Thick photoresist (> 20 μm) with high resolution is needed. AZ 9260 thick-film photoresist is designed for the more-demanding higher-resolution thick-resist requirements. It provides high resolution with superior aspect ratios, as well as wide focus and exposure latitude and good sidewall profiles. A process of two spinning coats using AZ 9260 has been developed to make a high-resolution thick photoresist mask of about 30 μm. Figure 4-11 shows the thick photoresist on the probe tip to guarantee a sharp tip after plasma etching. The photoresist is hard baked in oven at 120 $^{\circ}$C for 30 min; the thick photoresist needs to be carefully handled during baking to avoid thermal cracking.
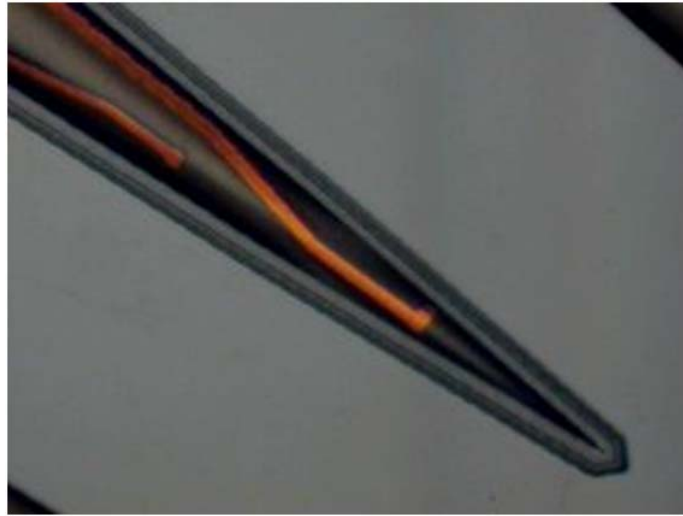
Figure 4-11   Thick photoresist with high resolution on the probe tip

4.2.4.5   Parylene-to-parylene Adhesion

The parylene-to-parylene adhesion is very important to the reliability of the neural probes and the flexible parylene cables. An annealing process has been developed in the Caltech Micromachining Lab to bond two parylene layers together by putting devices in a vacuum oven with N_2 at 200 ^{o}C for 48 hours. Ongoing soaking test results show that the parylene-to-parylene adhesion of the able is able to withstand more than 2 weeks of soaking in 90 °C saline. The annealing process also provides also a good chance to shape the flexible parylene cables. Because the parylene flexible cable is circularly routed to save wafer area, the free-standing parylene cable is curled up; which causes handling and bonding difficulties. A mechanical jig is made to hold the parylene cables straight during annealing. As shown in Figure 4-12, the straight parylene cables have been made by the annealing process.
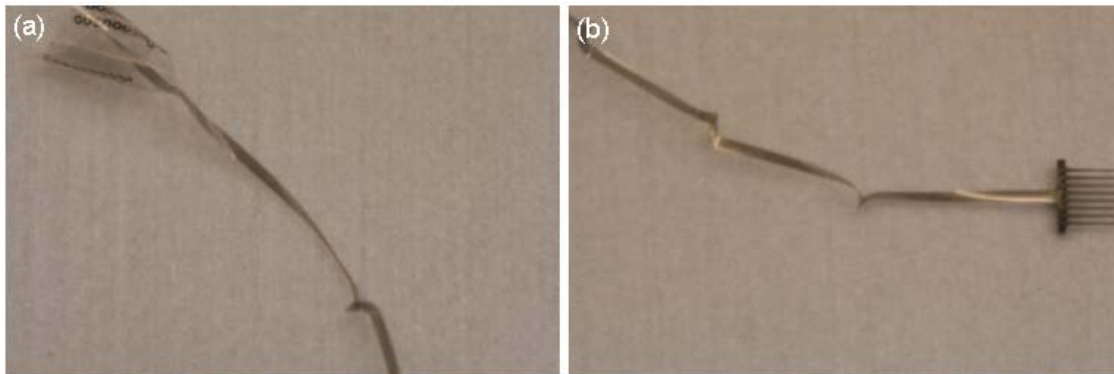
Figure 4-12   Straight flexible parylene cables made by annealing process

4.2.4.6   Completely Parylene Coating on Silicon Shanks

As is common knowledge, silicon is slowly attacked in saline. Although silicon neural probes have been widely used, silicon is not an ideal biocompatible material. We have developed a process to completely coat the silicon shanks with parylene, providing a complete insulation of silicon material from the brain tissue. (Other techniques are also available to realize the same complete-coating process, for example, using lasers to open the electrodes. However, because this is a nonstandard process with very low productivity, it is not feasible for our application.)

First, we developed a tape-detach process to realize the complete parylene coating. Clean room black tape is attached on the top of the neural probe shanks to protect the electrode openings. A 0.4 μm parylene layer is then uniformly coated on the silicon shank's back and sides. The probes are released by detaching the probe shanks from the black tape. Figure 4-13 shows the probe's shank completely coated by parylene using the tape-detach process. As shown in the picture, the side wall of the probe shank is coated with the 0.4 μm parylene layer, which connects with the top parylene layer on the probe

shank. The broken lines of the 0.4 μm parylene layer are on the edges of the top parylene layer, as shown in Figure 4-13. However, the force required to detach the probes will break the thin probe shanks, thus the tape-detach process is only good for very strong probe shanks.
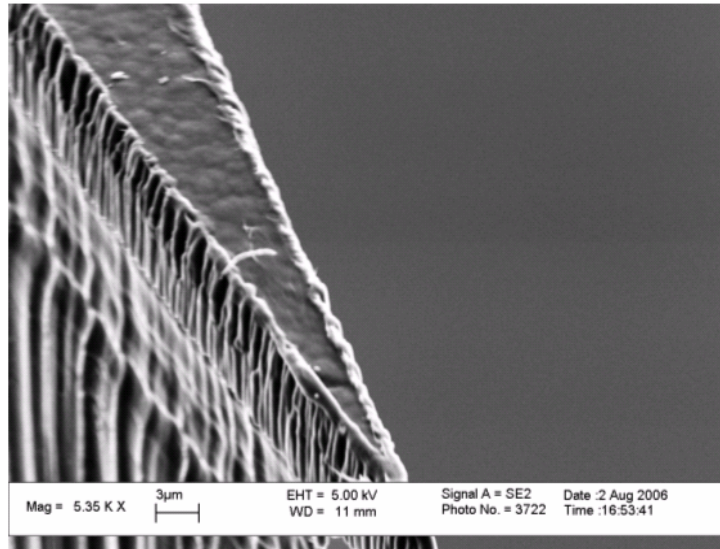
Figure 4-13   The neural probe's shank completely coated with parylene using the tape-detach process

Another, easier and more reliable, RIE etch-back process has been developed for complete parylene coating. After the standard process of probe fabrication described above, the probe shanks and flexible parylene cable are completely and uniformly coated with a 1 μm parylene layer; only the parylene sheet connector is protected by a drop of photoresist. Then photoresist is painted onto both sides of the parylene cable and hardened by oven baking. RIE O_2 plasma etching from the top of the probe shanks is used to reopen the electrodes. Figure 4-14(a) shows the reopened electrode, and Figure 4-14(b) shows that while the parylene layer was etched from the side in RIE, enough

parylene thickness still remains on the sides of the silicon shanks. The completeness of the parylene coating is proved by immersing the coated probe shanks in silicon etchant. The silicon shanks were not attacked by the etchant because they were protected completely by parylene. Another benefit the RIE etch-back process provides is an additional complete coat of parylene around the flexible parylene cable at the same time, further improving the reliability of the cable.
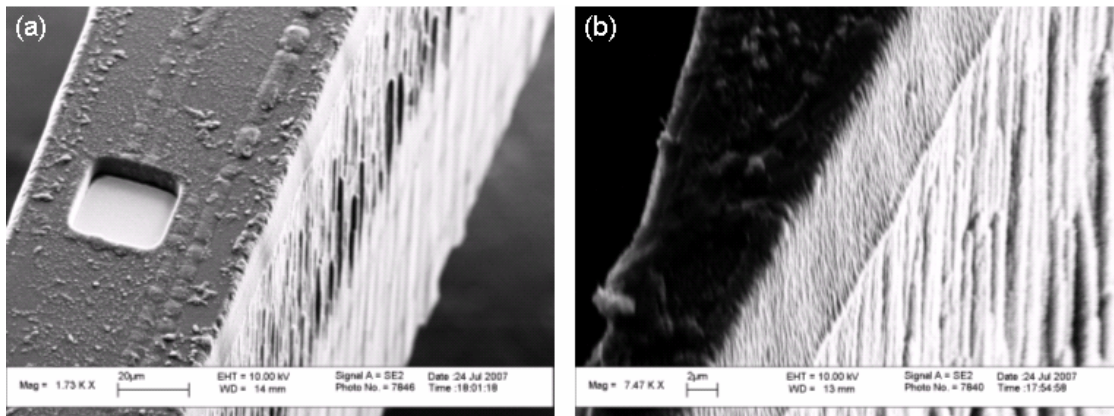
Figure 4-14   Neural probe shanks completely coated with parylene using the RIE

etch-back process: (a) reopened electrode after RIE etching; (b) side wall of the probe

shank coated by parylene layer

4.3   96-Channel Percutaneous Connector

A need exists for a reliable and effective high-contact-density percutaneous connector system for transferring multichannel signals through the skull and skin during chronic implantation. This system will initially be used in animal experiments (e.g., monkey) related to the development of neural prostheses, but the ultimate goal is to develop a new percutaneous connector system that can be utilized in neural prostheses

which are implanted in humans. Such a percutaneous connector system should permit direct connections between signal processors located outside the body and an electrode array implanted in the human brain.

The percutaneous connector system will consist of a pedestal firmly attached to the skull and a replaceable electrical connector with at least 96 separate contacts. The system must have a low physical profile and be made of durable materials to reduce the possibility of it being mechanically damaged during the activities of everyday living. It must utilize biocompatible materials in the parts that directly contact tissue, and it must be designed to minimize the likelihood of infection and chronic drainage due to invasion of microorganisms and/or a poor seal between the device and the skin.

Figure 4-15 shows one commercially available 96-channel percutaneous connector, including both pedestal and headstage connector [126]. This percutaneous connector is specially designed for a Utah array, which has a limitation on probe length (1.0 or 1.5 mm). 96 insulated 1.0-mil Au/Pd wires are used to bond the 96 electrodes, and the stiffness of this bundle of metal wires makes it impractical for chronic implantation in the human brain.
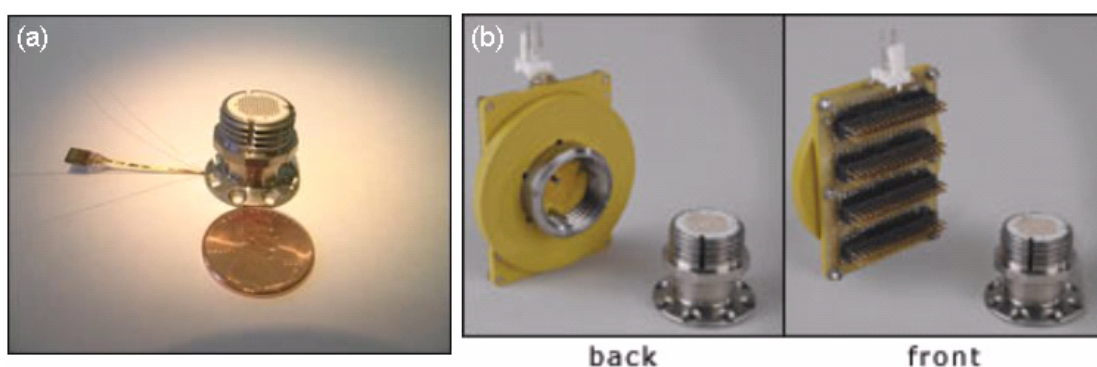
Figure 4-15   (a) Cyberkinetics percutaneous connector for a 96-electrode chronic microelectrode array; (b) the pedestal with headstage connector [126]

A new type of percutaneous connector is designed for our 96-electrode chronic implantation system. Figure 4-16 shows the schematic of this percutaneous connector. The pedestal is made of titanium for long-term implantation. The low-profile design allows for protection from damage during and after experimental recordings. The pedestal is attached to the human skull using titanium screws. A protective cap provides protection and prevents body fluids from entering the connector. PPO (Parylene-PCB-Omnetics connector) high-density packaging technology is used to connect parylene neural probes with Omnetics connectors. A circular PCB with six 18-pin Omnetics connectors symmetrically distributed is screwed into the pedestal and then potted with medical grade silicone elastomer. Flexible parylene cables exit from one side of the pedestal, go through the surgery hole in the skull and connect with the implanted parylene neural probe array. A 3-D drawing of the design of the 96-channel percutaneous connector is shown in Figure 4-17(a). The fabricated 96-channel percutaneous connector is shown in Figure 4-17(b).
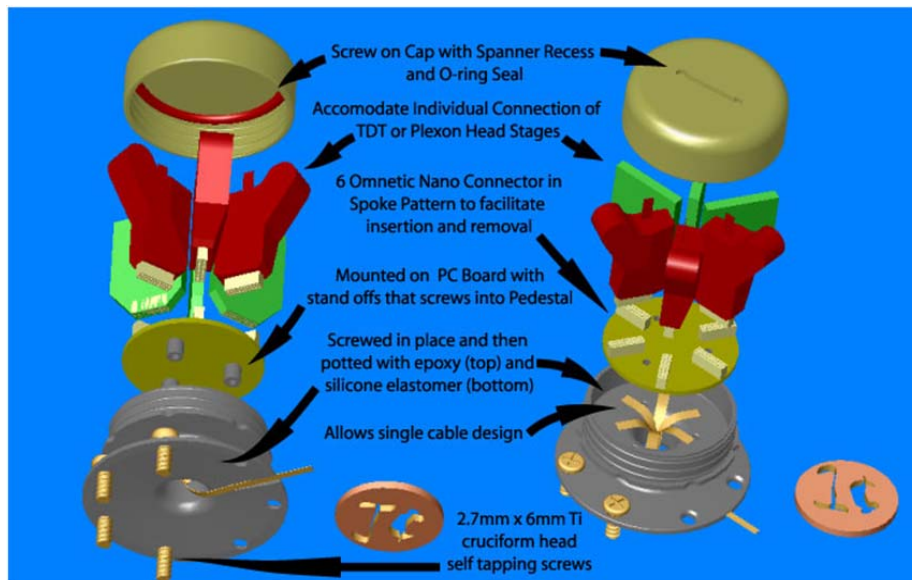
Figure 4-16   Schematic of the design for the 96-channel percutaneous connector

(Pictures courtesy of Dr. Jeremy Emken)
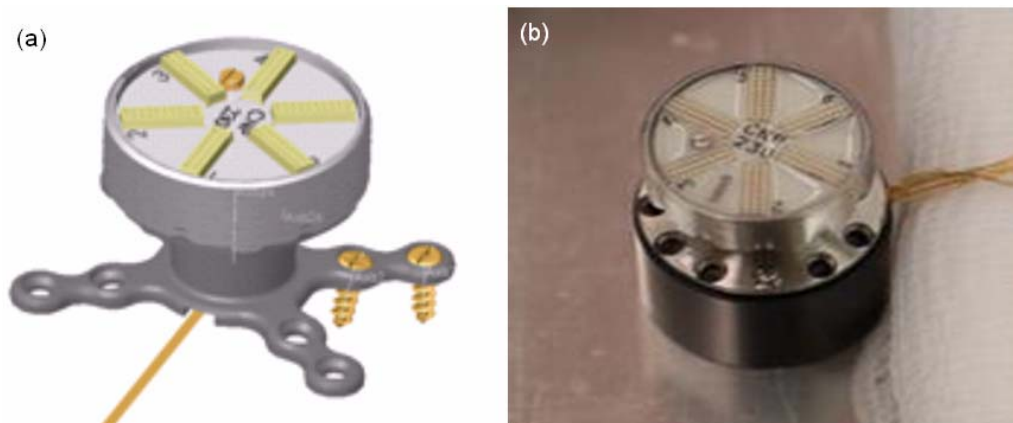
Figure 4-17   (a) 3-D drawing of the design of the 96-channel percutaneous connector; (b)

picture of the fabricated 96 channels percutaneous connector (Pictures courtesy of Dr.

Jeremy Emken)

4.4   Packaging

A PPO (parylene-PCB-Omnetics connector) high-density packaging is designed for

the 96-channel chronic implantation system.

Figure 4-18   (a) PCB and Omnetics connectors for the 96-electrode chronic implantation

system before assembling; (b) assembled PCB and Omnetics connectors; (c) back-side

view of the PCB after conductive epoxy bonding

As shown in Figure 4-18(a), a circular PCB is designed to assemble with six 18-pin

Omnetics connectors. The Omnetics connectors are symmetrically distributed on the PCB

with a 60° separation angle. Figure 4-18(b) shows the PCB assembled with the Omnetics

connectors. The parylene sheet connector of the neural probe devices is then assembled on the PCB along the pins of the Omnetics connectors. Conductive epoxy is painted on to make connection between the bonding metal pad of the parylene sheet connector and each individual pin of the Omnetics connector. Figure 4-18(c) shows the back-side view of the PCB after bonding. Figure 4-19(a) shows one bonded parylene neural probe device (32 electrodes) with a 7-cm-long flexible parylene cable. As shown in Figure 4-19(b), three identical devices are bonded for a 96-electrode system. A 3-D electrode array is made by epoxy bonding three 2-D electrode arrays together (Figure 4-20(c)). Figure 4-20(a) and Figure 4-20(b) show the complete 96-electrode system which includes the 3-D electrode array and the percutaneous connector. As shown in Figure 4-20 (b), the parylene flexible cables go out of the percutaneous connector from one side of the connector, and the outside length is about 4 cm, which is long enough for going through the human skull.
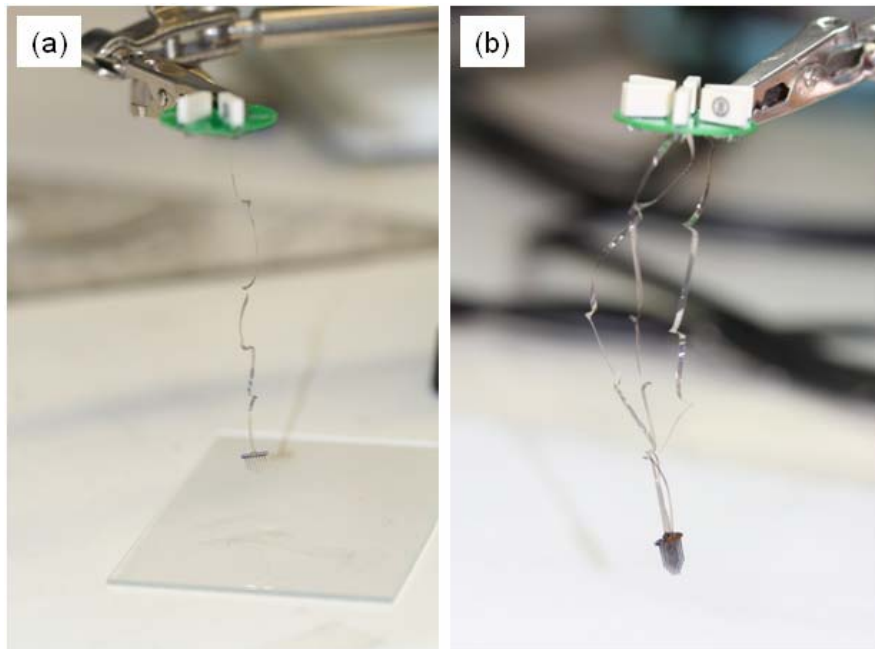
Figure 4-19   Bonded device on PCB and Omnetics connectors: (a) 32 electrodes; (b) 96 electrodes
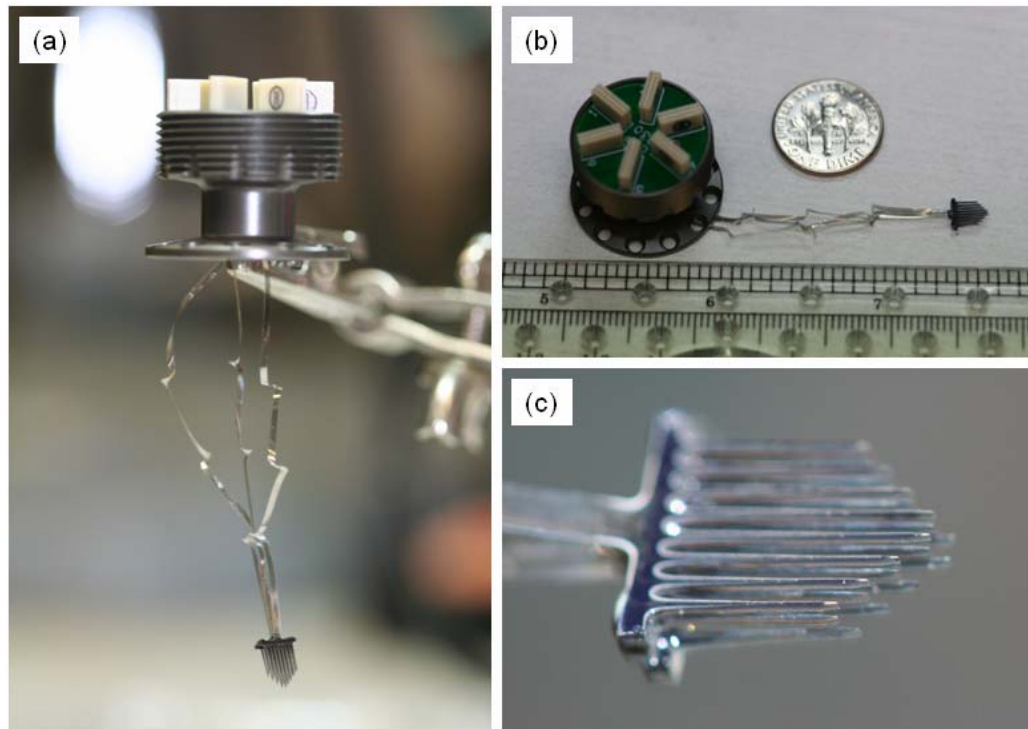
Figure 4-20   (a) (b) The 96-electrode system for chronic implantation; (c) 3-D parylene

neural probes (8 × 3) with 96 electrodes

4.5   Testing Results

The electrodes are subjected to a saline in vitro impedance test. The impedance of

the 23.1 μm × 23.1 μm electrodes is 670 KΩ ± 33 KΩ at 1 KHz, and that of the reference

electrodes is about 20 KΩ. Different signal types, including sine waves and replicated

action potentials, were pumped into the saline and were successfully recorded with the

fabricated electrodes (Figure 4-21).

The devices were inserted through the pia and cortex of live rats to test their

penetration ability. Results show a full insertion of the probe was successful without any

bending, buckling, or breakage. Finally, the devices underwent accelerated life testing to

determine the mean time to failure. Failure modes include the silicon-to-parylene adhesion, as well as de-lamination between the parylene layers. Ongoing soaking test results show that the parylene-silicon adhesion is able to withstand more than 6 weeks of soaking in 90 °C saline, and that parylene cable quality is uncompromised after 2 weeks of soaking in the same environment.
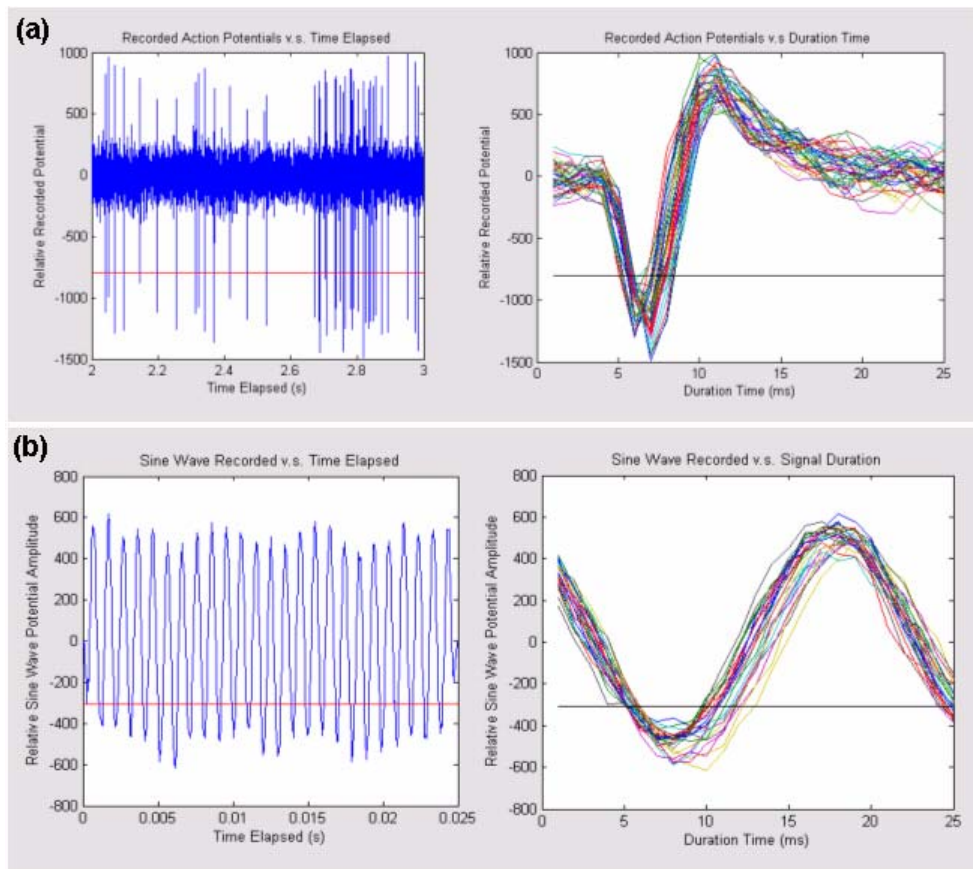
Figure 4-21   Signal recorded by the electrode of parylene neural probes: (a) action potential recorded; (b) sine wave recorded

4.6   Summary and Future Work

A 96-electrode parylene neural probe chronic implantation system has been designed, fabricated, and characterized. A 7-cm-long flexible parylene cable has been

monolithically integrated with the neural probes. A novel RIE etch-back process has been developed to completely coat the silicon probe shanks with parylene giving the neural probes better biocompatibility. A molten parylene layer was used to improve the adhesion between parylene layer and silicon substrate. A 96-channel percutaneous connector has been designed and fabricated. The neural probes were bonded with the percutaneous connector using the PPO (Parylene-PCB-Omnetics connector) high-density technology. Different types of signals were successfully picked up by the electrodes in an in vitro test. Ongoing soaking tests show good parylene-to-silicon and parylene-to-parylene adhesion.

Future work includes in vivo acute testing and chronic implantation. We plan to implant this system in a rat for 3 months and conduct a histology study from the surgery. A reversed version of the 96-electrode system will be implanted in a monkey or human brain for chronic testing.

Our next generation of neural probe system will include wireless communication. As shown in Figure 4-22(a), the completely packaged system will include battery, signal amplifier, data storage and processing, and wireless communication. The schematic of PCB design for the system is shown in Figure 4-22(b).

With the advantages of parylene packaging technology, we also propose a size-minimized implantable capsule for an under-skin neural probe wireless implantation system, which includes a two-way RF coil for transferring power and data, low-power IC chips (with battery management, data processing, and telemetry), an implantable battery, and a discrete biomedical-grade capacitor for recharging if necessary.

(a)

Embedded Signal Cables

Protective Cover

Battery Pack

Microprocessor and Signal Processing

Protective cover

Prototype Semi-chronic Microdrive

Acrylic
Cranium
Dura
Brain

(b)

Flexible Cable

Future PC Board

Bus Interface

AMP

ADC

On Chip AMP/MUX

Probes Array

EPROM

DSP

Wireless Interface

Computer Data Acquisition

Power Interface

Power Management
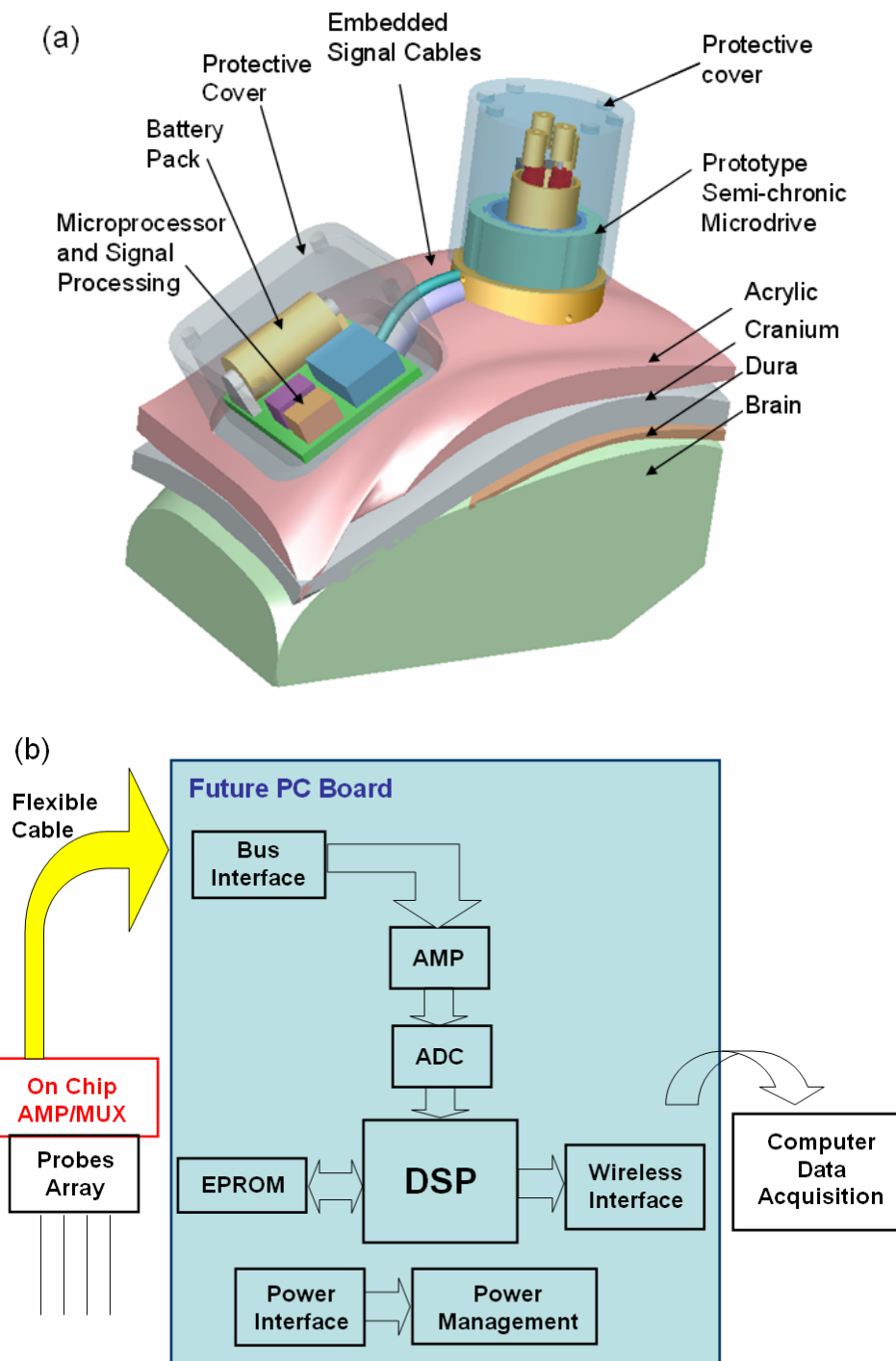
Figure 4-22   (a) Illustration of a packaged neural probe implantation system with

wireless communication; (b) schematic of PCB design for the system

CHAPTER 5

ELECTROLYSIS ACTUATORS FOR MOVABLE NEURAL PROBES

5.1   Introduction

One of the biggest limitations in current multi-electrode technologies and practice is the lack of movable ability; the electrodes in fixed-geometry arrays cannot be adjusted once they are implanted. Since the arrays cannot be positioned precisely at the level of single neurons during implantation, the yield and quality of the recorded signals often depend upon the luck of the initial surgical placement. The array's useful signal yield may be low, as the electrodes' active recording sites may lie in electrically inactive tissue, be distant from cell bodies (which generally produce the largest extracellular signals), or sample cells with non-optimal receptive fields for the experiment at hand. Even if the initial placement is satisfactory, fixed-geometry arrays can drift slightly in the brain matrix due to tissue movement caused by respiratory or circulatory pressure variations [127], and mechanical

shocks due to movements of the animal subject [128]. This drift can lead to the separation of the electrode from the vicinity of active cells, thereby lowering signal yield. Some fixed arrays are fabricated with lower impedance electrodes to make up for their lack of adjustment by increasing the "listening" volume. Unfortunately, recordings from low-impedance electrodes can suffer poorer signal quality and signal discrimination.

Clearly, the possibility of repositioning electrodes after implantation would significantly improve the quality and yield of neural recordings. Figure 5-1 shows the importance of the distance between the sensing electrode and the neuron to the quality of the extracellular neural signal. In contrast to fixed-electrode arrays, autonomously movable electrode arrays should also increase the yield and lifetime of implanted systems by enabling signal yield from more channels, maintaining higher quality signals for longer periods of time, and allowing the electrode tips to advance to new cells upon loss of signal.
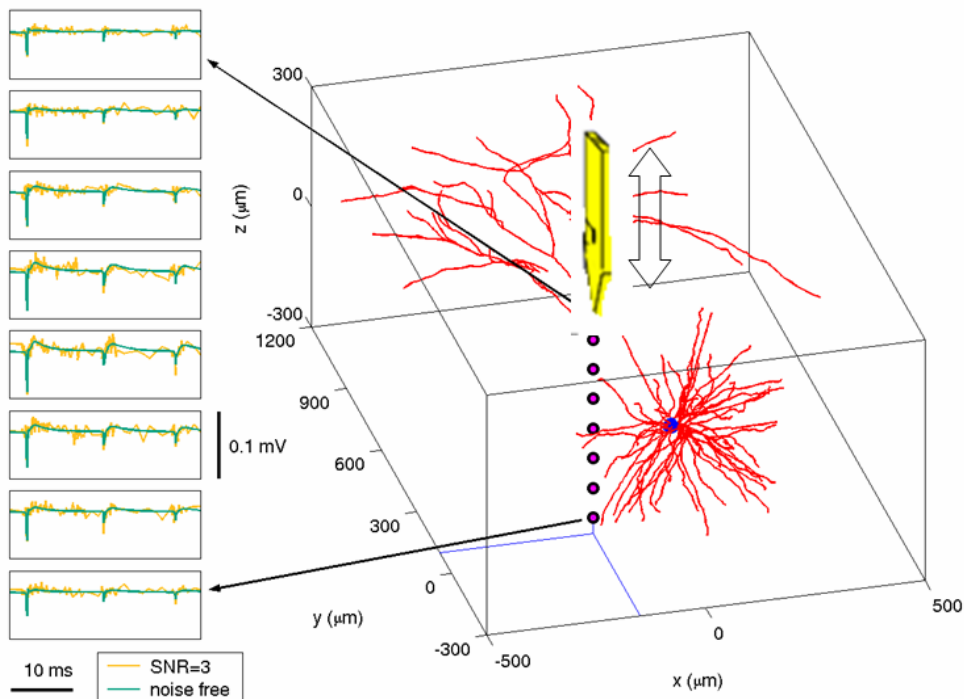
Figure 5-1   Extracellular field simulator

However, for brain use, the movable neural probes need to be powerful (to penetrate brain tissue), high density, low power, bidirectional, and latchable (without power). We have since proposed to develop electrolysis-based actuators for the movable probes. Our initial work presents novel miniaturized MEMS actuators that can drive movable electrodes to adjust their position so as to optimize and maintain the quality of the recorded signal. For chronic experiments or neuroprosthetic applications, the MEMS movable probes will provide a unique and useful capability for post-implantation electrode adjustment that will improve the quality and yield of the recorded signals, and possibly increase the longevity of the implant.

5.1.1   Review of Movable Neural Probes and Current Challenges

Variations of chronic microdrives, in which manual turning of lead screws advances individual or small bundles of electrodes, provide the ability to reposition electrodes so as to re-optimize signals during long-term recordings [13, 129-134].   Large arrays of movable electrodes (49 [135] and 144 [11], respectively) for chronic implantation, in which a conventional microdrive is manually used to push or pull each electrode, have also been reported. Again, a great deal of manual operation is required to reposition each electrode in these devices.

Different types of minimotors have been developed and used to drive movable electrodes. Eckhorn developed a "rubber tube driving principle [136, 137]," which uses the tension of a rubber tube to push the metal electrode to move into a position controlled by a gear motor. But the large size of the system limits its use for chromic implantation.

Fee described a motorized chronic microdrive with three movable electrodes [138] that is suitable for freely behaving small animals such as the zebra finch. This device,

which uses three miniature electric motors, was still operated under human control. Fee reported that the ability to easily adjust the electrodes led to significant improvements in experimental productivity.

Recently, Professor Joel Burdick's lab at Caltech has developed a movable probe system for chronic implantation (Figure 5-2(a)) [139-141], which includes four glass-coated Pt-Ir electrodes driven individually by piezoelectric linear actuators. A control algorithm has also been developed for autonomously isolating and maintaining optimal extracellular action potentials [142, 143]. Figure 5-2(b) shows the neural signal stream detected by the movable neural probe and used to isolate neuron cell in a monkey cortex. This insight is promising for the activities that go beyond manual electrode adjustment to automated adjustment of multiple electrodes.
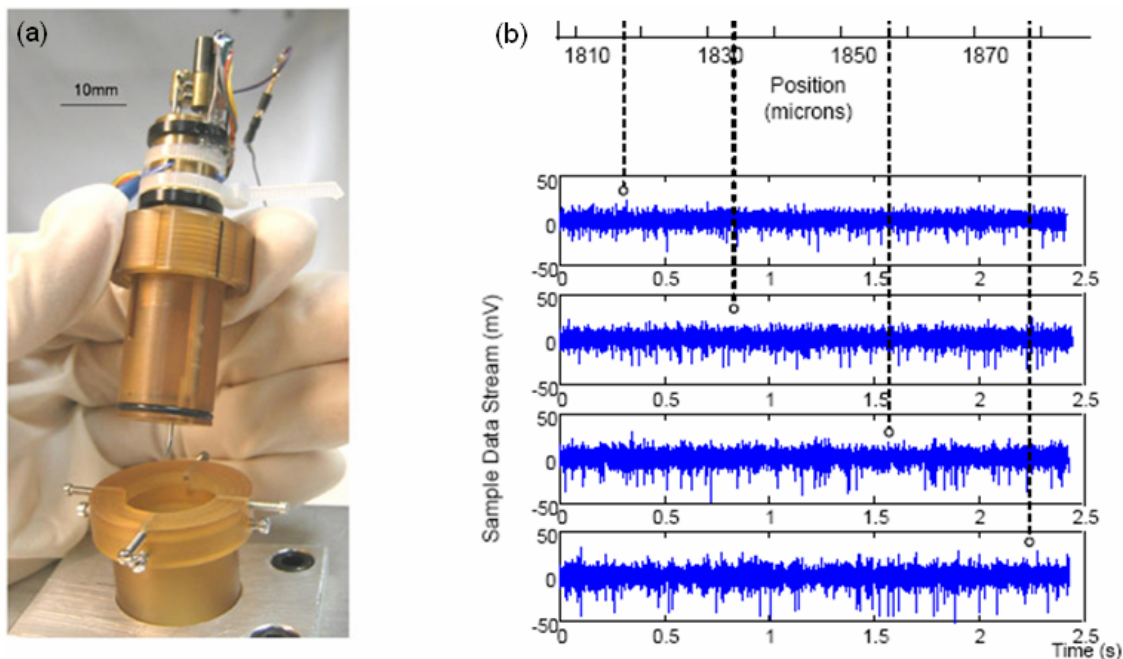
Figure 5-2   (a) Movable probe system with four metal wire electrodes driven by piezoelectric linear actuators; (b) neural signal stream detected by the movable neural probe and used to isolate neuron cell in a monkey cortex [139]

In summary, for chronic recording, it is difficult to reliably obtain stable and selective signals with very high yield from fixed-geometry implanted arrays over long periods of time. While current chronic microdrives have proven useful for basic-science research, they are not suited for neuroprosthetic systems. Current chronic micro-drive systems, which require manual manipulation, cannot easily optimize the isolation of neurons, and cannot ensure that specific neurons or neural populations are selected. Moreover, the geometries of their superstructures are unsuitable for future neuroprosthetic applications in humans. The size of the motorized microdrives limits their use for large electrode arrays.

For human brain use, the actuators for the movable neural probes need to meet several requirements: low voltage actuation, low heat dissipation, low power drain, high force generation capability and large displacement, lockable and reversible ability, small size, and easy integration with high-density electrode arrays. MEMS technology provides great opportunities to fabricate micro actuators to meet all the requirements. Unfortunately, many MEMS actuator technologies are not suitable for chronically implantable movable probes. Table 5-1 summarizes some of the relevant properties of MEMS actuators that have been developed to date, as well as the electrolysis actuator we propose to develop. Electrostatic actuators [144-146] and piezoelectric [147, 148] actuators often require high voltage (> 100 V). Not only do high voltages interfere with neural recording, voltage leaks in the case of component failure may damage neural tissue. Some actuator types also suffer from low arrayability (the ability of the actuators to be formed into arrays due to form factor limitations and other engineering issues). Thermo-pneumatic actuators [149, 150] cause excessively high temperature rises, which can cause tissue damage and loss of brain function in the probe's vicinity. Similarly, the most miniaturized electromagnetic motors, such as

MicroMo's (1.9 mm O.D.) motors, require hundreds of mW of power, a delicate gearbox for operation, and are too large for formation into arrays. Generally, most MEMS actuation techniques, such as shape memory alloy actuators [151-153], are not "lockable"—they require continual application of energy to maintain their position, which can cause unacceptable tissue heating. In summary, most commonly investigated MEMS actuation techniques suffer from one or more drawbacks for our needs.

Table 5-1   Relevant properties of MEMS actuators

Actuation Type	Power Supply	Heat Dissipation	Output	Lockable	Arrayable
Electrolysis actuator	**Low current & voltage**	**Low**	**Large force & displacement**	**Yes**	**High**
Shape-memory alloy	High current & power	High	Large force & displacement	No	Low
Piezoelectrics	High voltage	Medium	Large force, small displacement	No	Low
Electromagnetics	High current	High	Medium force	No	Poor
Electrostatics	High voltage	Low	Small force & displacement	No	High
Thermoelastic	High current & power	High	Large force, small displacement	No	Medium
Electroosmotics	High voltage	Medium	Large force, small displacement	No	Low
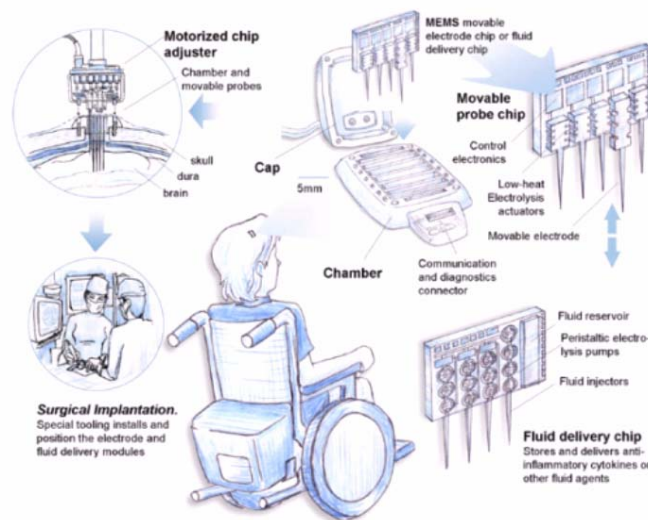
Figure 5-3   Proposed movable neural probe array with electrolysis actuators for neuroprosthetic applications in humans

Our previous research shows that the electrolysis-based MEMS actuators overcome many of the problems of known actuation techniques. As a whole, except for electrolysis-based actuators, none of the other actuator technologies are currently feasible for our use. The electrolysis-based actuator needs low current ($\sim$ μA) and voltage ($<$ 5V), but will output large force and large displacement. It operates at room temperature and has latching capability. Figure 5-3 shows our proposed movable neural probe array with electrolysis actuators for neuroprosthetic applications in humans.

5.1.2 Electrolysis Technology

5.1.2.1 Theory

Electrolysis is proposed to actuate the probes of an implantable movable electrode array. Electrolysis is a technique for converting electrical energy to pneumatic energy. The two electrochemical half-reactions for the electrolysis of water are shown in Eqs. 5-1 and 5-2. The net reaction (Eq. 5-3) entails a 3:2 stoichiometric ratio of gas to liquid and occurs via the transfer of four equivalents of electrons through an external circuit.

$$2H_2O(l) \underset{recombination}{\overset{electrolysis}{\rightleftharpoons}} O_2(g) + 4H^+(aq) + 4e^- \qquad [5\text{-}1]$$

$$4H^+(aq) + 4e^- \underset{recombination}{\overset{electrolysis}{\rightleftharpoons}} H_2(g) \qquad [5\text{-}2]$$

$$\text{Net: } 2H_2O(l) \underset{recombination}{\overset{electrolysis}{\rightleftharpoons}} O_2(g) + 2H_2(g) \qquad [5\text{-}3]$$
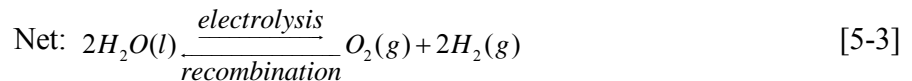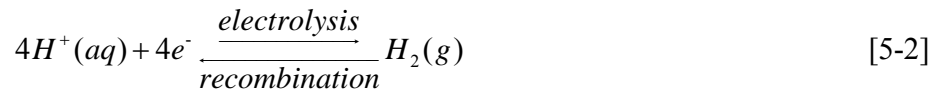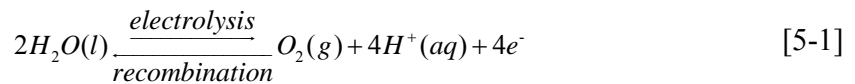
Since an actuator device based on these reactions is powered by the gas it generates, its response will be governed approximately by the ideal gas law:

$$PV = nRT \qquad [5\text{-}4]$$

The maximum fractional change in length $\Delta L / L$, or strain, can be calculated by the volume change at constant pressure,

$$V_{gas} = (3/2)n_{H_2O}RT / P \qquad\qquad [5\text{-}5]$$

$$V_{liquid} = n_{H_2O} \times M_{H_2O} / \rho_{H_2O} \qquad\qquad [5\text{-}6]$$

where M_{H_2O} and ρ_{H_2O} are the molecular weight and density of water, respectively, and n_{H_2O} is moles of water transformed. The maximum relative strain under ambient conditions can be calculated:

$$strain = \frac{(actuated \quad length) - (unactuated \quad length)}{unactuated \quad length} \qquad\qquad [5\text{-}7]$$

$$= \frac{V_{gas} - V_{liquid}}{V_{liquid}} \qquad\qquad [5\text{-}8]$$

$$\gg \frac{V_{gas}}{V_{liquid}} \qquad\qquad [5\text{-}9]$$

$$= \frac{(3/2)RT / P_{atm}}{M_{H_2O} / \rho_{H_2O}} \gg 136,000\% \qquad\qquad [5\text{-}10]$$

The maximum stress is reached when the gas is confined to the small volume made available by the water consumed:

$$P = \frac{(3/2)n_{H_2O}RT}{V_{liquid}} \qquad\qquad [5\text{-}11]$$

$$= \frac{(3/2)RT}{M_{H_2O} / \rho_{H_2O}} \gg 200MPa \qquad\qquad [5\text{-}12]$$

Therefore electrolysis can theoretically achieve a strain of 136,000%, and is capable of generating a pressure beyond 200 MPa [154]. At the same time, an electrolysis actuator requires little electrical power and produces minimal heat. Also, thanks to the large volume

expansion through electrolysis, the actuators can have a small volume but a large output force.

It is interesting to note that the electrolysis reaction can be reversed. The generated oxygen and hydrogen can recombine into water. Although extremely slow under normal conditions, the recombination rate can be greatly enhanced in the presence of platinum as a catalyst. The recombination rate depends on the contact area between the platinum and the gases, and on the gas pressure. The higher the pressure, the faster the recombination. The maximum pressure is reached when the gas recombination rate equals the generation rate. Theoretically, devices taking advantage of both forward and reverse electrolysis can be used repeatedly without refilling the electrolyte.

In conclusion, electrolysis actuators are ideal for application to movable probes. These actuators require two electrodes (typically gold, palladium, or platinum) immersed in an electrolyte. When voltage is applied, with water as an electrolyte, electrolysis at the electrodes produces oxygen and hydrogen gases. This reaction is reversible when the voltage polarity is reversed in the presence of a catalyst such as platinum. Placing the reaction in a sealed chamber, results in an actuator.

5.1.2.2   Electrolysis Actuators

Electrolysis is a good method for high-performance actuation. The electrolysis pump was first demonstrated by Xie [98, 100]. Figure 5-4 shows an electrolysis-based pumping system for electrospray applications. It consists of electrolysis pumping electrodes, solvent chamber, passive mixer, and electrospray nozzle. Characterization of the pumps was done using a 95/5/0.1 (water/acetonitrile/formic acid), a typical solvent used in LC applications. Higher flow rates at higher pressures can be achieved by simply increasing the current. The

electrolysis actuator can produce > 200 psi of pressure. Pumping efficiency up to 40% has

been observed.
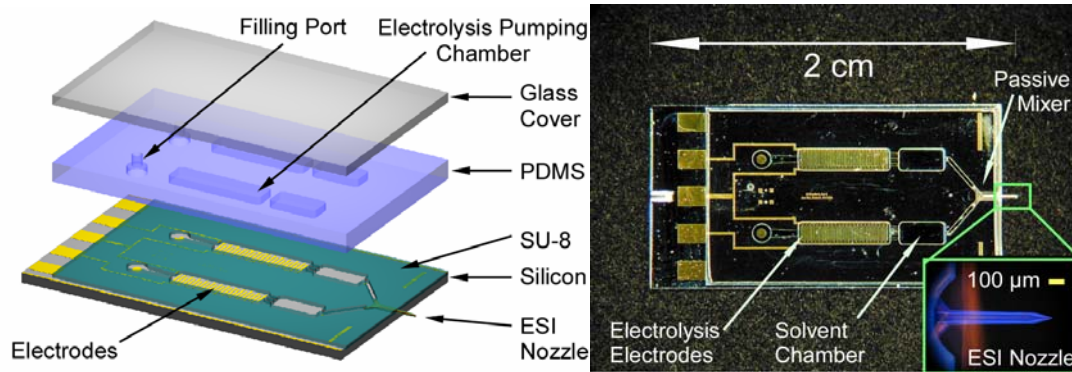
Figure 5-4   Integrated electrolysis pump system

Figure 5-5 shows a parylene channel for electrolysis pressure test consisting of

interdigital electrodes embedded under the 100-μm-wide and 25-μm-high channel. The

electrodes were built by evaporating and patterning a Ti/Pt/Au (300Å/2000Å/1000Å) layer.

Two electrode spaces were fabricated: (1) 5-μm-wide electrodes at 5-μm intervals; and (2)

3-μm-wide electrodes at 7-μm intervals.
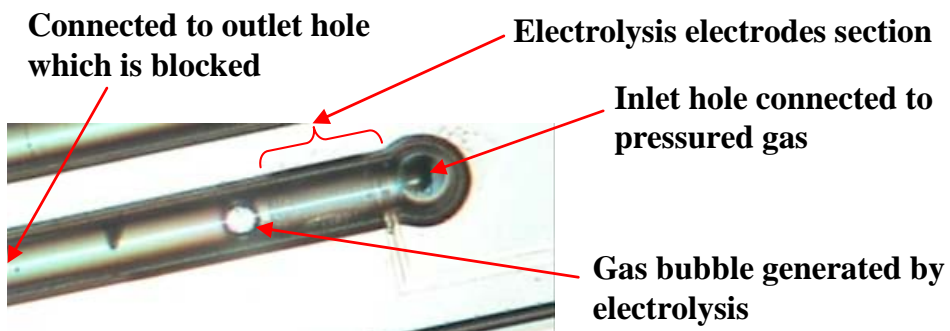
Figure 5-5   The parylene channel for electrolysis pressure test

The electrolyte used in testing is DI water with 10% ethanol and 1% acetic acid. The electrolyte solution is pumped into the device using a compressed N_2 tank. Then the outlet of the device is sealed. The solution in the device is kept under pressure from the gas tank.

First, a bubble is generated using electrolysis with constant current. The bubble shrinks or expands, depending on whether its internal pressure is lower or higher than the system pressure applied by the compressed nitrogen. By adjusting the nitrogen pressure, a balance pressure can be found for each current level, which maintains the bubble size. At this balance point, gas generation and recombination rates are equal. This pressure can be considered the maximum pressure possible for the device at that fixed current.

At every balance point, the bubble is monitored for over 5 minutes to ensure its size does not change. The error for the obtained balance pressures is about ± 2 psi. The balance pressures are plotted against electrolysis currents in Figure 5-6. The device with 5-μm-wide electrodes and 5-μm electrode spacing always generates higher pressures than the one with 3-μm-wide electrodes and 7-μm electrode spacing, because the former is more efficient in bubble generation. From the figure, it can be seen that 1.1 μA of current can generate a maximum of 150 psi in the device with 5-μm electrodes. Pressures as high as 300 psi have been achieved when the 5-μm-electrode device was tested at 5 μA.

The voltages at the balance points are also recorded and plotted against the balance pressures (Figure 5-7). The device with 3 μm–7 μm electrodes always needs higher voltage to achieve the same pressure generated by the one with 5 μm–5 μm electrodes. The figure also shows a threshold voltage near 3.2 V, above which the balance pressure increases rapidly, meaning significantly more bubble generation from the electrolysis reaction. Hence water electrolysis requires only a few volts to produce enormous relative strains, unlike the

piezoelectrics and other electric-field-responsive materials that demand very high operating
voltages for even much lower strains.
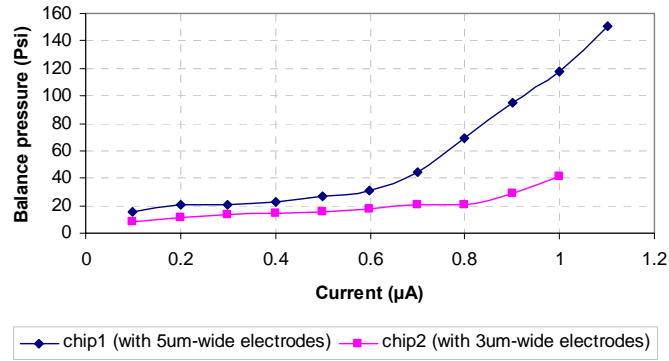
Figure 5-6   Electrolysis balance pressure vs. applied current
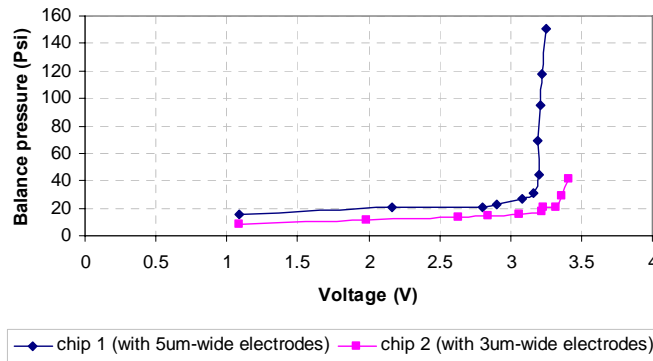
Figure 5-7   Balance pressure for different electrolysis voltages

Figure 5-8 shows a photo and a cross-sectional diagram of a diaphragm-type
electrolysis actuator [85] produced by the Caltech Micromachining Lab. The circular region
is a 2-μm-thick parylene deflected-polymer membrane. As pressure from the electrolyzed
gas grows, the diaphragm bulges. The electrolysis chamber diameter is 2 mm and its height
is 4 μm. Pt is used as both electrodes and recombination catalyst. Maximum deflection
observed is 120 μm.
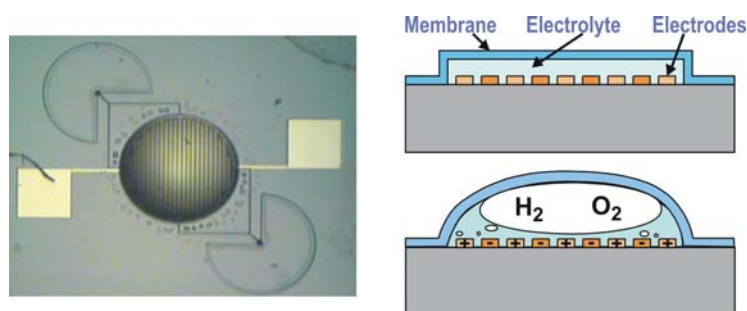
Figure 5-8　Electrolysis diaphragm actuator and electrolysis actuation diagram
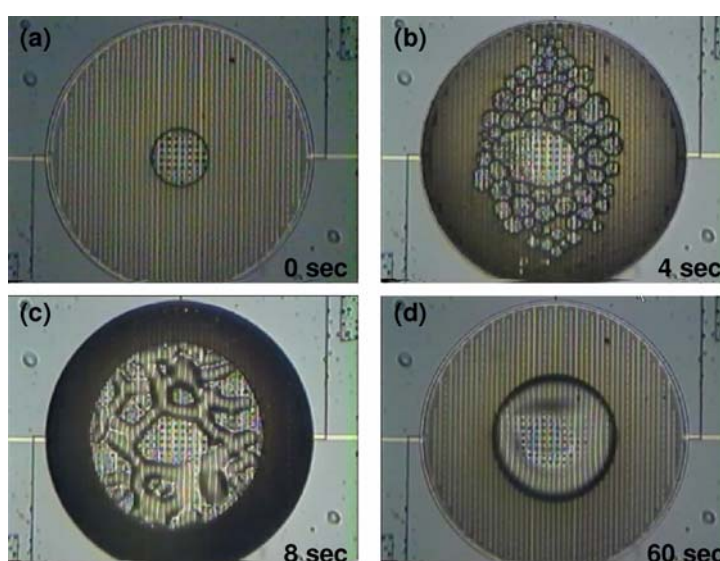
Figure 5-9　Snapshots of activation and deactivation of the actuator filled with DI water

DI water is used as the testing electrolyte. Video snapshots of a bubble generation-recombination cycle are shown in Figure 5-9. In Figure 5-9(a), the device is at rest. There is a bubble from the previous cycle at the chamber center. When an adequate voltage is applied to the two electrodes, bubbles appear immediately and then coalesce into one large bubble (Figure 5-9(b)), deflecting the chamber membrane. In a controlled actuation, constant current is used instead of constant voltage, because the amount of generated gas is directly proportional to the charges injected into the solution. In the very

beginning of the electrolysis, voltage and current follows an approximately linear relationship. For the particular device tested, the voltage starts at 80 V for a current of 0.24 mA, corresponding to a power consumption of 19 mW. The voltage rises over time for a constant-current operation, since the impedance in the chamber increases. The bubbles continue to accumulate, generating higher and higher pressure, which deflects the membrane more and more until the voltage is removed (Figure 5-9(c)). The maximum deflection observed for the device is 120 μm, above which the parylene membrane delaminates from the substrate due to high pressures inside the chamber.

Since Pt electrodes are used, the recombination of hydrogen and oxygen is catalyzed. The mixed gas bubble shrinks quickly when some of the gases are converted back to water. At the same time, the internal pressure reduces, thus the flexible parylene membrane returns to its original position (Figure 5-9(d)). However, there is always a small bubble left which does not disappear even after several days. This is possibly because the small bubble is no longer in contact with the Pt electrodes, and therefore the recombination rate is extremely low.

5.2   Electrolysis-based Silicon Diaphragm Actuators

5.2.1   Introduction

Electrolysis-based diaphragm actuators [155, 156] were designed, fabricated and characterized for the application to movable probes. The actuators require modest electrical power and produce minimal heat. Due to the large volume expansion obtained via electrolysis, the small actuators can create a large force. Up to 100 μm (comparable to the average neuron-to-neuron distance) of movement was achieved by a 3-mm diaphragm. The bidirectional movement can be linearly controlled by small currents. The actuator has proved

latchable. While electrolysis-based actuators may not extend rapidly, our preliminary results show that such speed is unnecessary. Overall, the results support the promising aspects of electrolysis-based movable neural probes.

5.2.2 Simulations

The loading-deflection behavior of a flat rectangular membrane, schematically shown in Figure 5-10 with the two sides 2a and 2b ($a \leq b$), can be described using the Eqs. 5-13, 5-14, and 5-15:

$$p = \frac{C_1 \sigma t h}{a^2} + \frac{C_2 E t h^3}{a^4} \tag{5-13}$$

$$C_1 = \frac{\pi^4 \left(1 + n^2\right)}{64} \tag{5-14}$$

$$C_2 = \frac{\pi^6}{32(1 - \nu^2)} \left\{ \frac{9 + 2n^2 + 9n^4}{256} - \left[\frac{\left(4 + n + n^2 + 4n^3 - 3n\nu\left(1 + n\right)\right)^2}{2\left\{81\pi^2\left(1 + n^2\right) + 128n + \nu\left[128n - 9\pi^2\left(1 + n^2\right)\right]\right\}} \right] \right\} \tag{5-15}$$
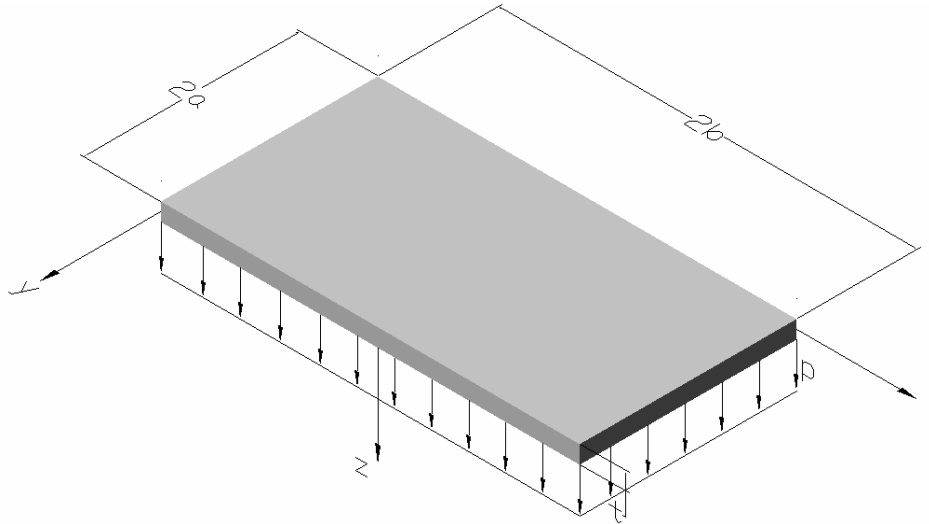
Figure 5-10   Geometry of rectangular membrane

Where p is the pressure generated by electrolysis, E is the Young's modulus of the diaphragm material ($E = 170 GPa$, for silicon), σ is the internal stress, t is the diaphragm thickness, and h is the membrane deflection. C_1 and C_2 are constants determined by the membrane shape and Poisson's ratio, ν. C_1 and C_2 are 3.04 and 1.83, respectively, for a square membrane (b/a=1) with an averaged Poisson's ratio of $\nu = 0.25$ for silicon.

Based on a 300-psi electrolysis pressure, which has already been demonstrated in our lab's previous work, and a silicon diaphragm of dimensions $1000 \times 1000 \times 40$ μm^3, the maximum diaphragm deflection is $h_{max} = 22 \mu m$. We actually anticipate that significantly higher pressures will be realized (up to 1000 psi using an analogous process has already been reported). With these higher pressures, we can reduce the actuator size, or increase its travel. Figure 5-11 shows how deflection scales with electrolysis pressure for different-sized diaphragms.
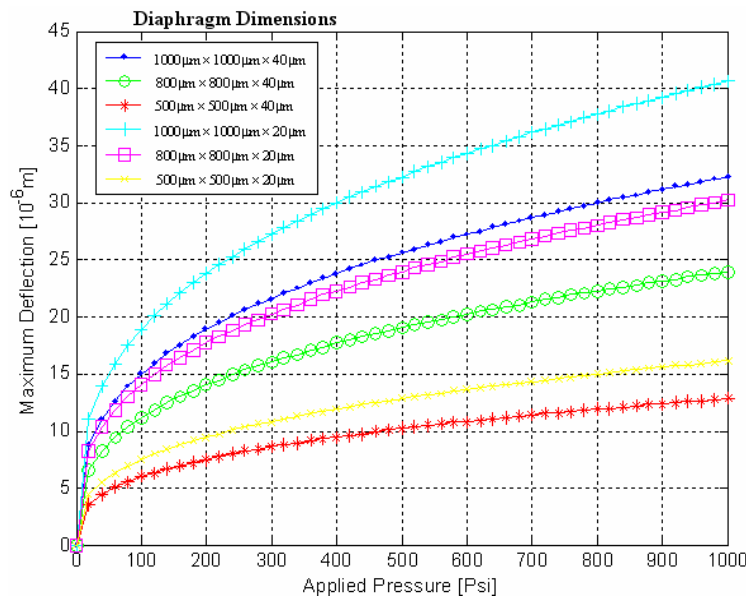
Figure 5-11   Theoretical displacement of a single diaphragm vs. electrolysis pressure for various diaphragm sizes

5.2.3　Design

　　The actuator schematic is shown in Figure 5-12, where two neighboring chambers are etched in the silicon chip using DRIE. The central chamber is for hydrogen (generated by electrolysis), and the outside for oxygen. The chamber volume ratio is 2:1, assuming stoichiometric electrolysis. These two chambers are separated by a high-aspect-ratio ring-shaped wall. On the outside, two channels are used to fill electrolyte into the chambers. Electrolysis electrodes are made on a separate glass chip, which is later bonded to the silicon top using polymers. The central silicon membrane (with a thickness of 40 μm) deflects under the pressure generated by electrolysis. Separating oxygen and hydrogen in different chambers prevents their recombination; therefore, the diaphragm can maintain its position even when the electrolysis is off, hence latchable. To achieve bidirectional movement, we can reverse the electrolysis polarity. If the electrolysis is reversed, the newly generated gases will mix and the oxygen and hydrogen recombine (in the presence of platinum catalyst), but only to the controlled amount defined by the reversed electrolysis.
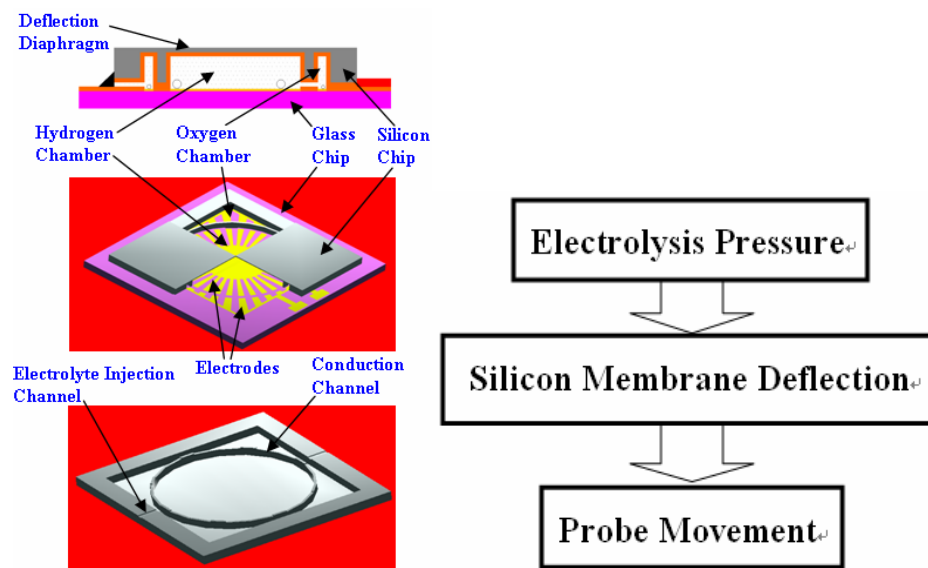
Figure 5-12　Schematic of the electrolysis-based silicon diaphragm actuator
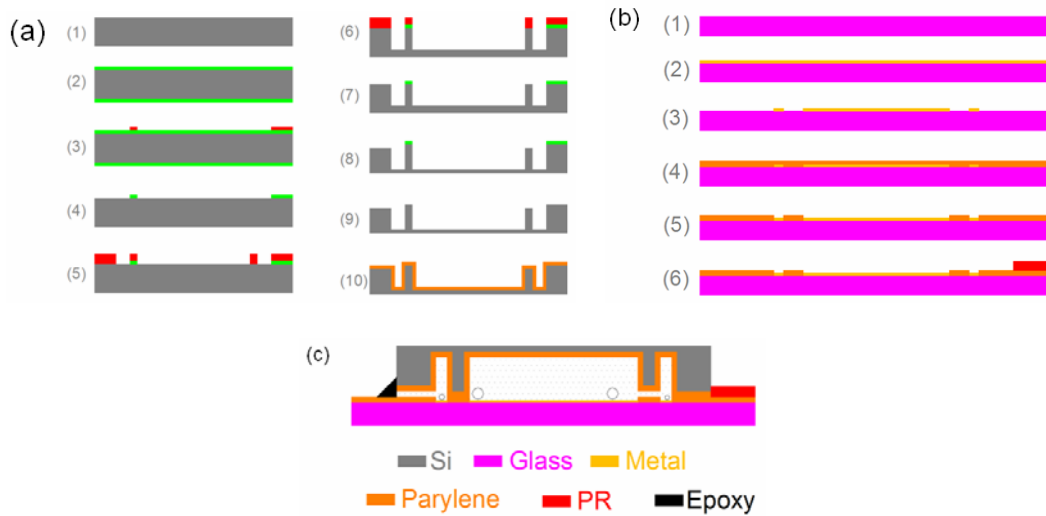
Figure 5-13   Fabrication process flow of the electrolysis-based silicon diaphragm

actuator

The process for the silicon top chip (Figure 5-13(a)) has a two-level DRIE etching. The deep etching is for the gas chambers; the shallow etching is to make conduction and electrolyte injection channels. A variety of actuator sizes have been made, ranging from 400 to 3000 μm (Figure 5-14). The process for the silicon top chip includes: (1) clean wafer (Piranha, 5% HF dip); (2) oxidation 1000 Å SiO_2; (3) pattern photoresist; (4) open SiO_2 window for all etching areas; (5) pattern of thick photoresist layer for deep etching areas; (6) DRIE, etch down the chambers (~ 470 μm); (7) strip photoresist; (8) DRIE, etch 10 μm down for the channels between chambers and the electrolyte injection channels; (9) remove oxide layer; (10) coat bonding polymer.

A Ti/Au layer is for the electrode on the glass chip (Figure 5-13(b)). The process for the glass bottom chip includes: (1) clean wafer; (2) deposit metal layer (Ti/Au); (3) pattern the metal layer for the electrolysis electrodes; (4) deposit bonding polymer; (5) pattern the polymer layer; (6) coat and pattern photoresist for assemble aligner.

Bonding polymer (either parylene or photoresist) is applied to bond the silicon top and the glass bottom chips (Figure 5-13(c)).

5.2.4 Fabrication Results

Figure 5-14 shows the DRIE fabricated silicon top chips. Central and outside chambers are etched 480 μm deep into silicon, leaving a 40-μm-thick membrane at the bottom. Because of the high-aspect-ratio etching performance of DRIE, the ring-shaped separation wall is made 50 μm wide and 480 μm deep. 10 μm is etched to make the conduction channels between the two chambers and the electrolyte injection channels.
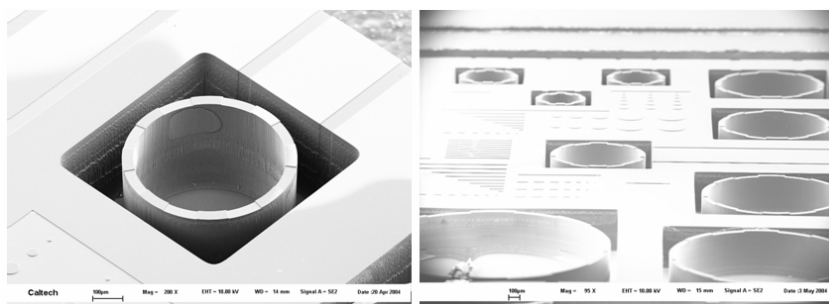
Figure 5-14   SEM pictures of the actuator chambers

Figure 5-15(a) shows the Ti/Au electrodes on the glass chip, with cathode for the central hydrogen chamber and anode for the outside oxygen chamber. Acute electrolysis is well performed using the electrodes by 3 V DC input, as shown in Figure 5-15(b).
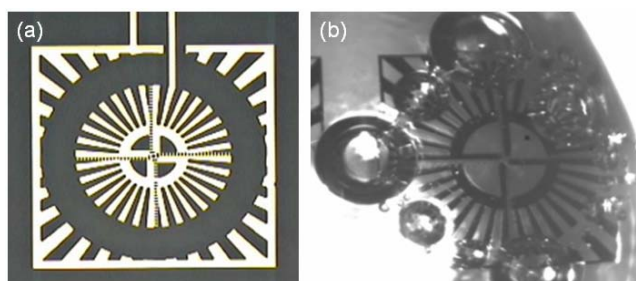
Figure 5-15   (a) Electrodes of the actuator; (b) electrolysis generated by the electrodes

A photoresist layer is patterned as the aligner to help assemble the silicon chip onto the glass chip. The photoresist aligner fits in the cavity of the silicon chip (Figure 5-16(a)), reflows at 160 $^{\circ}$C, and sticks the two chips together after it is cooled down (Figure 5-16(b)). Then we use thermal bonding to bond the two chips firmly and seal the chambers around the side wall, leaving only the conduction channels and electrolyte injection channels open. We tried two kinds of bonding methods using, parylene or photoresist [157]. Based on the diaphragm deflection experiment data, calculation shows that the photoresist bonding can hold under pressure as high as 500 psi. Figure 5-17 shows the SEM pictures of a photoresist bonded device. Photoresist provides very good sealing capability.
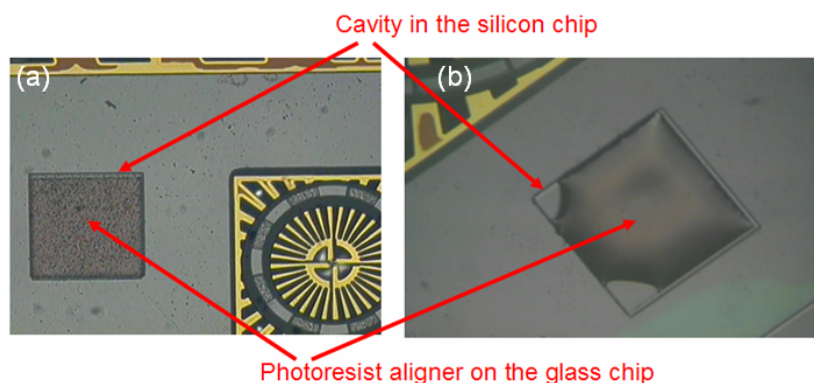
Figure 5-16 (a) Device aligned by photoresist aligner; (b) photoresist aligner reflows in the silicon cavity and sticks two chips together (Pictures were taken from back-side of the glass electrode chip after the two chips were assembled together.)

Filling the chambers with electrolyte is done by immersing the bonded chambers in electrolyte under vacuum, where the air in the chambers is first evacuated and then immediately filled by the liquid. After filling, a small amount of epoxy is used to seal the electrolyte injection channels. Figure 5-18 shows the liquid-filled chambers under fluorescence.
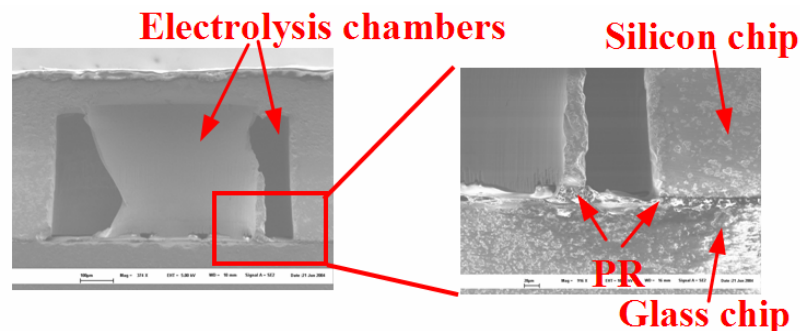
Figure 5-17   SEM pictures of the cross section of the photoresist bonded device
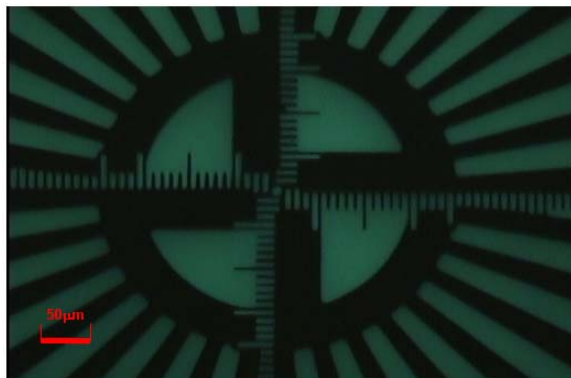
Figure 5-18   Fluorescent microscope image of the electrolyte-filled chamber

5.2.5   Testing Results

Deflection tests are first performed on the actuators by electrolysis (Figure 5-19). The deflection is calibrated by an electromagnetic displacement sensor with 0.02 μm resolution. Figure 5-20 shows the maximum deflections the actuators can achieve by applying 5 V electrolysis voltage. Up to 100 microns of movement can be achieved by a 3-mm diaphragm. Experiment data show that the diaphragm increasing deflection rate depends linearly on the electrolysis current; Figure 5-21 shows that the actuator movement can be linearly controlled by current. The latchable and reversible movement is also demonstrated using the electrolysis actuators. Because hydrogen and oxygen are stored in

two separated chambers, preventing recombination, Figure 5-22 shows that the diaphragm can hold the position, even with no power input. And when we reverse the voltage polarity, recombination happens in each chamber, the diaphragm moves backward, and then goes forward after the recombination is finished. For example: in the central hydrogen chamber, after the voltage polarity is reversed, oxygen is generated and meets the original hydrogen to recombine to water, resulting in backward movement of the membrane. After hydrogen is totally recombined, more oxygen is generated in the chamber and the pressure increases again, therefore the membrane goes forward again. Figure 5-22 also shows several cycles of bidirectional movements. We observed that the membrane cannot totally come back to the original position. This is because only the gas on the chamber bottom, which contacts the electrode, recombined. Some of the gases stay in the top of the chamber, because recombination occurs very slowly without catalyst. Although the gases didn't completely recombine in this experiment, this can be improved by adding platinum catalyst into the electrolyte.

Figure 5-19   Electrolysis in the actuator's chamber
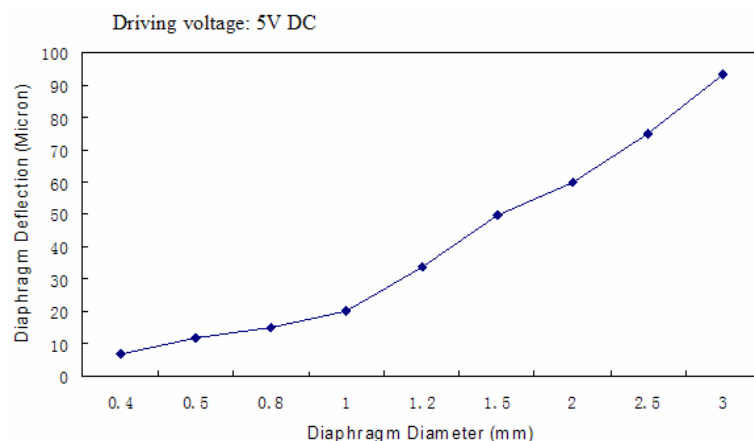
Figure 5-20   The deflection of different size actuators under 5 V voltage
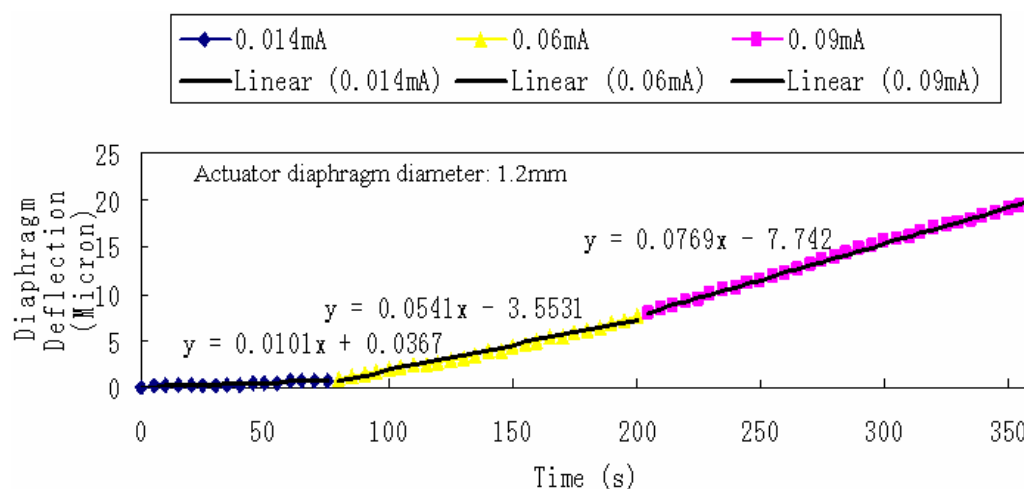
Figure 5-21   Diaphragm deflection under different driving currents

In conclusion, a large-force bidirectional electrolysis actuator is fabricated with MEMS technology. Up to 100 μm of movement is achieved by a 3-mm diaphragm. With powerful (to penetrate brain tissue), high-density, low power, bidirectional, and latchable (without power) capability, the actuator shows promise for electrolysis-based movable neural probes.
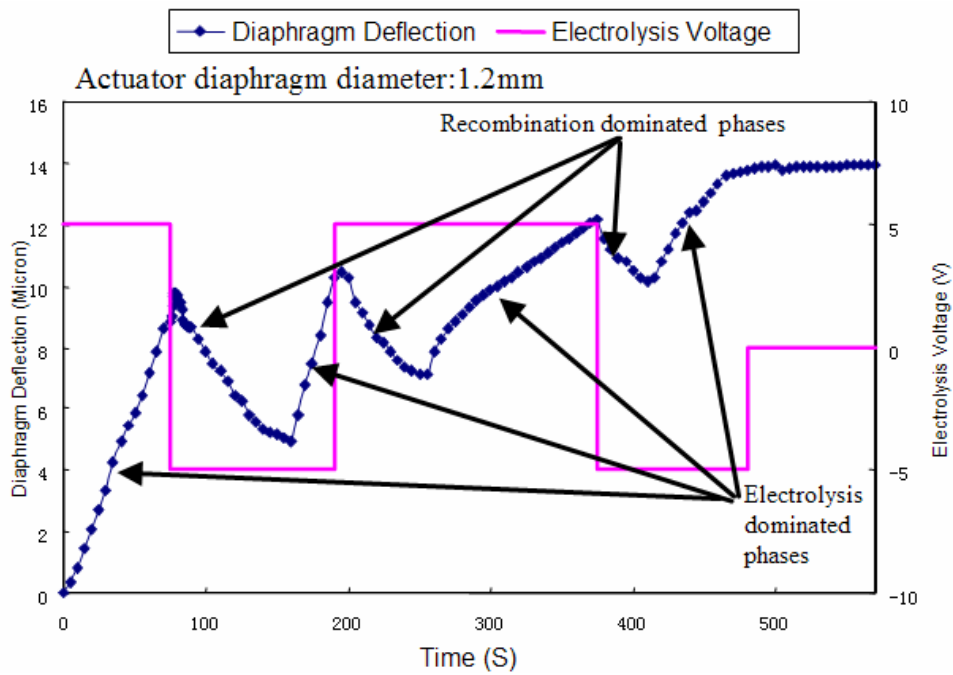
Figure 5-22   Actuator's reversing and latching capability testing

5.2.6   Bellows Structure Design and Future Work

In order to reduce the diaphragm size and have large displacement at the same time, a novel electrolysis-based bellows actuator is designed, as shown in Figure 5-23. The bellows creates the electrolysis chamber, and can add multiple diaphragm deflections together. Therefore larger probe movement can be achieved.
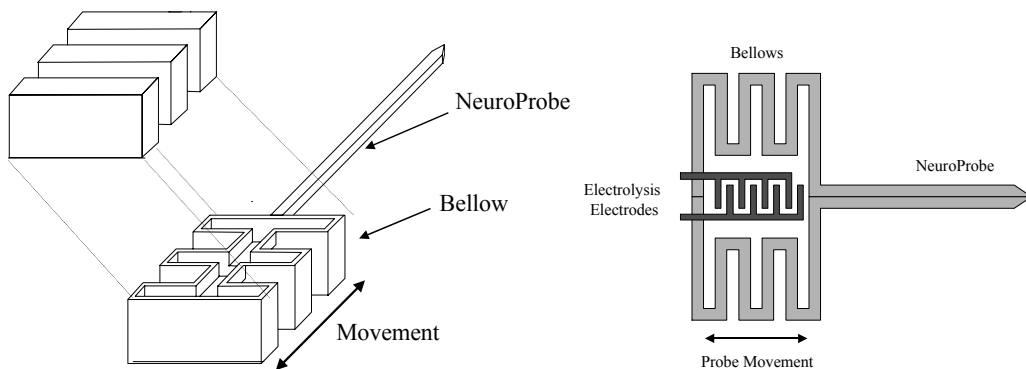
Figure 5-23   Electrolysis-actuated MEMS bellow concept for moveable probe
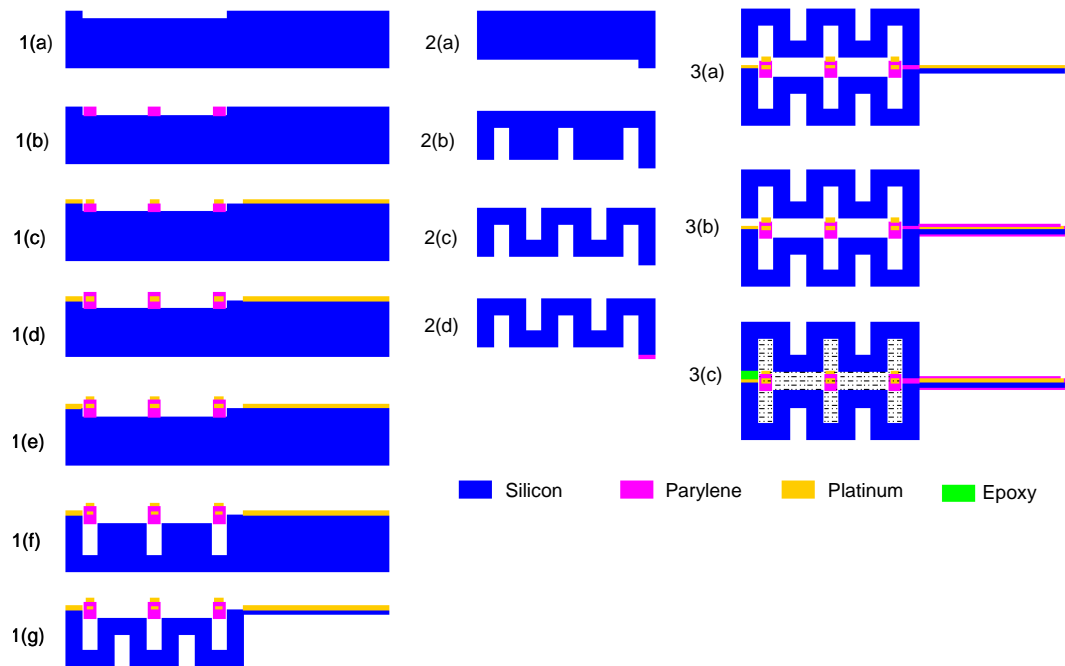
Figure 5-24   Bellows and electrode fabrication process flow

Bottom half bellow process: (a) front-side shallow DRIE etch of electrolysis-bridge channel, (b) deposit and pattern CVD parylene for metal support, (c) platinum lift-off metallization for recording electrodes, (d) deposit and pattern parylene for Pt insulation, (e) deposition and lift-off patterning of platinum for electrolysis electrodes, (f) front-side deep DRIE forms electrolysis chamber and frees the electrolysis electrodes, (g) back-side deep DRIE forms diaphragm, followed by front-side shallow DRIE to form electrode shaft. 2. **Top half bellow process**: (a) back-side DRIE of electrolysis-bridge channel and electrolyte injection channel, (b) back-side deep DRIE forms electrolysis chamber, (c) front-side deep DRIE finishes top half bellow, (d) deposition of insulation and bonding parylene. 3. **Bellow bonding, filling, and sealing**: (a) parylene bonding of complete bellow and the formation of the filling channel, (b) (optional) deposition of parylene to insulate the probe and laser opening of the platinum electrodes, (c) vacuum electrolyte filling and sealing of the bellow with epoxy.

We propose to use a double-side deep reactive ion etching (DRIE) process to machine the multiplayer bellow structure. We will build half-bellow structures separately, and then bond the two halves together to form an actuator. The major proposed processing steps are shown in Figure 5-24. The integrated recording electrode is made as part of this process. First, a front DRIE creates the chamber connection channel (1a). Then, parylene is deposited and patterned as an insulating and free-standing flexible cable layer (to connect the actuator to an external voltage source) (1b). Platinum is deposited and lift-off-patterned

on the parylene layer to form the recording electrodes (1c). The Pt metal wires also transmit signals over the bellow chamber. Next, another parylene layer is deposited to cover and insulate the recording electrode layer (1d). A second layer of platinum is deposited and patterned as electrolysis electrodes, followed by the second (but deep) front DRIE to etch the bellow chamber. Note that this DRIE step only undercuts (but not attacks) the parylene so that a free-standing and flexible cable can be made (1f). After the etching, the electrolysis electrodes are free standing on the parylene layer in the bellow chamber. Next, the back DRIE is performed to etch the bellows folds and the probe shaft structure (1g). The same front and back DRIE etching steps are used to fabricate the other bellows half, together with a channel for the subsequent electrolyte injection (2a-d). The two bellow halves are then bonded together using parylene-to-parylene bonding to form the complete bellows structure. Finally, the probe shafts are coated with parylene and the metal electrodes are opened with laser machining.

The movable probes with bellows actuators can be fabricated in a high-density 2-D array—by stacking 2-D arrays together, 3-D arrays can be made. Flexible parylene cables will provide interconnection to the electrodes. Figure 5-25 shows the schematic of making a 10×10 movable probe array with bellows actuators.
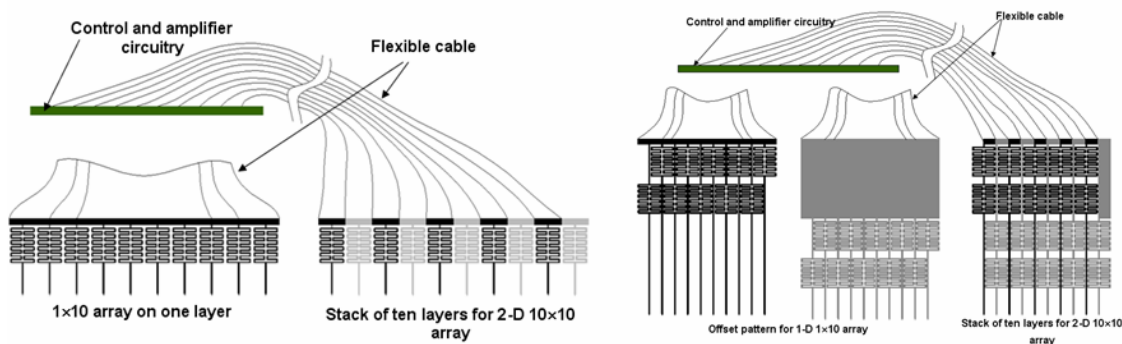
Figure 5-25   Schematic of making a 10×10 movable probe array with bellows actuators

5.3   Electrolysis-based Parylene Balloon Actuators

5.3.1   Introduction

From the previous study, we learned that the functional electrolysis chamber, which has good sealing and large elongation under pressure is the key point in developing a functional electrolysis actuator for application to movable neural probes. The electrolysis chamber materials also need to be biocompatible. Because parylene C is a polymer material with good biocompatibility, large elongation, extremely low gas and moisture permeability, and good adhesion to silicon substrate (Table 1-1), we developed a novel electrolysis-based actuator for movable neural probes using parylene C as the electrolysis chamber material [158], instead of the silicon bellows design. Compared with silicon, parylene has the advantages of better biocompatibility, larger deflection, better sealing (no need for a bonding process to make the chamber), and easier fabrication process. Two types of electrolysis-based parylene balloon actuators have been designed, fabricated, and tested. The results show that the actuators have great potential for use with movable neural probes.

5.3.2   Device Design and Simulation

The electrolysis-based parylene balloon actuator design is shown in Figure 5-26. The neural probe with sensing electrodes and the parylene cable will be fabricated using the same double-side DRIE process introduced in Chapter 4. An electrolysis actuator will be integrated on the base of the probe shank and implanted into the brain tissue with the probe shank, so as to push the probe shank to move after chronic implantation. The electrolysis actuator contains a silicon spring structure, a balloon shape parylene membrane to perform as the electrolysis chamber, and two electrolysis electrodes inside the chamber. Electrolyte

will completely fill the chamber using vacuum filling through a tiny hole poked by a hot probe tip. A little drop of biocompatible epoxy will be used to seal the chamber. As we know, after applying current into the electrolyte via the electrodes inside the parylene balloon chamber, a huge amount of pressure will be generated in the chamber and the parylene balloon will expand under the electrolysis pressure—stretching the silicon spring, and pushing the neural probe shank. If needed, gas recombination will reduce the chamber pressure and pull the probe shank back. Good control of electrolysis and recombination is necessary to precisely control the probe position and perform the reversible and lockable functions.
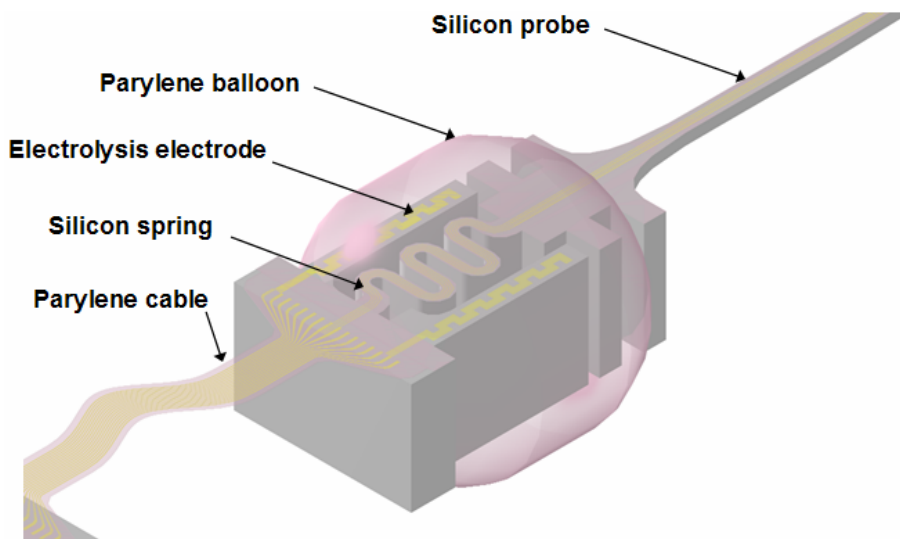
Figure 5-26   Schematic of the electrolysis-based parylene balloon actuator design

The silicon spring structure is very important for the actuator. It needs to be soft enough to elongate, and at the same time it should be strong enough to provide mechanical support for probe insertion. Different spring structures (single spring and double spring) with different parameters (spring size L, number of spring turns or leaves) have been designed, as shown in Table 5-2. Figure 5-27 shows the maximum displacement and stress

simulation for the single-spring structure and the double-spring structure. A FEMLAB mechanical model has been used for the simulation. For this particular case: single-spring structure—L = 500 μm, applied pressure = 100 psi, maximum displacement = 10.35 μm, maximum stress = 174 MPa; double-spring structure—L = 1000 μm, applied pressure = 100 psi, maximum displacement = 22.76 μm, maximum stress = 132 MPa. From the simulation results, we can see that under 100 psi applied pressure, the maximum stress of the silicon spring structure is much less than the silicon failure stress, and from our previous test results, pressure much higher than 100 psi generated by electrolysis was observed, so displacement larger than 22.76 μm is expected for this design.

Table 5-2　Design parameters for silicon spring structure

Single spring structure

Design parameters:
a=b=50μm

	L (μm)	Turns
Type 1	300	5
Type 2	500	5
Type 3	1000	5
Type 4	300	7
Type 5	500	7
Type 6	1000	7
Type 7	300	9
Type 8	500	9
Type 9	1000	9

Double spring structure

Design parameters:
a=b=50μm

	L (μm)	Leaves
Type 1	650	3
Type 2	1000	3
Type 3	650	4
Type 4	1000	4
Type 5	650	5
Type 6	1000	5
Type 7	650	6
Type 8	1000	6

Figure 5-27   Maximum displacement and stress simulation results: (a) single-spring

structure; (b) double-spring structure

5.3.3   Fabrication

A silicon probe is fabricated using the double-side DRIE process introduced in

Chapter 4. The silicon spring structure is fabricated on the probe shank base at the same time.

Figure 5-28 shows the spring structure with different geometric designs. Sensing electrodes

and electrolysis electrodes are built on the probe shank tip and spring structure separately.

Figure 5-28(c) and (d) show the electrolysis electrode on the spring structure.

A photoresist sacrificial ball is painted around the spring structure using a paint

brush. 100 $^{\circ}$C oven bake is used to harden the photoresist. Bubbling in the photoresist is the

biggest issue in controlling the ball shape of the sacrificial photoresist. In order to figure out

this issue, two types of photoresist and three steps of painting are used. The first step is to

use AZ1518 photoresist, which is the photoresist with lower viscosity, to fill the trench in the spring structure. After oven baking, the second painting uses AZ4620 photoresist, which is the photoresist with much higher viscosity, to form the ball shape. But air bubbles may still exist in the photoresist, causing problems later. To remove the bubbles, a vacuum process is used before the second oven bake. A third painting is performed to modify the ball shape of the photoresist using AZ4620 if necessary. The final oven bake is to harden the photoresist ball. A photoresist sacrificial ball is shown in Figure 5-29.
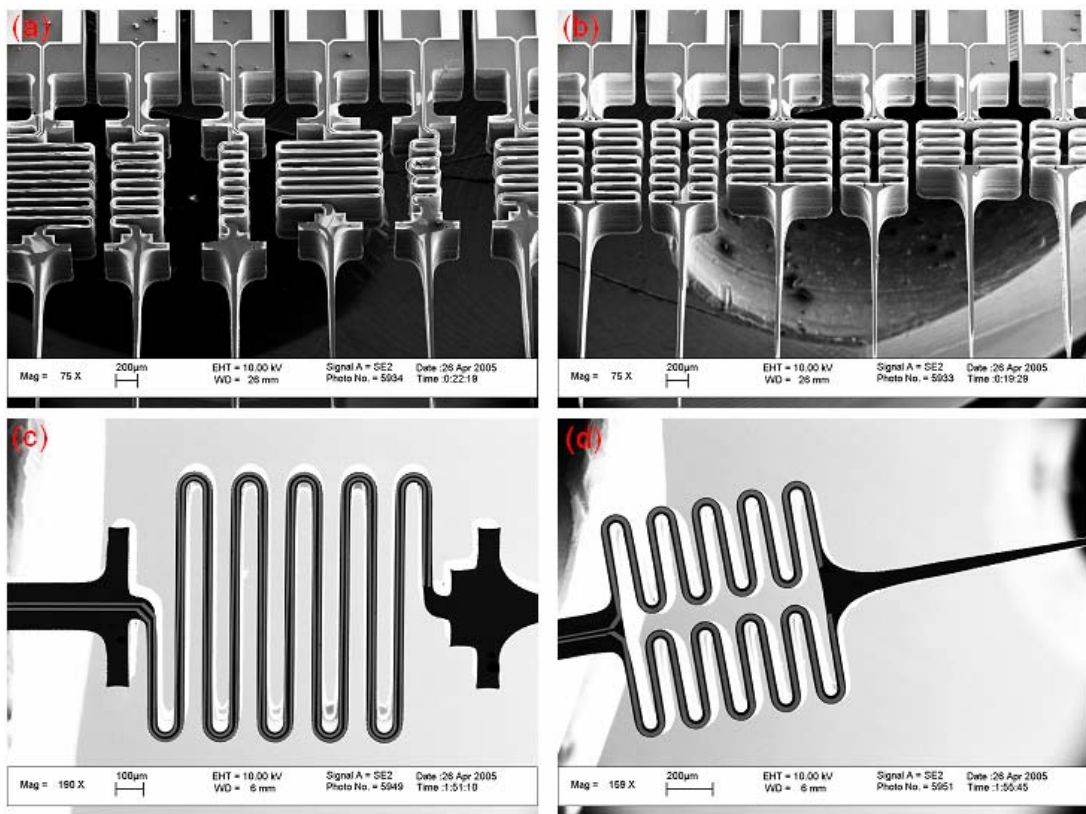
Figure 5-28   SEM pictures of silicon spring structure: (a) array of single-spring structures; (b) array of double-spring structures; (c) single-spring structure with electrolysis electrodes; (d) double-spring structure with electrolysis electrodes
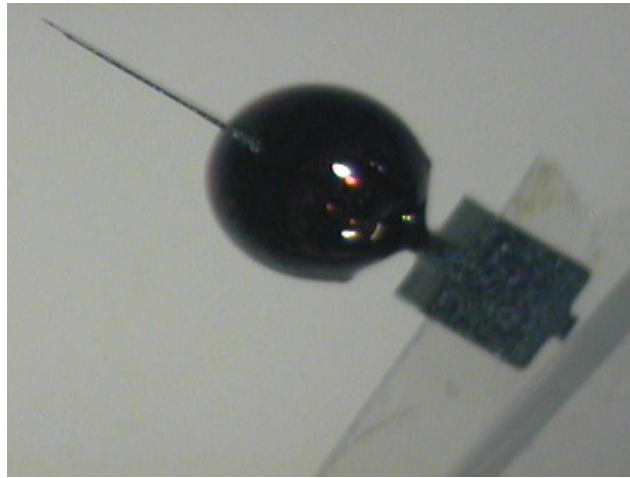
Figure 5-29   Photoresist sacrificial ball painted around the spring structure
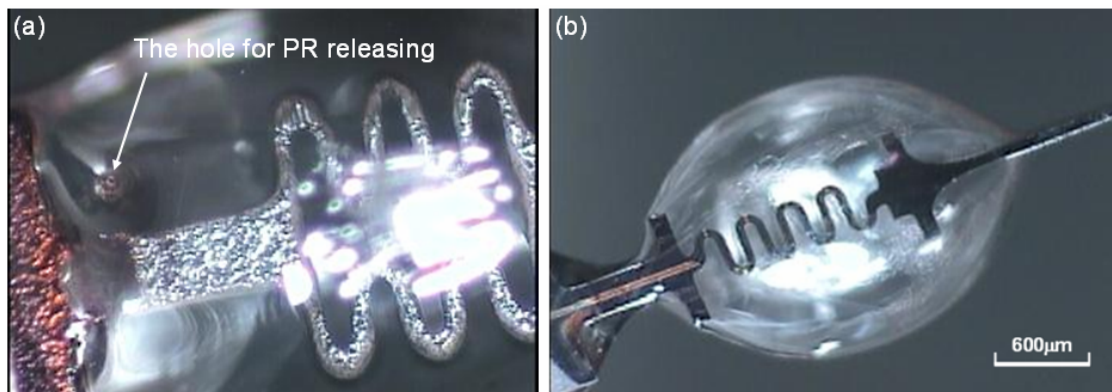
Figure 5-30   (a) The back-side of the parylene balloon, showing the hole for PR releasing

poked by a hot probe; (b) fabricated parylene balloon actuator

A parylene C layer (10 μm) is coated on the photoresist sacrificial ball. As shown in

Figure 5-30(a), a tiny hole is poked in the parylene layer near the base of the silicon spring

structure, using a hot probe. The probe tip is heated by a soldering iron at about 300 ^{o}C,

which is higher than the melting temperature of parylene C, so that it can melt the parylene

C layer and poke through easily. The size of the hole is only about 5 μm to 10 μm, so it can

be easily sealed by epoxy after the parylene balloon is filled with electrolyte. However,

because of the very small hole size, the PR release will take a very long time. The device is immersed in acetone for about one week to release the photoresist inside the parylene balloon. Figure 5-30(b) shows the device after photoresist release. The parylene balloon is filled with electrolyte (95/5/0.1% water/methanol/acetic acid) by immersing it into the fluid under vacuum. This process works well, as demonstrated by the fluorescence photograph (Figure 5-31(a)). A small amount of epoxy is then used to seal the electrolyte filling hole (Figure 5-31(b)).
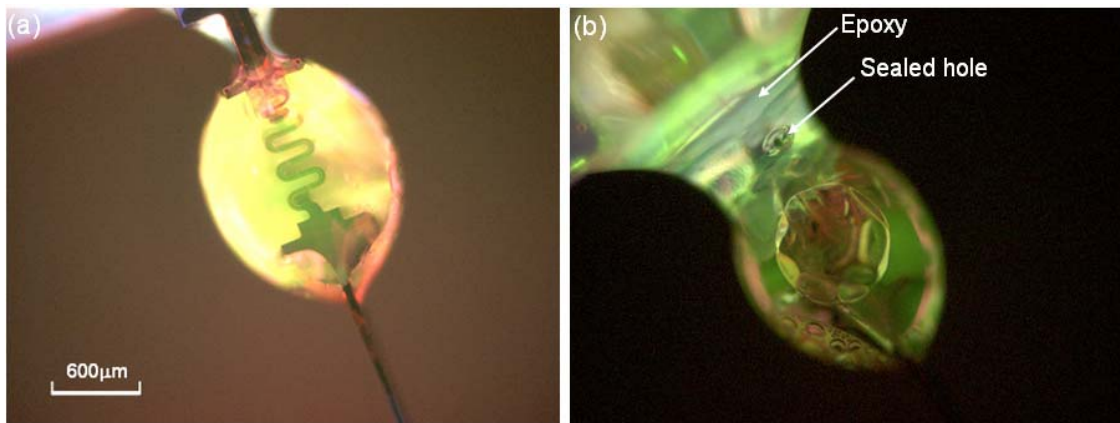
Figure 5-31   (a) Fluorescence picture showing the parylene balloon is fully filled with electrolyte; (b) fluorescence picture showing the back of the parylene balloon sealed by epoxy

5.3.4   Testing Method and Results

The setup for testing the movement of the parylene balloon actuators is shown in Figure 5-32. The testing device is epoxy glued on a glass slide and fixed on a stage. Two adjustable metal probes are used to make electrical contact with the electrode pads on the device, connecting the electrolysis electrodes to the voltage supply. A multimeter is connected to monitor the electrolysis current. An electromagnetic force and displacement

gauge with 0.02-μm resolution is used to measure the probe movement. A 3-D stage is used to make close contact between the tip of the displacement gauge and the tip of the silicon probe. The electrolysis chamber of the actuator is monitored by a stereo scope with CCD camera connected, so the reaction in the chamber during the actuation can be recorded and analyzed later.
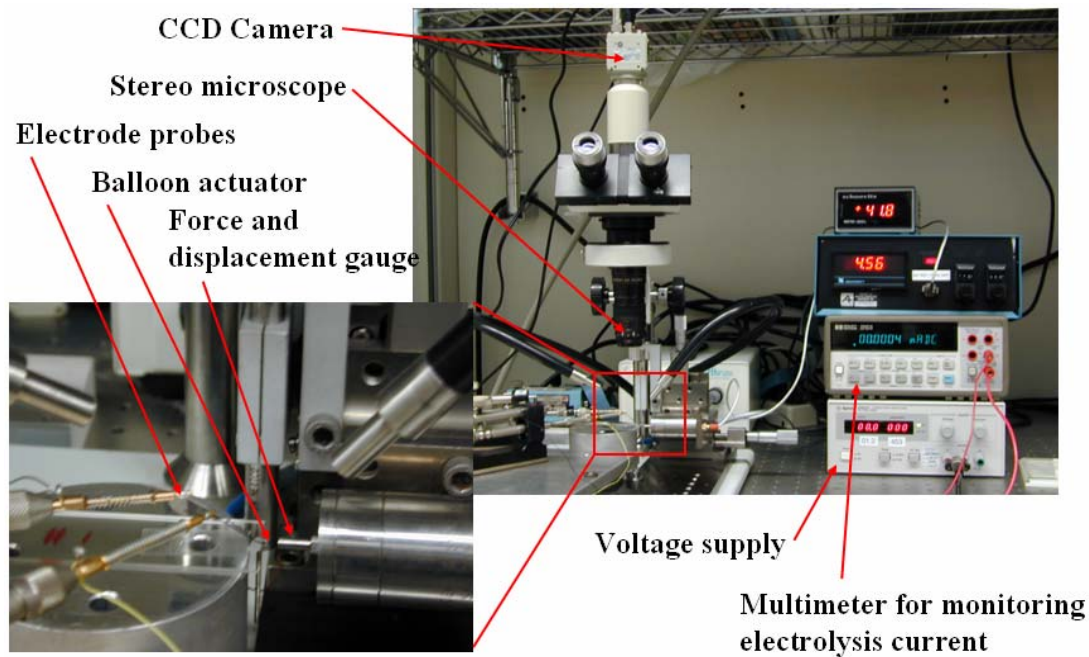
Figure 5-32   Testing setup for the parylene balloon actuator

Figure 5-33 shows the picture of the electrolysis chamber during actuation. Gas bubbles generated by electrolysis are observed inside the chamber, and the parylene balloon expends under the pressure. The probe movement is recorded by the displacement gauge at the same time. The test results are shown in Figure 5-34. The electrolysis current and the actuator movement are recorded: A 3 μm probe movement is observed during the time of current supply. After turning off the current supply, the probe moved back, due to the gas recombination in the electrolysis chamber.
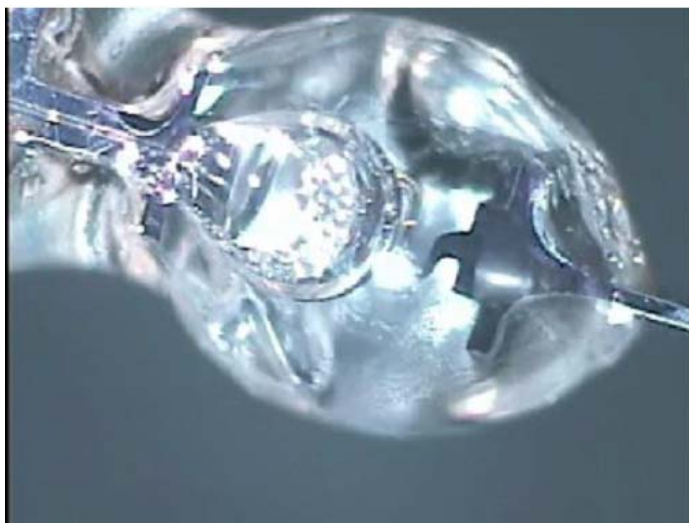
Figure 5-33   Electrolysis inside the parylene balloon of the actuator
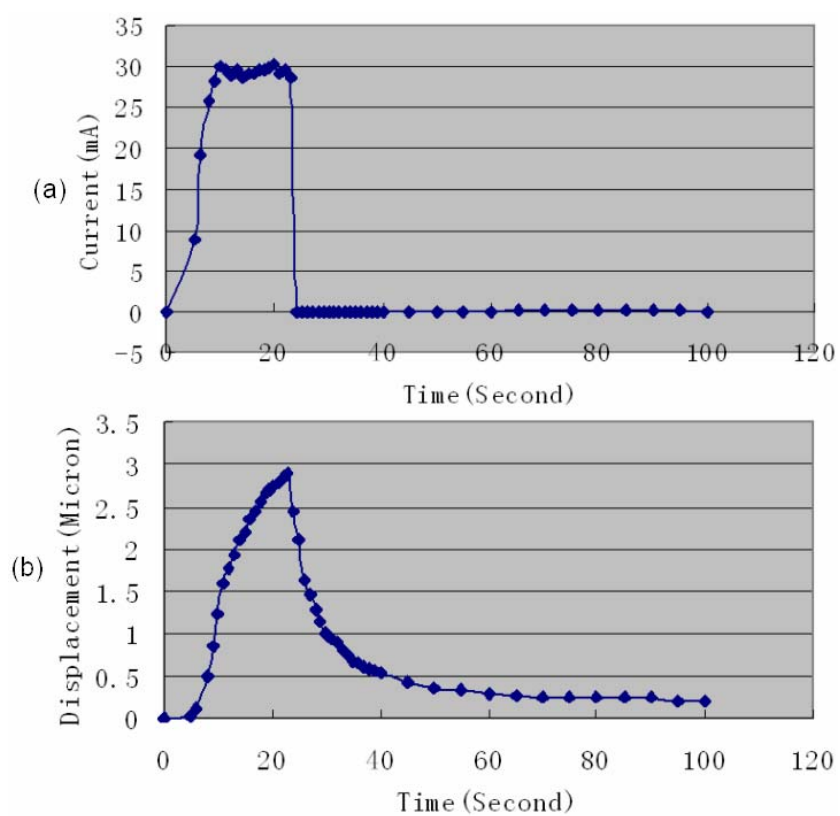
Figure 5-34   One demonstration of the actuator movement: (a) current applied to

electrolysis actuator; (b) actuator movement in the probe shank direction

5.3.5   Discussions

The testing demonstrated the probe movement by electrolysis actuation, although the movement is very small and the actuation is not lockable after power shutoff. Two things may cause the problem: Unlike the silicon diaphragm actuator, this parylene balloon actuator only has one chamber for electrolysis gas storage. That means the gas recombination happens at the same time as the electrolysis, causing very low electrolysis efficiency. Instead of a lift-off process, an etching process is used to fabricate the electrolysis electrodes (Cr/Au ($\sim$ 200 Å / 2000 Å)); electrode shortage may be caused by incomplete metal etching, causing much higher electrolysis current in mA level than in μA level. So modification in device design and fabrication design is needed to further improve the actuator's performance (larger displacement, lower input current, and lockable function).

5.4   The 2nd Generation of Electrolysis-based Parylene Balloon Actuators

5.5.1   Device Design

As we discussed above, the key point in improving the electrolysis actuator performance is good control of the electrolysis and recombination. The problem of the last version of parylene balloon actuator is there is only one electrolysis chamber. As a result, the gases (H_2 and O_2) generated by electrolysis on the two electrodes meet together and recombine to water during electrolysis. So there is no control of the separation of electrolysis and recombination. From the results of the electrolysis-based silicon diaphragm

actuator, we learned that the separation of the electrolysis gases into two chambers is a good method to control the electrolysis and recombination.

The 2nd generation of electrolysis-based parylene balloon actuator is shown in Figure 5-35. Two parylene balloons are designed for the separated electrolysis chambers, which are connected by a parylene channel as salt bridge. The spring structure and electrolysis electrode are inside each parylene balloon. Instead of gold, platinum is used for the electrolysis electrode material, because of its inertness in chemical reaction. A strain gauge is designed to monitor the deformation of the spring structure, so as to detect the probe movement. The double-side DRIE etching process is used to make the neural probes. A parylene cable will be integrated for the final implantable devices.
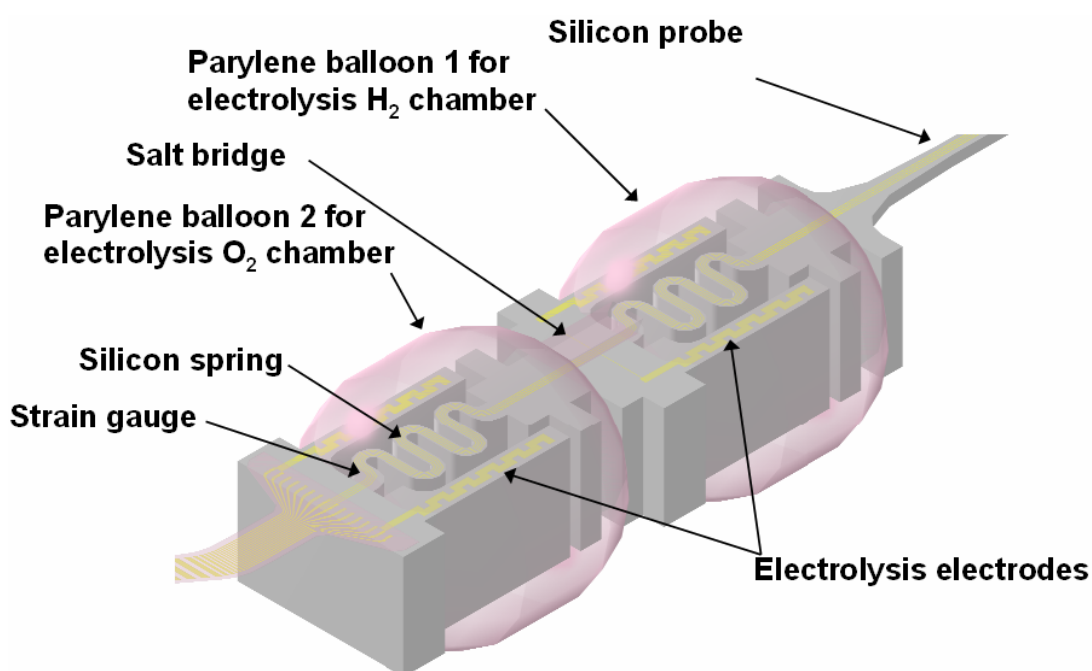
Figure 5-35   Schematic of the device design of the 2nd generation of electrolysis-based parylene balloon actuators with two electrolysis chambers

5.5.2 Fabrication

Two metal layers with parylene insulation are used: a Cr/Au layer for the sensing electrodes, and a Ti/Pt layer for the electrolysis electrodes. The process flow for the probe and spring structure fabrication is shown in Figure 5-36. The process starts with a double-side-polished wafer. XeF_2 silicon etching is performed to etch the silicon down about 1–2 μm. The first parylene layer ($\sim$ 2 μm) is coated on the silicon substrate; the roughened silicon surface provides good adhesion between silicon substrate and the first parylene layer. The Cr/Au (200 Å / 2000 Å) layer is thermally evaporated and patterned by lift-off process; Figure 5-37 shows pictures of the Cr/Au layer. The second parylene payer ($\sim$ 2 μm) is then coated. The Ti/Pt (200 Å / 2000 Å) layer is e-beam evaporated and patterned by lift-off process; Figure 5-38 shows pictures of the electrolysis electrodes and the strain gauge. The third parylene layer is added to protect the metal layers. RIE O_2 plasma etching is used to open the sensing electrode sites, electrolysis electrodes, and metal pads for bonding connection. Another RIE O_2 plasma etching is performed to etch through all the parylene layers to define the probe and spring structure shape. DRIE etching is used to etch into the silicon substrate about 150 μm deep. Back-side DRIE etching defines the thickness of the probe and spring structure ($\sim$ 100 μm). The devices are released in hot ST-22 solvent (120 $^{\circ}$C) to remove all the photoresist used in the process. The SEM pictures of the probe tip and the spring structure are shown in Figure 5-39. Different sizes of the spring structure are designed and fabricated.
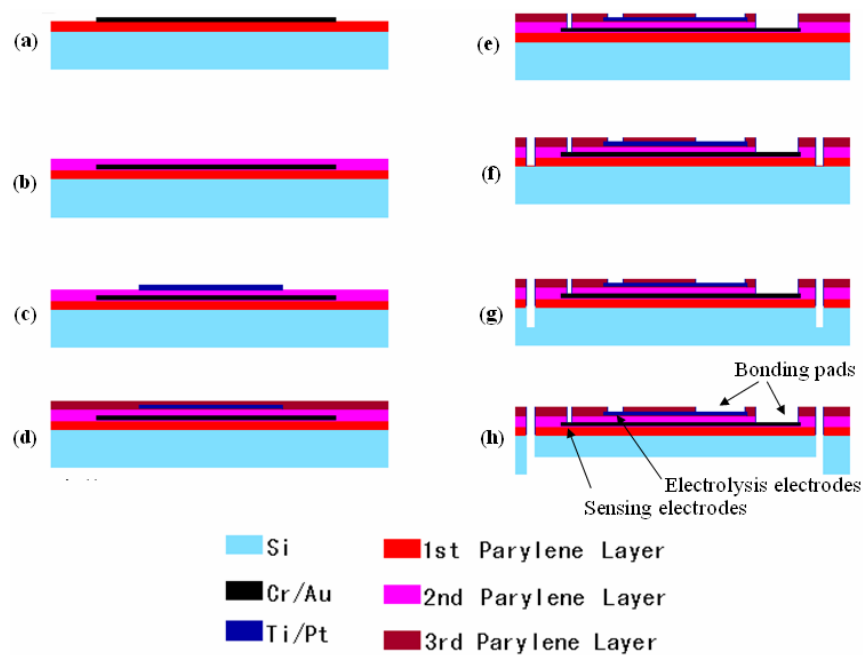
Figure 5-36   Process flow of the probe and spring structures of the 2nd generation of

electrolysis-based parylene balloon actuators with two electrolysis chambers
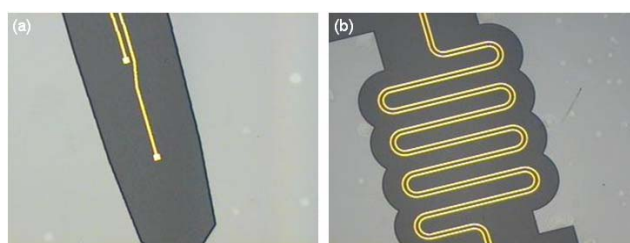
Figure 5-37   Cr/Au metal layer: (a) sensing electrodes; (b) trace lines on spring structure
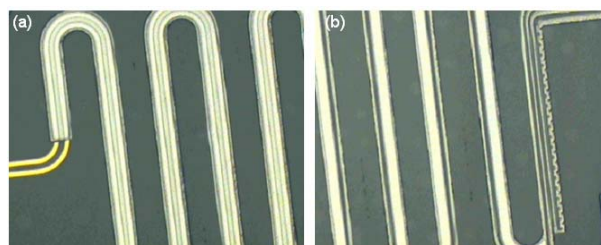
Figure 5-38   Ti/Pt metal layer: (a) electrolysis electrode on the top spring structure; (b)

electrolysis electrode on the bottom spring structure and the strain gauge
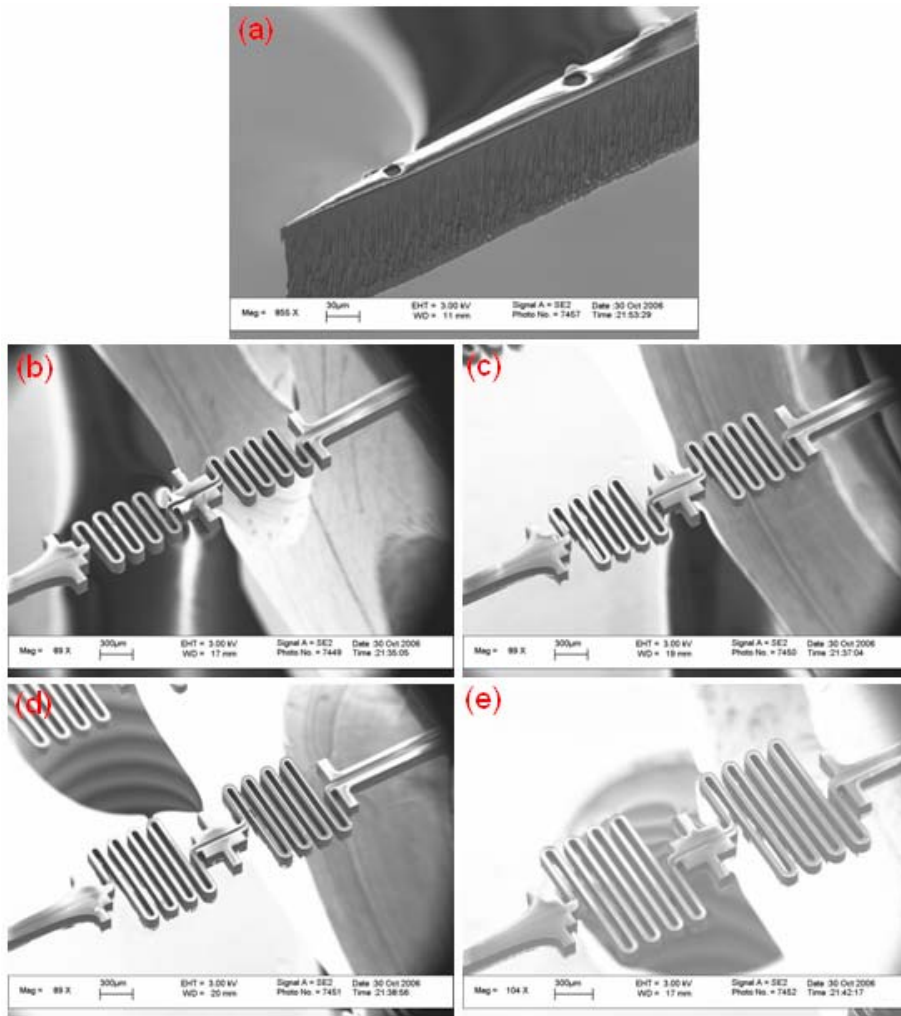
Figure 5-39   SEM pictures of the fabricated neural probe and spring structures: (a)

sensing electrodes; (b) spring structures with 600 μm width; (c) spring structures with

800 μm width; (d) spring structures with 1000 μm width; (e) spring structures with 1200

μm width

Photoresist sacrificial balls are then painted around the spring structures using a
paint brush. A thin layer of photoresist is also painted to connect the two photoresist balls
as the sacrificial layer for the salt bridge. Figure 5-40 shows the photoresist sacrificial balls
after oven bake.
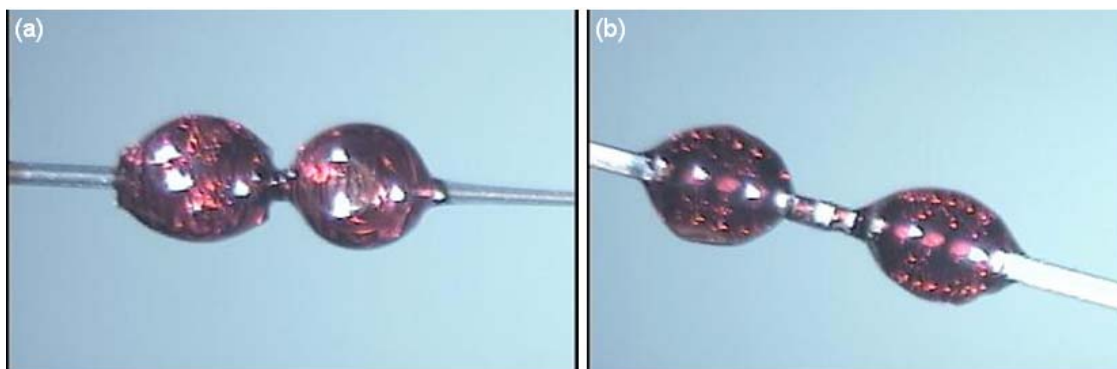
Figure 5-40   Photoresist sacrificial balls around the spring structures: (a) top view; (b)

side view

A 10-μm parylene C layer is coated as the balloon layer. A photoresist-releasing hole is poked by hot probe. The photoresist sacrificial layer is released in acetone by soaking for over a week. Figure 5-41 shows pictures of the released devices.
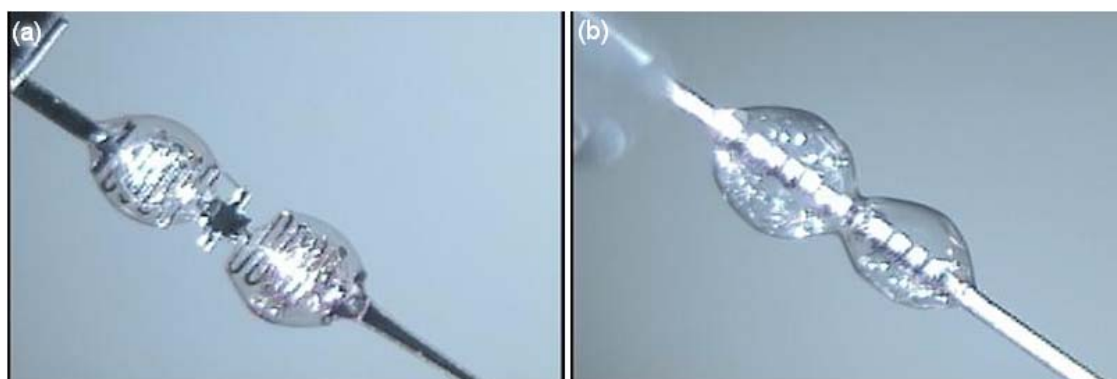
Figure 5-41   Released devices with two parylene balloons: (a) top view; (b) side view

The parylene balloons are filled with electrolyte (95/5/0.1% water/methanol/acetic acid) under vacuum. A small amount of epoxy is then used to seal the electrolyte filling hole.

5.5.3 Testing

To test the Pt electrolysis electrodes, an open electrolysis test is performed using a test chip with the same electrolysis electrodes and silicon trench as the parylene balloon device. As shown in Figure 5-42, a drop of DI water is dropped on the two electrodes and current is applied through the probe contact. Electrolysis bubbles generated on the electrolysis are observed. Applied current and voltage are recorded and shown in Figure 5-43. As we expect, the power consumption is very small. For several volts applied voltage, the current is only in the µA range.
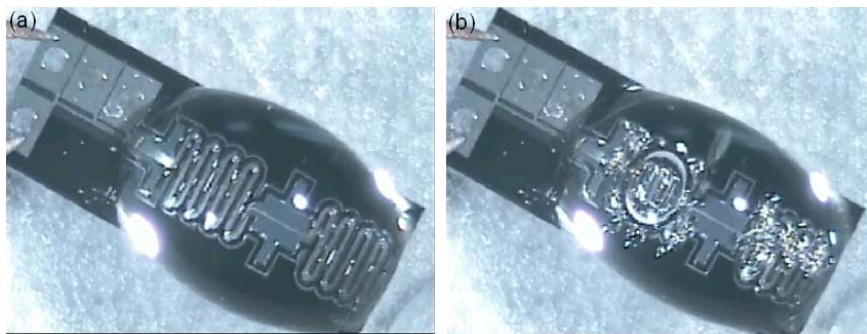
Figure 5- 42   Open electrolysis test: (a) before current is applied; (b) after current is

applied
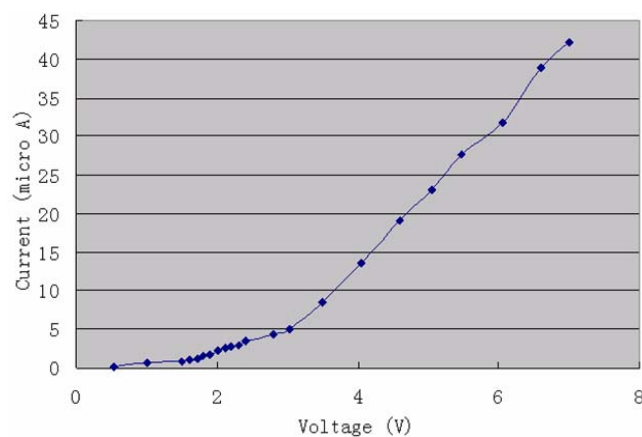
Figure 5-43   I-V curve of the open electrolysis

A device with one big parylene balloon with two spring structures inside is used to test the electrolysis pressure built up inside the chamber. The pictures taken during the test are shown in Figure 5-44. A big gas bubble is observed growing inside the parylene balloon, but unfortunately no probe movement is detected at this time. The problem is in the device fabrication: The parylene balloon is not big enough to surround the spring structures. The side edge of the spring structures anchor into the parylene balloon causing a limitation on the spring expansion. Although there was no probe movement, the huge pressure generated by electrolysis inside the parylene balloon was demonstrated. At the end of the test, the balloon of 10 μm parylene C layer is exploded by the electrolysis pressure. The sealing of the device, including the epoxy sealing and the adhesion between parylene and the silicon substrate, is demonstrated to be good enough for this electrolysis pressure.
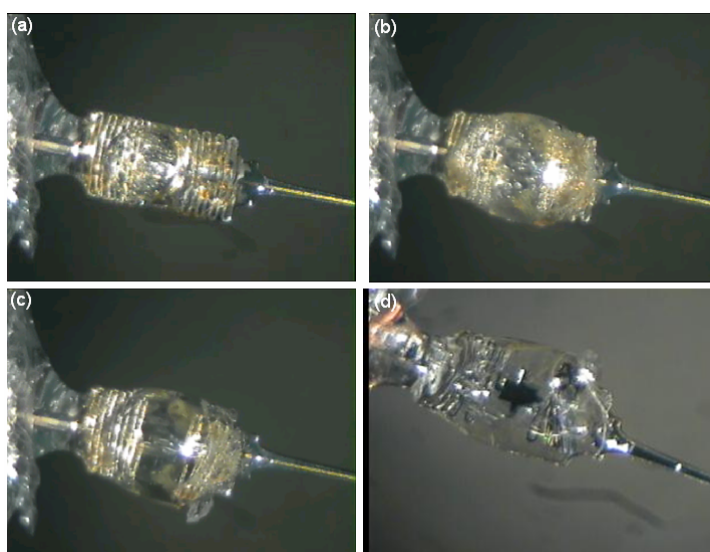
Figure 5-44   Electrolysis test of the device with single parylene balloon: (a) beginning of the test; (b) middle of the test—gas bubbles generated in the parylene balloon; (c) failed device at the end of the test; (d) picture from the back side of the failed device showing the hole on the parylene balloon exploded by electrolysis pressure

A device with a double parylene balloon is tested. The probe movement is detected by an electromagnetic force and displacement gauge with 0.02 μm resolution. The pictures taken during the test are shown in sequence in Figure 5-45. Figure 5-46(a) shows the voltage applied to the electrolysis electrodes, Figure 5-46(b) records the electrolysis current and Figure 5-46(c) shows the detected probe movement. About 18 μm of probe movement is observed in the linear range. The big jump of movement at the end of the test is due to the failure of the salt bridge—the parylene channel between the two parylene balloons. Figure 5-45(d) shows the device after failure. The parylene channel expands, the two parylene balloons connect together, and the spring structure bends, causing device failure.
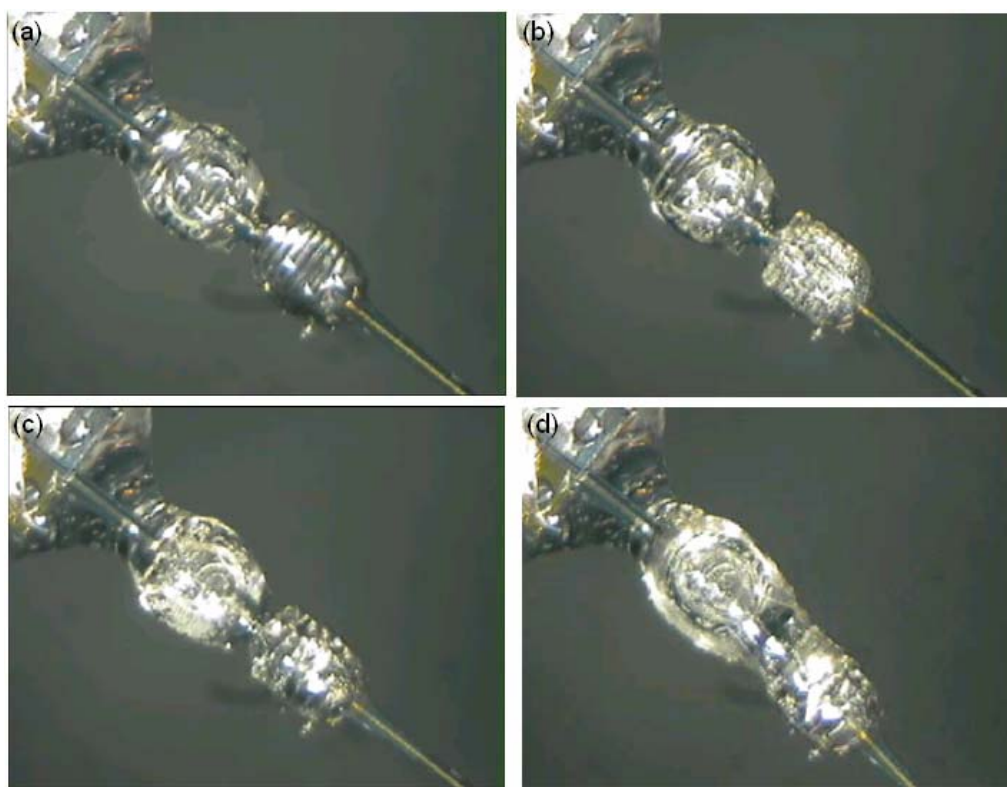
Figure 5-45   Electrolysis test of the device with a double parylene balloon: (a) beginning of the test; (b) (c) middle of the test—gas bubbles generated in the parylene balloon; (d) failed device at the end of the test
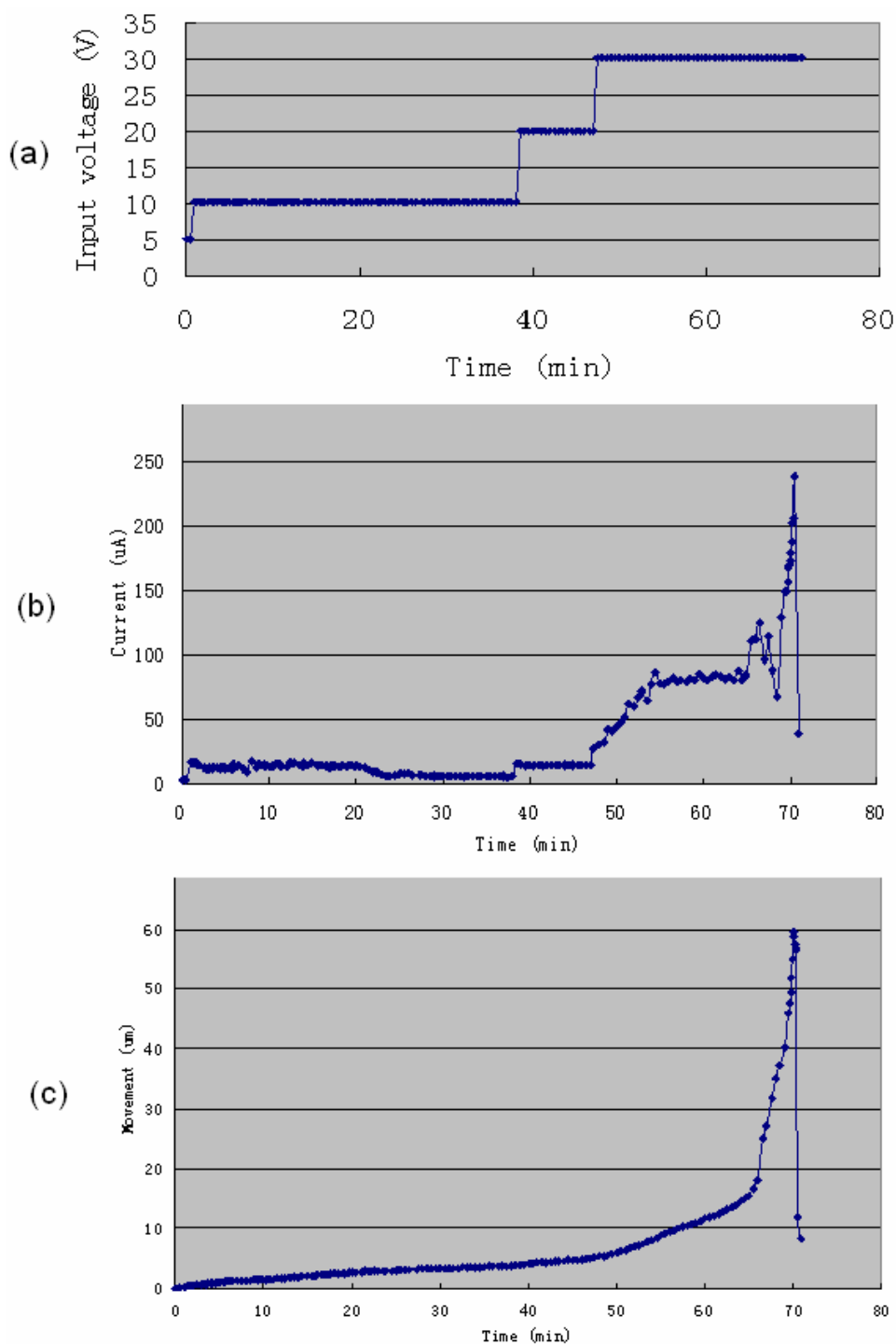
Figure 5-46   Test results of the electrolysis actuator with two parylene balloons: (a)

applied voltage to the electrolysis electrodes; (b) electrolysis current; (c) probe movement

5.5.4 Discussions

From the test results, we demonstrated the efficiency of electrolysis using platinum electrodes: huge electrolysis pressure built inside the parylene balloon, and about 18 μm functional probe movement was seen with two parylene balloons. The reversible and lockable functions can be further tested in the functional movement range. The weak point of the device with two parylene balloons is the salt bridge, the parylene channel connecting the two parylene balloons. The device's performance can be further improved by developing a process to make the salt bridge smaller and stronger.

5.5   Summary

Electrolysis actuation has great potential for use with movable neural probes, because of small size, low power consumption, low heat dissipation, large force and displacement, and lockable and reversible functions. Different types of electrolysis actuators for movable neural probe application were designed, fabricated, and tested. About 100 μm displacement was achieved a by 3-mm electrolysis-based silicon diaphragm actuator. Reversible and lockable control was demonstrated by the silicon diaphragm actuator. A proposed silicon bellows actuator was designed to reduce the actuator's size.

A special parylene coating process was developed to fabricate parylene balloons as the chambers of electrolysis actuators. About 18 μm of functional movement was achieved by an electrolysis-based double-parylene-balloon actuator. The weak points of the parylene balloon actuators and methods to further improve their performance were discussed.

CHAPTER 6

CONCLUSION

We have successfully applied parylene technology to the development of neural probes to make a new generation of neural probes with better functions. We have designed, fabricated, and characterized a new parylene neural probe electrode array with long flexible parylene cable for chronic implantation in the human brain.

Major technical achievements in process development include: combining the parylene coating/etching process with the silicon neural probe double-side DRIE etching process to build parylene on silicon probes as insulating and protecting material; development of a novel process to monolithically integrate flexible parylene cables with neural probes; development of a new RIE etch-back process to completely coat the silicon probe shanks with parylene; development of a novel percutaneous connector with a new Parylene-PCB-Omnetics-connector match-up bonding method to make a 96-channel high-density electrode interface connection for chronic implantation into the human brain.

We optimized both the mechanical and electrical properties of our probe. Probes with different geometries (different shank length, width, thickness, and tip angle) have been

fabricated for in vivo testing in order to determine the best design to make the probes strong enough to penetrate the human pia, and as small as possible to reduce the damage to the brain. We have also fabricated different electrodes and tested the electrode impedance with different materials (Au or Pt) and different sizes of open area, in an attempt to optimize the electrode design for human brain implantation.

A 96-electrode high-density 3-D neural probe array for chronic implantation has been demonstrated. Neural signals were properly recorded using our new parylene neural probes.

Electrolysis actuation has great potential for use with movable neural probes, due to small size, low power consumption, low heat dissipation, large force and displacement, and lockable and reversible functions. The electrolysis-based silicon diaphragm actuators were fabricated by etching separated electrolysis chambers in silicon using DRIE, and using photoresist bonding to seal the chambers. Promising test results of the electrolysis-based silicon diaphragm actuators show 100 μm movement of a 3-mm diaphragm actuator, and controllable electrolysis and recombination for reversible and lockable function.

A special parylene coating process has been developed to fabricate the parylene balloons as sealed electrolysis chambers. The electrolysis-based actuators—both with single parylene balloon and with double parylene balloons—have been fabricated and tested. 18 μm functional movement was achieved by a double-parylene-balloon actuator, and the weak point of the actuators and methods to improve the actuators performance were discussed.

As a conclusion, with the properties of high electrical resistivity, mechanical flexibility, biocompatibility, low coefficient of friction, and an easy deposition/etching

process, parylene is a good material for neural probe applications. The new generation of parylene neural probes has been developed.

REFRENCES

[1]   B. Franklin, "An Account of the Effects of Electricity in Paralytic Cases. In a Letter to John Pringle, M. D. F. R. S. from Benjamin Franklin, Esq; F. R. S," *Philosophical Transactions (1683-1775), * vol. 50, pp. 481-483, 1757.

[2]   R. C. Gesteland, B. Howland, J. Y. Lettvin, and W. H. Pitts, "Comments on Microelectrodes," *Proceedings of the IRE, * vol. 47, pp. 1856-1862, 1959.

[3]   V. S. Polikov, P. A. Tresco, and W. M. Reichert, "Response of brain tissue to chronically implanted neural electrodes," *Journal of Neuroscience Methods, * vol. 148, pp. 1-18, 2005.

[4]   D. H. Hubel and T. N. Wiesel, "Ferrier Lecture: Functional Architecture of Macaque Monkey Visual Cortex," *Proceedings of the Royal Society of London. Series B, Biological Sciences, * vol. 198, pp. 1-59, 1977.

[5]   C. D. Gilbert, "Adult Cortical Dynamics," *Physiol. Rev., * vol. 78, pp. 467-485, April 1, 1998 1998.

[6]   D. McLaughlin, R. Shapley, M. Shelley, and D. J. Wielaard, "A neuronal network model of macaque primary visual cortex (V1): Orientation selectivity and dynamics in the input layer 4Calpha," *Proceedings of the National Academy of Sciences, * vol. 97, pp. 8087-8092, 2000.

[7]   S. A. Deadwyler and R. E. Hampson, "The Significance of Neural Ensemble

Codes During Behavior and Cognition," *Annual Review of Neuroscience,* vol. 20, pp. 217-244, 1997.

[8]   M. A. L. Nicolelis, *Methods for Neural Ensemble Recordings*: Crc Press, 1999.

[9]   R. A. Normann, D. J. Warren, J. Ammermuller, E. Fernandez, and S. Guillory, "High-resolution spatio-temporal mapping of visual pathways using multi-electrode arrays," *Vision Research,* vol. 41, pp. 1261-1275, 2001.

[10]   M. A. L. Nicolelis and S. Ribeiro, "Multielectrode recordings: the next steps," *Current Opinion in Neurobiology,* vol. 12, pp. 602-606, 2002.

[11]   K. L. Hoffman and B. L. McNaughton, "Coordinated Reactivation of Distributed Memory Traces in Primate Neocortex," *Science,* vol. 297, pp. 2070-2073, 2002.

[12]   S. Nirenberg and P. E. Latham, "Population coding in the retina," *Current Opinion in Neurobiology,* vol. 8, pp. 488-493, 1998.

[13]   B. P. Vos, M. Wijnants, S. Taeymans, and E. De Schutter, "Miniature carrier with six independently moveable electrodes for recording of multiple single-units in the cerebellar cortex of awake rats," *Journal of Neuroscience Methods,* vol. 94, pp. 19-26, 1999.

[14]   A. E. Grumet, J. L. Wyatt, and J. F. Rizzo, "Multi-electrode stimulation and recording in the isolated retina," *Journal of Neuroscience Methods,* vol. 101, pp. 31-42, 2000.

[15]   M. A. Wilson and B. L. McNaughton, "Dynamics of the hippocampal ensemble code for space," *Science,* vol. 261, pp. 1055-1058, 1993.

[16]   P. Petersson, M. Holmer, T. Breslin, M. Granmo, and J. Schouenborg, "An imaging system for monitoring receptive field dynamics," *Journal of*

Neuroscience Methods, vol. 104, pp. 123-131, 2001.

[17]   P. J. Rousche, R. S. Petersen, S. Battiston, S. Giannotta, and M. E. Diamond, "Examination of the spatial and temporal distribution of sensory cortical activity using a 100-electrode array," *Journal of Neuroscience Methods,* vol. 90, pp. 57-66, 1999.

[18]   R. S. Petersen and M. E. Diamond, "Spatial-Temporal Distribution of Whisker-Evoked Activity in Rat Somatosensory Cortex and the Coding of Stimulus Location," *J. Neurosci.,* vol. 20, pp. 6135-6143, August 15, 2000 2000.

[19]   A. A. Ghazanfar, C. R. Stambaugh, and M. A. L. Nicolelis, "Encoding of Tactile Stimulus Location by Somatosensory Thalamocortical Ensembles," *J. Neurosci.,* vol. 20, pp. 3761-3775, 2000.

[20]   S. Neuenschwander, M. Castelo-Branco, and W. Singer, "Synchronous oscillations in the cat retina," *Vision Research,* vol. 39, pp. 2485-2497, 1999.

[21]   J. C. Prechtl, "Visual Motion Induces Synchronous Oscillations in Turtle Visual Cortex," *Proceedings of the National Academy of Sciences,* vol. 91, pp. 12467-12471, December 20, 1994 1994.

[22]   K. Frank and M. C. Becker, "Microelectrodes for recording and stimulation," *Physical Techniques in Biological Research, W. L. Nastuk, Ed. New York: Academic,* vol. 5, 1964.

[23]   D. A. Robinson, "The electrical properties of metal microelectrodes," *Proceedings of the IEEE,* vol. 56, pp. 1065-1071, 1968.

[24]   S. Musallam, M. J. Bak, P. R. Troyk, and R. A. Andersen, "A floating metal microelectrode array for chronic implantation," *Journal of Neuroscience Methods,*

vol. 160, pp. 122-127, 2007.

[25] H. Scherberger, I. Fineman, S. Musallam, D. J. Dubowitz, K. A. Bernheim, B. Pesaran, B. D. Corneil, B. Gilliken, and R. A. Andersen, "Magnetic resonance image-guided implantation of chronic recording electrodes in the macaque intraparietal sulcus," *Journal of Neuroscience Methods,* vol. 130, pp. 1-8, 2003.

[26] M. Verzeano and K. Negishi, "Neuronal Activity in Cortical and Thalamic Networks: A study with multiple microelectrodes," *J. Gen. Physiol.,* vol. 43, pp. 177-195, July 1, 1960 1960.

[27] C. A. Terzuolo and T. Araki, "An analysis of intra-versus extra-cellular potential changes associated with activity of single spinal motoneurons," *Annals of the New York Academy of Sciences,* vol. 94, pp. 547-558, 1961.

[28] O. F. Schanne, M. Lavallee, R. Laprade, and S. Gagne, "Electrical properties of glass microelectrodes," *Proceedings of the IEEE,* vol. 56, pp. 1072-1082, 1968.

[29] S. Gagne and R. Plamondon, "Open Tip Glass Microelectrodes: Conduction Through the Wall at the Tip," *Biomedical Engineering, IEEE Transactions on,* vol. BME-34, pp. 56-61, 1987.

[30] T. K. Chowdhury, "Fabrication of extremely fine glass micropipette electrodes," *Journal of Physics E: Scientific Instruments,* vol. 2, pp. 1087-1090, 1969.

[31] S. J. Tanghe and K. D. Wise, "A 16-channel CMOS neural stimulating array," *Solid-State Circuits, IEEE Journal of,* vol. 27, p. 1819, 1992.

[32] J. Ji, K. Najafi, and K. D. Wise, "A scaled electronically-configurable multichannel recording array," *Sensors and Actuators A: Physical,* vol. 22, pp. 589-591, 1989.

[33]   J. Ji, K. Najafi, and K. D. Wise, "A low-noise demultiplexing system for active multichannel microelectrode arrays," *Biomedical Engineering, IEEE Transactions on,* vol. 38, p. 75, 1991.

[34]   J. Ji and K. D. Wise, "An implantable CMOS circuit interface for multiplexed microelectrode recording arrays," *Solid-State Circuits, IEEE Journal of,* vol. 27, pp. 433-443, 1992.

[35]   K. Changhyun and K. D. Wise, "A 64-site multishank CMOS low-profile neural stimulating probe," *Solid-State Circuits, IEEE Journal of,* vol. 31, p. 1230, 1996.

[36]   K. Changhyun and K. D. Wise, "Low-voltage electronics for the stimulation of biological neural networks using fully complementary BiCMOS circuits," *Solid-State Circuits, IEEE Journal of,* vol. 32, p. 1483, 1997.

[37]   R. H. OlssonIii, D. L. Buhl, A. M. Sirota, G. Buzsaki, and K. D. Wise, "Band-Tunable and Multiplexed Integrated Circuits for Simultaneous Recording and Stimulation With Microelectrode Arrays," *Biomedical Engineering, IEEE Transactions on,* vol. 52, p. 1303, 2005.

[38]   Q. Bai, K. D. Wise, and D. J. Anderson, "A High-Yield Microassembly Structure For Three-Dimensional Microelectrode Arrays," *IEEE TRANSACTIONS ON BIOMEDICAL ENGINEERING,* vol. 47, pp. 281-289, 2000.

[39]   Q. Bai and K. D. Wise, "Single-Unit Neural Recording with Active Microelectrode Arrays," *IEEE TRANSACTIONS ON BIOMEDICAL ENGINEERING,* vol. 48, pp. 911-920, 2001.

[40]   Y. Yao, M. N. Gulari, S. Ghimire, J. F. Hetke, and K. D. Wise, "A Low-Profile Three-Dimensional Silicon/Parylene Stimulating Electrode Array for Neural

Prosthesis Applications," in *the 2005 IEEE Engineering in Medicine and Biology 27th Annual Conference*, Shanghai, China, 2005.

[41]   K. C. Cheung, K. Djupsund, Y. Dan, and L. P. Lee, "Implantable multichannel electrode array based on SOI technology," *Microelectromechanical Systems, Journal of,* vol. 12, pp. 179-184, 2003.

[42]   L. Lin and A. P. Pisano, "Silicon-processed microneedles," *Microelectromechanical Systems, Journal of,* vol. 8, p. 78, 1999.

[43]   R. Rathnasingham, D. R. Kipke, S. C. Bledsoe, and J. D. McLaren, "Characterization of Implantable Microfabricated Fluid Delivery Devices," *IEEE TRANSACTIONS ON BIOMEDICAL ENGINEERING,* vol. 51, pp. 138-145, Jan 2004.

[44]   K. D. Wise, J. B. Angell, and A. Starr, "An integrated circuit approach to extracellular microelectrodes," in *the 8th Int. Conf. Engineering Medicine and Biology*, 1969, pp. 14-15.

[45]   K. D. Wise, D. J. Anderson, J. F. Hetke, D. R. Kipke, and K. Najafi, "Wireless implantable microsystems: high-density electronic interfaces to the nervous system," *Proceedings of the IEEE,* vol. 92, p. 76, 2004.

[46]   S. J. Tanghe, K. Najafi, and K. D. Wise, "A planar IrO multichannel stimulating electrode for use in neural prostheses," *Sensors and Actuators B: Chemical,* vol. 1, pp. 464-467, 1990.

[47]   K. Najafi, "Solid-state microsensors for cortical nerve recordings," *Engineering in Medicine and Biology Magazine, IEEE,* vol. 13, p. 375, 1994.

[48]   K. Najafi, "Micromachined Systems for Neurophysiological Applications," in

Handbook of Microlithograph, Micromachining, and Microfabrication. vol. II: Micromachining and Microfabrication: SPIE, 1997, pp. 517-569.

[49]   K. Najafi and J. F. Hetke, "Strength characterization of silicon microprobes in neurophysiological tissues," *Biomedical Engineering, IEEE Transactions on,* vol. 37, p. 474, 1990.

[50]   K. Najafi, J. Ji, and K. D. Wise, "Scaling limitations of silicon multichannel recording probes," *Biomedical Engineering, IEEE Transactions on,* vol. 37, p. 1, 1990.

[51]   K. L. Drake, K. D. Wise, J. Farraye, D. J. Anderson, and S. L. BeMent, "Performance of planar multisite microprobes in recording extracellular single-unit intracortical activity," *Biomedical Engineering, IEEE Transactions on,* vol. 35, p. 719, 1988.

[52]   A. C. Hoogerwerf and K. D. Wise, "A three-dimensional microelectrode array for chronic neural recording," *Biomedical Engineering, IEEE Transactions on,* vol. 41, p. 1136, 1994.

[53]   D. J. Anderson, K. Najafi, S. J. Tanghe, D. A. Evans, K. L. Levy, J. F. Hetke, X. Xue, J. J. Zappia, and K. D. Wise, "Batch fabricated thin-film electrodes for stimulation of the central auditory system," *Biomedical Engineering, IEEE Transactions on,* vol. 36, pp. 693-704, 1989.

[54]   C. Jingkuang and K. D. Wise, "A silicon probe with integrated microheaters for thermal marking and monitoring of neural tissue," *Biomedical Engineering, IEEE Transactions on,* vol. 44, p. 770, 1997.

[55]   R. J. Vetter, J. C. Williams, J. F. Hetke, E. A. Nunamaker, and D. R. Kipke,

"Chronic neural recording using silicon-substrate microelectrode arrays implanted in cerebral cortex," *Biomedical Engineering, IEEE Transactions on,* vol. 51, p. 896, 2004.

[56] J. F. Hetke, J. L. Lund, K. Najafi, K. D. Wise, and D. J. Anderson, "Silicon ribbon cables for chronically implantable microelectrode arrays," *Biomedical Engineering, IEEE Transactions on,* vol. 41, p. 314, 1994.

[57] D. R. Kipke, R. J. Vetter, J. C. Williams, and J. F. Hetke, "Silicon-substrate intracortical microelectrode arrays for long-term recording of neuronal spike activity in cerebral cortex," *Neural Systems and Rehabilitation Engineering, IEEE Transactions on [see also IEEE Trans. on Rehabilitation Engineering],* vol. 11, p. 151, 2003.

[58] K. Jones, P. Campbell, and R. Normann, "A glass/silicon composite intracortical electrode array," *Annals of Biomedical Engineering,* vol. 20, pp. 423-437, 1992.

[59] P. K. Campbell, K. E. Jones, R. J. Huber, K. W. Horch, and R. A. Normann, "A silicon-based, three-dimensional neural interface: manufacturingprocesses for an intracortical electrode array," *IEEE Transactions on Biomedical Engineering,* vol. 38, pp. 758-768, 1991.

[60] R. C. Kelly, M. A. Smith, J. M. Samonds, A. Kohn, A. B. Bonds, J. A. Movshon, and T. Sing Lee, "Comparison of Recordings from Microelectrode Arrays and Single Electrodes in the Visual Cortex," *J. Neurosci.,* vol. 27, pp. 261-264, January 10, 2007 2007.

[61] C. T. Nordhausen, P. J. Rousche, and R. A. Normann, "Chronic recordings of visually evoked responses using the utah intracortical electrode array," in

Engineering in Medicine and Biology Society, 1993. Proceedings of the 15th Annual International Conference of the IEEE, 1993, pp. 1391-1392.

[62] P. J. Rousche and R. A. Normann, "Chronic recording capability of the Utah Intracortical Electrode Array in cat sensory cortex," *Journal of Neuroscience Methods,* vol. 82, pp. 1-15, 1998.

[63] P. J. Rousche and R. A. Normann, "Chronic intracortical microstimulation (ICMS) of cat sensory cortex using the Utah intracortical electrode array," *Rehabilitation Engineering, IEEE Transactions on [see also IEEE Trans. on Neural Systems and Rehabilitation],* vol. 7, pp. 56-68, 1999.

[64] S. Suner, M. R. Fellows, C. Vargas-Irwin, G. K. Nakata, and J. P. Donoghue, "Reliability of signals from a chronically implanted, silicon-based electrode array in non-human primate primary motor cortex," *IEEE Transactions on Neural Systems and Rehabilitation Engineering,* vol. 13, 2005.

[65] P. Norlin, M. Kindlundh, A. Mouroux, K. Yoshida, and U. G. Hofmann, "A 32-site neural recording probe fabricated by DRIE of SOI substrates," *Journal of Micromechanics and Microengineering,* vol. 12, pp. 414-419, 2002.

[66] D. T. Kewley, M. D. Hills, D. A. Borkholder, I. E. Opris, N. I. Maluf, C. W. Storment, J. M. Bower, and G. T. A. Kovacs, "Plasma-etched neural probes," *Sensors and Actuators A: Physical,* vol. 58, pp. 27-35, 1997.

[67] K. Cheung, L. Gun, K. Djupsund, D. Yang, and L. P. Lee, "A new neural probe using SOI wafers with topological interlocking mechanisms," in *Microtechnologies in Medicine and Biology, 1st Annual International, Conference On. 2000*, 2000, pp. 507-511.

[68] M. Kindlundh, P. Norlin, and U. G. Hofmann, "A neural probe process enabling variable electrode configurations," *Sensors and Actuators B: Chemical,* vol. 102, pp. 51-58, 2004.

[69] R. R. J. Richardson, J. A. Miller, and W. M. Reichert, "Polyimides as biomaterials: Preliminary biocompatibility testing," *Biomaterials,* vol. 14, pp. 627–635, July 1993.

[70] C. Xu, W. Lemon, and C. Liu, "Design and fabrication of a high-density metal microelectrode array for neural recording," *Sensors and Actuators A: Physical,* vol. 96, pp. 78-85, 2002.

[71] P. J. Rousche, D. S. Pellinen, D. P. Pivin, Jr., J. C. Williams, R. J. Vetter, and D. R. kirke, "Flexible polyimide-based intracortical electrode arrays with bioactive capability," *Biomedical Engineering, IEEE Transactions on,* vol. 48, p. 361, 2001.

[72] S. Takeuchi, T. Suzuki, K. Mabuchi, and H. Fujita, "3D flexible multichannel neural probe array," *JOURNAL OF MICROMECHANICS AND MICROENGINEERING,* vol. 14, pp. 104-107, 2004.

[73] K.-K. Lee, J. He, A. Singh, S. Massia, G. Ehteshami, B. Kim, and G. Raupp, "Polyimide-based intracortical neural implant with improved structural stiffness," *JOURNAL OF MICROMECHANICS AND MICROENGINEERING,* vol. 14, pp. 32-37, 2004.

[74] N. A. Blum, B. G. Carkhuff, H. K. Charles, Jr., R. L. Edwards, and R. A. Meyer, "Multisite microprobes for neural recordings," *IEEE Transactions on Biomedical Engineering,* vol. 38, p. 68, 1991.

[75] J. F. Hetke, J. C. Williams, D. S. Pellinen, R. J. Vetter, and D. R. Kipke, "3-D

Silicon Probe Array with Hybrid Polymer Interconnect for Chronic Cortical Recording," in *The 1st International IEEE EMBS Conference on Neural Engineering*, Capri Island, Italy, Mach 20-22, 2003.

[76]   J. Subbaroyan and D. R. Kipke, "The role of flexible polymer interconnects in chronic tissue response induced by intracortical microelectrodes - a modeling and an in vivo study," in *The 28th IEEE EMBS Annual International Conference*, New York City, USA, Aug 30-Sept 3, 2006.

[77]   J. M. Carmena, M. A. Lebedev, R. E. Crist, J. E. Doherty, D. M. Santucci, D. F. Dimitrov, P. G. Patil, C. S. Henriquez, and M. A. L. Nicolelis, "Learning to Control a Brain-Machine Interface for Reaching and Grasping by Primates," *PLoS Biology,* vol. 1, p. e42, 2003.

[78]   M. D. Serruya, N. G. Hatsopoulos, L. Paninski, M. R. Fellows, and J. P. Donoghue, "Brain-machine interface: Instant neural control of a movement signal," *Nature,* vol. 416, pp. 141-142, 2002.

[79]   D. M. Taylor, S. I. H. Tillery, and A. B. Schwartz, "Direct Cortical Control of 3D Neuroprosthetic Devices," *Science,* vol. 296, pp. 1829-1832, June 7, 2002 2002.

[80]   J. Wessberg, C. R. Stambaugh, J. D. Kralik, P. D. Beck, M. Laubach, J. K. Chapin, J. Kim, S. J. Biggs, M. A. Srinivasan, and M. A. L. Nicolelis, "Real-time prediction of hand trajectory by ensembles of cortical neurons in primates," *Nature,* vol. 408, pp. 361-365, 2000.

[81]   R. A. Andersen, J. W. Burdick, S. Musallam, H. Scherberger, B. Pesaran, D. Meeker, B. D. Corneil, I. Fineman, Z. Nenadic, E. Branchaud, J. G. Cham, B. Greger, Y. C. Tai, and M. M. Mojarradi, "Recording advances for neural

prosthetics," in *Proceedings of the 26th Annual International Conference of the IEEE EMBS*, San Francisco, CA, USA, 2004, pp. 5352-5355.

[82] R. A. Andersen, J. W. Burdick, S. Musallam, B. Pesaran, and J. G. Cham, "Cognitive neural prosthetics," *Trends in Cognitive Sciences,* vol. 8, p. 486, 2004.

[83] S. Musallam, B. D. Corneil, B. Greger, H. Scherberger, and R. A. Andersen, "Cognitive Control Signals for Neural Prosthetics," *Science,* vol. 305, pp. 258-262, July 9, 2004 2004.

[84] R. A. Andersen, J. W. Burdick, S. Musallam, H. Scherberger, B. Pesaran, D. Meeker, B. D. Corneil, I. Fineman, Z. Nenadic, E. Branchaud, J. G. Cham, B. Greger, Y. C. Tai, and M. M. Mojarradi, "Recording advances for neural prosthetics," in *Engineering in Medicine and Biology Society, 2004. IEMBS '04. 26th Annual International Conference of the IEEE*, 2004, pp. 5352-5355 Vol.7.

[85] Q. He, "Integrated Nano Liquid Chromatography System On-a-Chip," *Ph.D. thesis in electrocal engineering of Calfornia Institute of Technology,* 2005.

[86] K. E. Petersen, "Silicon as a mechanical material," *Proceedings of the IEEE,* vol. 70, pp. 420-457, 1982.

[87] M. Gazicki, G. Surendran, W. James, and H. Yasuda, "Polymerization of Para-Xylyene Derivatives (Parylene Polymerization). II. Heat Effects during Deposition of Parylene C at Different Temperatures," *Journal of Polymer Science,* vol. 23, pp. 2255-2277, 1985.

[88] S. C. Systems, "Parylene knowledge: specifications & properties," *http://www.scscoatings.com/parylene_knowledge/specifications.aspx,* 2007.

[89] S. C. Systems, "Solvent resistance of the Parylene," *Trade literature*.

[90]   S. Nancy, "Literature Review: Biological Safety of Parylene C," *Medical Plastics and Biomaterials,* vol. 3, pp. 30-35, March 1996.

[91]   W. Lonny, "Assessing the performance and suitability of Parylene coating," *Medical Devices & Diagnostic Industry Magazine,* August 2000.

[92]   B. Humphrey, "Using Parylene for Medical Substrate Coating," *Medical Plastics and Biomaterials,* Janurary 1996.

[93]   E. M. Schmidt, J. S. McIntosh, and M. J. Bak, "Long-Term Implants of Parylene-C Coated Microelectrodes," *Med Biol Eng Comput,* vol. 26, pp. 96-101, 1988.

[94]   L. Licklider, X. Q. Wang, A. Desai, Y. C. Tai, and T. D. Lee, "A Micromachined Chip-Based Electrospray Source for Mass Spectrometry," *Anal. Chem.,* vol. 72, pp. 367-375, 2000.

[95]   X.-Q. Wang and Y.-C. Tai, "A normally closed in-channel micro check valve," in *Micro Electro Mechanical Systems, 2000. MEMS 2000. The Thirteenth Annual International Conference on*, 2000, pp. 68-73.

[96]   J. Xie, X. Yang, X.-Q. Wang, and Y.-C. Tai, "Surface micromachined leakage proof Parylene check valve," in *Micro Electro Mechanical Systems, 2001. MEMS 2001. The 14th IEEE International Conference on*, 2001, pp. 539-542.

[97]   J. Xie, J. Shih, and Y.-C. Tai, "Integrated surface-micromachined mass flow controller," in *Micro Electro Mechanical Systems, 2003. MEMS-03 Kyoto. IEEE The Sixteenth Annual International Conference on*, 2003, pp. 20-23.

[98]   J. Xie, Y. Miao, J. Shih, Q. He, J. Liu, Y.-C. Tai, and T. D. Lee, "An Electrochemical Pumping System for On-Chip Gradient Generation " *Analytical*

Chemistry, vol. 76, pp. 3756-3763, 2004.

[99]   J. Xie, J. Shih, and Y. C. Tai, "Integrated parylene electrostatic peristaltic pump," in *2003 Micro Total Analysis System (uTAS '03)*, Squaw Valley, California, USA, Oct. 5-9 2003, pp. 865-869.

[100]   J. Xie, J. Shih, Q. He, C. Pang, Y.-C. Tai, Y. Miao, and T. D. Lee, "An Integrated LC-ESI Chip With Electrochemical-Based Gradient Generation " in *The 17th IEEE International Conference on MicroElectroMechanical Systems (MEMS 2004)*, Maastricht, the Netherlands, 2004, pp. 334-337.

[101]   Q. He, C. Pang, Y.-C. Tai, and T. D. Lee, "Ion Liquid Chromatography On-a-Chip with Beads-Packed Parylene Column," in *The 17th IEEE International Conference on MicroElectroMechanical Systems (MEMS 2004)*, Maastricht, the Netherlands, 2004, pp. 212-215.

[102]   A. Tooker, J. Erickson, Y. C. Tai, and J. Pine, "Robust and biocompatible neurocages," in *2004 Micro Total Analysis System (uTAS'04)*, Malmo, Sweden, Sept. 26-30, 2004, pp. 64-66.

[103]   A. Tooker, E. Meng, J. Erickson, Y. C. Tai, and J. Pine, "Biocompatible parylene neurocages," *IEEE Engineering in Medicine and Biology,* vol. 24, pp. 30-33, 2005.

[104]   A. Tooker, E. Meng, J. Erickson, Y. C. Tai, and J. Pine, "Development of biocompatible neurocages," in *The 26th Annual International Conference of the IEEE Engineering in Medicine and Biology Society (EMBS'04)*, San Francisco, California, USA, Sept. 1-5, 2004, pp. 2542-2545.

[105]   D. C. Rodger, A. J. Fong, W. Li, H. Ameri, I. Lavrov, H. Zhong, S. Saati, P.

Menon, E. Meng, J. W. Burdick, R. R. Roy, V. R. Edgerton, J. D. Weiland, M. S. Humayun, and Y. C. Tai, "High-density Flexible Parylene-based Multielectrode Arrays for Retinal and Spinal Cord Stimulation," in *The 14th International Conference on Solid-State Sensors, Actuators and Microsystems (Transducers '07)*, Lyon, France, 2007.

[106]   D. C. Rodger, W. Li, H. Ameri, A. Ray, J. D. Weiland, M. S. Humayun, and Y. C. Tai, "Flexible parylene-based microelectrode technology for intraocular retinal prostheses," in *The First Annual IEEE International Conference on Nano/Micro Engineered and Molecular Systems (IEEE-NEMS'06)*, Zhuhai, China, Jan. 18-21, 2006.

[107]   D. C. Rodger, W. Li, A. J. Fong, H. Ameri, E. Meng, J. W. Burdick, R. R. Roy, V. R. Edgerton, J. D. Weiland, M. S. Humayun, and Y. C. Tai, "Flexible microfabricated parylene multielectrode arrays for retinal stimulation and spinal cord field modulation," in *The 4th International IEEE-EMBS Special Topic Conference on Microtechnologies in Medicine and Biology (MMB'06)*, Okinawa, Japan, May 9-12, 2006, pp. 31-34.

[108]   W. Li, D. C. Rodger, E. Meng, J. D. Weiland, M. S. Humayun, and Y.-C. Tai, "Flexible parylene packaged intraocular coil for retinal prostheses," in *The 4th International IEEE-EMBS Special Topic Conference on Microtechnologies in Medicine and Biology (MMB'06)*, Okinawa, Japan, May 9-12, 2006, pp. 105-108.

[109]   W. Li, D. C. Rodger, J. D. Weiland, M. Humayun, and Y. C. Tai, "Integrated flexible ocular coil for power and data transfer in retinal prostheses," in *The 27th Annual International Conference of the Engineering in Medicine and Biology*

Society, 2005, (IEEE-EMBC 2005), Shanghai China, 2005, pp. 1028-1031.

[110] D. C. Rodger, J. D. Weiland, M. S. Humayun, and T. Yu-Chong, "Scalable flexible chip-level parylene package for high lead count retinal prostheses," in *Solid-State Sensors, Actuators and Microsystems, 2005. Digest of Technical Papers. TRANSDUCERS '05. The 13th International Conference on*, 2005, pp. 1973-1976 Vol. 2.

[111] D. C. Rodger and T. Yu-Chong, "Microelectronic packaging for retinal prostheses," *Engineering in Medicine and Biology Magazine, IEEE,* vol. 24, pp. 52-57, 2005.

[112] P. J. Chen, D. Rodger, M. Humayun, and Y. C. Tai, "Spiral-tube parylene intraocular pressure sensor," in *The 18th IEEE International Conference on Micro Electro Mechanical Systems (MEMS '05)*, Miami Beach, Florida, USA, 2005, pp. 311-314.

[113] P. J. Chen, D. Rodger, and Y. C. Tai, "Fully-Dry Fabrication of Monolithic High-Aspect-Ratio Embedded Parylene Microchannels," in *The Ninth International Conference on Miniaturized Systems for Chemistry and Life Sciences (µTAS'05)*, Boston, Massachusetts, USA, Oct. 9-13, 2005, pp. 181-183.

[114] P. J. Chen, D. C. Rodger, E. Meng, M. S. Humayun, and Y. C. Tai, "Implantable Unpowered Parylene MEMS Intraocular Pressure Sensor," in *The 4th International IEEE-EMBS Special Topic Conference on Microtechnologies in Medicine and Biology (MMB'06)*, Okinawa, Japan, May 9-12, 2006, pp. 256-259.

[115] P. J. Chen, D. C. Rodger, E. Meng, M. S. Humayun, and T. D. Y.C. Tai", , , , pp. . "In Vivo Characterization of Implantable Unpowered Parylene MEMS Intraocular

Pressure Sensors," in *The 10th International Conference on Miniaturized Systems for Chemistry and Life Sciences (µTAS'06)*, Tokyo, Japan, Nov. 5-9, 2006, pp. 834-836.

[116] P. J. Chen, C. Y. Shih, and Y. C. Tai, "Design, Fabrication and Characterization of Monolithic Embedded Parylene Microchannels in Silicon Substrate," *Lab on a Chip,* vol. 6, pp. 803-810, 2006.

[117] P. J. Chen and Y. C. Tai, "Monolithic High-Aspect-Ratio Embedded Parylene Channel Technology: Fabrication, Integration, and Applications," in *The First Annual IEEE International Conference on Nano/Micro Engineered and Molecular Systems (IEEE-NEMS'06)*, Zhuhai, China, Jan. 18-21, 2006, pp. 1284-1287.

[118] C. Pang, J. G.Cham, Z. Nenadic, Y.-C. Tai, J. W. Burdick, and R. A. Andersen, "A New Neural Recording Electrode Array with Parylene Insulating Layer," in *The Ninth International Conference on Miniaturized Systems for Chemistry and Life Sciences (µTAS)* Boston, Massachusetts, USA, 2005.

[119] C. Pang, J. G. Cham, Z. Nenadic, S. Musallam, Y.-C. Tai, J. W. Burdick, and R. A. Andersen, "A New Multi-Site Probe Array with Monolithically Integrated Parylene Flexible Cable for Neural Prostheses," in *The 27th Annual International Conference of the Engineering in Medicine and Biology Society, (IEEE-EMBS 2005)*, 2005, pp. 7114-7117.

[120] C. Pang, J. G. Cham, S. Musallam, Y.-C. Tai, J. W. Burdick, and R. A. Andersen, "Monolithic Silicon Probes with Flexible Parylene Cables for Neural Prostheses," in *The 1st IEEE International Conference on Nano/Micro Engineered and Molecular Systems, (NEMS '06)* 2006, pp. 1125-1128.

[121] C. Pang, S. Musallam, Y.-C. Tai, J. W. Burdick, and R. A. Andersen, "Novel Monolithic Silicon Probes with Flexible Parylene Cables for Neural Prostheses," in *2006 International Conference on Microtechnologies in Medicine and Biology*, 2006, pp. 64-67.

[122] C. Pang, S. Musallam, D. Rizzuto, C. Ustun, Y.-C. Tai, J. W. Burdick, and R. A. Andersen, "Vivo Study of Mechanical Properties for the Monolithic Silicon Probes with Flexible Parylene Cables for Neural Prostheses," in *The 10th International Conference on Miniaturized Systems for Chemistry and Life Sciences (µTAS'06)*, Tokyo, Japan, Nov. 5-9, 2006, pp. 702-704.

[123] R. Huang, C. Pang, Y.-C. Tai, J. Emken, C. Ustun, and R. A. Andersen, "Parylene coated silicon probes for neural prosthesis," in *The 3rd IEEE International Conference on Nano/Micro Engineered and Molecular Systems, (NEMS '08)* Sanya, Hainan, China, 2008 (Submitted).

[124] M. P. Maher, J. Pine, J. Wright, and Y.-C. Tai, "The neurochip: a new multielectrode device for stimulating and recording from cultured neurons," *Journal of Neuroscience Methods,* vol. 87, pp. 45-56, 1999.

[125] R. Huang, C. Pang, Y.-C. Tai, J. Emken, C. Ustun, D. S. Rizzuto, R. A. Andersen, and J. W. Burdick, "Integrated Parylene-Cabled Silicon Probes for Neural Prosthetics," in *The 21th IEEE International Conference on Micro Electro Mechanical Systems (MEMS '08)*, 2008 (Submitted).

[126] "Research Products: Compoments: Chronic Connectors," *Cyberkineticsinc Neurotechnology Systems, Inc.,* p. http://www.cyberkineticsinc.com/content/researchproducts/chronic.jsp, 2007.

[127] C. J. J. Avezaat and J. H. M. v. Eijndhoven, "The role of the pulsatile pressure variations in intracranial pressure monitoring," *Neurosurgical Review,* vol. 9, pp. 113-120, 1986.

[128] M. S. Fee, "Active Stabilization of Electrodes for Intracellular Recording in Awake Behaving Animals," *Neuron,* vol. 27, pp. 461-468, 2000.

[129] P. D. Wall, J. Freeman, and D. Major, "Dorsal horn cells in spinal and in freely moving rats," *Exp Neurol,* vol. 19, pp. 519-529, 1967.

[130] J. L. Kubie, "A driveable bundle of microwires for collecting single-unit data from freely-moving rats," *Physiology & Behavior,* vol. 32, pp. 115-118, 1984.

[131] S. Venkatachalam, M. S. Fee, and D. Kleinfeld, "Ultra-miniature headstage with 6-channel drive and vacuum-assisted micro-wire implantation for chronic recording from the neocortex," *Journal of Neuroscience Methods,* vol. 90, pp. 37-46, 1999.

[132] J. D. Kralik, D. F. Dimitrov, D. J. Krupa, D. B. K. DB, D. Cohen, and M. A. Nicolelis, "Techniques for long-term multisite neuronal ensemble recordings in behaving animals," *Journal of Neuroscience Methods,* vol. 25, 2001.

[133] J. G. Keating and G. L. Gerstein, "A chronic multi-electrode microdrive for small animals," *Journal of Neuroscience Methods,* vol. 117, pp. 201-206, 2002.

[134] C. S. Lansink, M. Bakker, W. Buster, J. Lankelma, R. van der Blom, R. Westdorp, R. N. J. M. A. Joosten, B. L. McNaughton, and C. M. A. Pennartz, "A split microdrive for simultaneous multi-electrode recordings from two brain areas in awake small animals," *Journal of Neuroscience Methods,* vol. 162, pp. 129-138, 2007.

[135] R. C. deCharms, D. T. Blake, and M. M. Merzenich, "A multielectrode implant device for the cerebral cortex," *Journal of Neuroscience Methods,* vol. 93, pp. 27-35, 1999.

[136] R. Eckhorn and U. Thomas, "A new method for the insertion of multiple microprobes into neural and muscular tissue, including fiber electrodes, fine wires, needles and microsensors," *Journal of Neuroscience Methods,* vol. 49, pp. 175-179, 1993.

[137] S. N. Baker, N. Philbin, R. Spinks, E. M. Pinches, D. M. Wolpert, D. G. MacManus, Q. Pauluis, and R. N. Lemon, "Multiple single unit recording in the cortex of monkeys using independently moveable microelectrodes," *Journal of Neuroscience Methods,* vol. 94, pp. 5-17, 1999.

[138] M. S. Fee and A. Leonardo, "Miniature motorized microdrive and commutator system for chronic neural recording in small animals," *Journal of Neuroscience Methods,* vol. 112, pp. 83-94, 2001.

[139] J. G. Cham, E. A. Branchaud, Z. Nenadic, B. Greger, R. A. Andersen, and J. W. Burdick, "Semi-Chronic Motorized Microdrive and Control Algorithm for Autonomously Isolating and Maintaining Optimal Extracellular Action Potentials," *J Neurophysiol,* vol. 93, pp. 570-579, January 1, 2005 2005.

[140] E. A. Branchaud, J. G. Cham, Z. Nenadic, J. W. Burdick, and R. A. Andersen, "A Miniature Robot for Autonomous Single Neuron Recordings," in *Robotics and Automation, 2005. ICRA 2005. Proceedings of the 2005 IEEE International Conference on*, 2005, pp. 1920-1926.

[141] J. G. Cham, M. T. Wolf, R. A. Andersen, and J. W. Burdick, "Miniature Neural

Interface Microdrive using Parylene-coated Layered Manufacturing," in *2006 IEEE/RAS-EMBS International Conference on Biomedical Robotics and Biomechatronics*, 2006.

[142] E. A. Branchaud, J. W. Burdick, and R. A. Andersen, "An Algorithm for Autonomous Isolation of Neurons in Extracellular Recordings," in *Biomedical Robotics and Biomechatronics, 2006. BioRob 2006. The First IEEE/RAS-EMBS International Conference on*, 2006, pp. 939-945.

[143] E. A. Branchaud, "A Control System for Positioning Recording Electrodes to Isolate Neurons in Extracellular Recording," *Ph.D. thesis in mechanical engineering of Calfornia Institute of Technology,* 2006.

[144] J. Branebjerg and P. Gravesen, "A new electrostatic actuator providing improved stroke length and force," in *Micro Electro Mechanical Systems, 1992, MEMS '92, Proceedings. An Investigation of Micro Structures, Sensors, Actuators, Machines and Robot. IEEE*, 1992, pp. 6-11.

[145] K. Sato and M. Shikida, "Electrostatic film actuator with a large vertical displacement," in *Micro Electro Mechanical Systems, 1992, MEMS '92, Proceedings. An Investigation of Micro Structures, Sensors, Actuators, Machines and Robot. IEEE*, 1992, pp. 1-5.

[146] R. Zengerle, A. Richter, and H. Sandmaier, "A micro membrane pump with electrostatic actuation," in *Micro Electro Mechanical Systems, 1992, MEMS '92, Proceedings. An Investigation of Micro Structures, Sensors, Actuators, Machines and Robot. IEEE*, 1992, pp. 19-24.

[147] M. Mescher, T. Abe, B. Brunett, H. Metla, T. E. Schlesinger, and M. Reed,

"Piezoelectric lead-zirconate-titanate actuator films for microelectromechanical systems applications," in *Micro Electro Mechanical Systems, 1995, MEMS '95, Proceedings. IEEE*, 1995, p. 261.

[148] M. Esashi, S. Shoji, and A. Nakano, "Normally close microvalve and micropump fabricated on a silicon wafer," in *Micro Electro Mechanical Systems, 1989, Proceedings, 'An Investigation of Micro Structures, Sensors, Actuators, Machines and Robots'. IEEE*, 1989, pp. 29-34.

[149] O. C. Jeong and S. S. Yang, "Fabrication of a thermopneumatic microactuator with a corrugated p+ silicon diaphragm," *Sensors and Actuators A: Physical,* vol. 80, pp. 62-67, 2000.

[150] C. Grosjean, Y. Xing, and T. Yu-Chong, "A practical thermopneumatic valve," in *Micro Electro Mechanical Systems, 1999. MEMS '99. Twelfth IEEE International Conference on*, 1999, pp. 147-152.

[151] H. Jerman, "Electrically-activated, micromachined diaphragm valves," in *Solid-State Sensor and Actuator Workshop, 1990. 4th Technical Digest., IEEE*, 1990, pp. 65-69.

[152] M. Kohl and K. D. Skrobanek, "Linear microactuators based on the shape memory effect," in *Solid State Sensors and Actuators, 1997. TRANSDUCERS '97 Chicago., 1997 International Conference on*, 1997, pp. 785-788 vol.2.

[153] C. Doring, T. Grauer, J. Marek, M. S. Mettner, H. P. Trah, and M. Willmann, "Micromachined thermoelectrically driven cantilever structures for fluid jet deflection," in *Micro Electro Mechanical Systems, 1992, MEMS '92, Proceedings. An Investigation of Micro Structures, Sensors, Actuators, Machines and Robot.*

IEEE, 1992, pp. 12-18.

[154] C. G. Cameron and M. S. Freund, "Electrolytic actuators: Alternative, high-performance, material-based devices," *PNAS,* vol. 99, pp. 7827-7831, June 11, 2002 2002.

[155] C. Pang, Y.-C. Tai, J. W. Burdick, and R. A. Andersen, "Electrolysis-Based Diaphragm Actuators " in *The International Conference on Bio-Nano-Informatics (BNI) Fusion*, Marina del Rey, California, USA, 2005.

[156] C. Pang, Y. C. Tai, J. W. Burdick, and R. A. Andersen, "Electrolysis-based diaphragm actuators," *NANOTECHNOLOGY,* vol. 17, pp. S64-S68, 2006.

[157] C.-T. Pan, A. H. Yang, A. S.-C. Shen, A. M.-C. Chou, and A. H.-P. Chou, "A low-temperature wafer bonding technique using patternable materials," *Journal of Micromechanics and Microengineering,* pp. 611-615, 2002.

[158] C. Pang, Y.-C. Tai, J. W. Burdick, and R. A. Andersen, "Electrolysis-based Parylene Balloon Actuators for Movable Neural Probes," in *The Second Annual IEEE International Conference on Nano/Micro Engineered and Molecular Systems (IEEE-NEMS'07)*, Bangkok, Thailand, Jan. 16-19, 2007, pp. 913-916.